A NOVEL H$_2$S MONITOR USING COPPER (II) OXIDE AND RAMAN SPECTROSCOPY: A PROOF OF CONCEPT

A Thesis Submitted to the College of

Graduate Studies and Research

in Partial Fulfillment of the Requirements

for the Degree of Master of Science

in the Division of Biomedical Engineering

University of Saskatchewan

Saskatoon, Saskatchewan

Canada

By

Syed Ghazali Ahmad

PERMISSION TO USE

In presenting this thesis in partial fulfillment of the requirements for a Postgraduate degree from the University of Saskatchewan, I agree that the libraries of this University may make it freely available for inspection. I further agree that permission for copying of this thesis in any manner, in whole or in part, for scholarly purposes may be granted by the professor or professors who supervised my thesis work or, in their absence, by the Head of the Department or the Dean of the College in which my thesis work was done. It is understood that any copying or publication or use of this thesis or parts thereof for financial gain shall not be allowed without my written permission. It is also understood that due recognition shall be given to me and to the University of Saskatchewan in any scholarly use which may be made of any material in my thesis.

Requests for permission to copy or to make other uses of materials in this thesis in whole or part should be addressed to:

> Head of the Division of Biomedical Engineering
> University of Saskatchewan
> Saskatoon, Saskatchewan S7N 5A9
> Canada

ABSTRACT

Development of a novel aqueous hydrogen sulfide (H_2S) detector is presented in this thesis. Nano copper (II) oxide (CuO) was selected as the detector material. Nano-CuO was synthesized by thermal oxidation and wet synthesis. CuS is produced from the reaction of CuO with H_2S and Raman spectroscopy was used for its detection.

The research presented in this thesis aimed at optimizing the parameters to produce coupons of CuO that can be used to detect H_2S (*aq*) over the concentration range of 3.81×10^{-3} ppm – 3.91×10^{-9} ppm (0.1 M – 0.1 μM) by using Raman spectroscopy. Four specific objectives were devised to (1) determine the optimal synthetic technique for CuO, (2) determine which synthesis provides optimal CuO/CuS Raman spectra, (3) determine the linear range and detection limit of H_2S by measuring the Raman Spectrum of CuS and, (4) to determine the rate of accumulation of CuS in human serum.

The nano-CuO material with the optimal CuO/CuS Raman bands of interest was synthesized by thermal oxidation, where copper mesh (149 μm) was heated at 400 °C in air for 2 hours. The limit of detection of H_2S (*aq*) by the optimal CuO is 1.22×10^{-8} ppm (3.59×10^{-7} M) with a linear range extending from 7.53×10^{-3} – 1.22×10^{-8} ppm (6.56×10^{-1} – 3.57×10^{-7} M).

This study has provided new knowledge through (1) the development of a novel methodology to measure H_2S (*aq*) concentration in serum by using CuO and Raman spectroscopy, (2) the discovery that CuO is specific to H_2S and does not interact with proteins in human serum or other sulfur compounds at clinical concentrations, (3) determination that H_2S (*aq*) detection is linear over the 7.53×10^{-3} – 1.22×10^{-8} ppm range with no interference of the Raman band from other biomaterials, and (4) the rate of accumulation is 0.1441 R/s.

ACKNOWLEDGMENTS

TABLE OF CONTENTS

LIST OF TABLES

LIST OF FIGURES

LIST OF ABBREVIATIONS

μm:	Micrometer
μM:	Micromolar
3-MST:	3-mercaptopyruvate sulfurtransferase
A / Ǎ:	Angstrom
AA:	Acetyl Acetate
AKT-P:	Adenosine Monophosphate activated protein kinase
ANOVA:	Analysis of Variance
aq:	Aqueous
BSA:	Bovine Serum Albumin
CBS:	Cystathionine-β-synthase
CNTs:	Carbon nanotubes
CSE:	Cystathionine γ-lyase
CTAB:	Cetyl trimethylammonium bromide
$Cu(OH)_2$:	Copper (II) Hydroxide
CuO:	Copper (II) oxide
Cys:	Cysteine
ddH_2O:	Distilled and degassed water
dH_2O:	Distilled water
DNA:	Deoxynucleic acids
eV:	Electron Volts
H- bonding:	Hydrogen bonding
Hcy:	Homocysteine
HS^-:	Sulfanide (or Bisulfide)
HSA:	Human Serum Albumin
IR:	Infrared spectroscopy
K:	Kalvin (when discussing temperature) or Potassium (when discussing chemicals)
LDH:	Lactate dehydrogenate

L-DOPA:	L-Dihydroxyphenolalanine
M:	Molarity
Met:	Methionine
mm:	Millimetre
$Na_2S \cdot 9H_2O$:	Sodium Sulfide Nonahydrate
NaHS:	Sodium Sulfanide
Nano-X:	Nano sized "X". i.e. Nano-CuO = Nano sized copper (II) oxide
NH_4OH:	Ammonium Hydroxide
nm:	Nanometers
oAs:	Acetate
Pa:	Pascal (measurement of pressure)
$Pb(ClO_4)_2$:	Lead perchlorate
PEPCK:	Phosphoenolpyruvate carboxykinase
pH:	Power of Hydrogen
pKa:	Acid dissociation constant
R:	Raman Counts
R/s:	Raman Counts per second
SAOB:	Sulfur Antioxidant Buffer
Sccm:	Standard cubic centimeters per minute
SEM:	Scanning Electron Microscopy
SERS"	Surface Enhanced Raman Spectroscopy
T_N:	Neel's Temperature
Ti:	Titanium
V:	Volts
VLS:	Vapor – Liquid – Solid Synthetic Method
W:	Tungsten
XRD:	X-Ray Diffraction

CHAPTER 1: INTRODUCTION

1.1. Background and Motivation

Since the discovery of H_2S as a neurotransmitter in the late 1980s[1–3], every investigation of its clinical importance has revealed an increasingly important role of H_2S in proper physiological functioning. H_2S is a biological signalling molecule which is involved in many seemingly unrelated biological processes, for example neurotransmission and muscle relaxation. H_2S is the third most prominent gasotransmitter, following nitric oxide (NO) and carbon monoxide (CO). Therefore, it is not surprising that H_2S is involved in a number of diseases including diabetes, cardiovascular diseases, hypertension, erectile dysfunction, Alzheimer's disease, Parkinson's Disease[4–14].

The detection of early onset of disease would have tremendous impact in healthcare and the entire healthcare field. Many secondary and preventable diseases manifest themselves in already sick patients, resulting in early deaths, decreased quality of life, increased burden on our already over-worked health professionals, and the added cost of medications. Thus, a H_2S detector can greatly benefit the health system. However, there is a severe lack of medical instruments capable of testing for this important molecule.

High quality spectral detectors, as required in the health field, require a material to bind preferentially to the disease marker (in this case H_2S) and upon binding have an easily detectable change in spectral response. The criteria for this material should be: 1) strong and selective binding, 2) easily detectable change in spectrum, 3) require small amounts of the disease marker, and 4) preferably, all materials should be non-toxic. Further practical considerations include: A) affordability, B) ease of production, C) size of device and D) small quantities of material required for measurement.

The greatest difficulty arises from the selection of material and type of spectrometer. Raman Spectroscopy measures vibrational spectra through an inelastic scattering process. Raman spectroscopy is an excellent and widely used tool for molecular fingerprinting. Additionally, Raman spectra can be measured without

significant interference from aqueous media, thus making it an excellent probe of biomaterials. Raman spectrometers are now available commercially as hand-held devices, for example by Horiba Scientific[15], making them practical for individual care and monitoring.

The last requirement for a detector is having a material with strong, preferential binding and an easily detectable spectral change. Nano-CuO reacts with H_2S to produce CuS, which forms Cu-S-S-Cu through a disulfide bridge. A new and clearly defined Raman band unequivocally fingerprints the Cu-S-S-Cu. Thus, nano-CuO is a promising material for H_2S detection.

1.2. Previous Work on H2S Detection Methods

Until the 2000s, the main methods of H_2S detection required large samples of tissue and were not convenient for clinical applications[16,17]. A novel technique was developed for the detection of H_2S was utilizing CNTs and confocal laser scanning microscopy or Raman spectroscopy to determine the quantity of H_2S in serum[16,17]. The underlying principle is similar to that of activated carbon used in scrubbers of chimney stacks where H_2S dissociates into HS^- and reacts with dissolved oxygen in the presence of activated carbon (heated/processed carbon in order to increase its reactivity). Upon reacting, hydroxide and sulfide ions are produced, the sulphide binds irreversibly with the activated carbon. The change in emission between the sulphur bound and non-sulphur bound CNT can be measured. One of the drawbacks of this method is that the defect sites of the CNT preferentially binds the sulfide ion and since defects on CNT are not well controlled, there is significant variability in the measurement[17]. This process was further developed, but the quality control of CNT posed a problem with reproducibility of results[17]. Another major drawback of this technique is that H_2S binds both reversibly and irreversibly with CNT and, it is likely that the reversible association of the H_2S within the pores of the CNT produced a significant percentage of the signal. The dominant mechanism for H_2S (*aq*) adsorption is likely through the filling of the CNT pores and vacancies[17,18]. As with any non-equilibrium reversible process, a steady state will not be reached, so the intensity of the signal of interest will change with time at physiological pH (pH of 7.4) and room temperature (25 °C), there is approximately 31% H_2S, 69% HS^- and approximately 0% S^{2-} (~2.5 x10^{-12} times lower than [HS^-])[18,19], whereas at physiological pH and temperature (37 °C) there is a difference in the acid dissociation constant (pKa) values. Experimentally, it has been found that the percentage of H_2S in trout is ~18.5%. As such it must also be remembered that due to the temperature

difference, the pKa_1 and pKa_2 values for the dissociation of H_2S into HS^- and subsequently into S^{2-} change as well[19]. Interestingly there is a debate over the value of pKa_2; the two proposed values of pKa_2 are 19 and 13.4[20]. It has been claimed that lower pKa_2 value is based heavily on theoretical calculations from thermodynamic equations whereas $pKa_2 = 19$ was determined using experimental methods[21]. For the purpose of this research the value of 19 is selected giving pKa values of $pKa_1 = 7.05$ & $pKa_2 = 19$[22]; at 37 °C: $pKa_1 = 6.755$[19] and pKa_2 is unknown. Regardless of the exact value of the pKa_2, it is known that the concentration of S^{2-} in physiological conditions is negligible[6,23]. Both the Raman and the confocal laser microscopy are very limited in their ability to discern even 1 µM samples (the limit is 10 µM) and as such these methods are not sensitive enough to be useful[17].

Moreover, with a fluorescent technique, there is always a residual baseline. It is known that activated carbon and CNT can bind to many constituents of sera, so the technique may not be a reliable source of detection for H_2S. It has been found that CNTs bind to Human Serum Albumin (HSA)[24] (the most abundant protein in the human body[25]), hemoglobin[26], DNA[27], antigens[28], myoglobin[29], streptavidin[30], Bovine Serum Albumin (BSA)[31], apolipoproteins[32] and various other proteins[33] and cannot be used to specifically determine the H_2S concentration levels. Taking hemoglobin as an example, let us imagine the case of two patients; one patient is physiologically normal and the other has an undiagnosed case of hemolytic anemia (a disease where the body destroys blood cells and thus the hemoglobin count is low in these individuals[34]). In a normal patient, the hemoglobin competitively binds to CNT alongside H_2S and gives a particular intensity of spectrum. The other patient has a tremendously larger H_2S spectral signature due to the lack of hemoglobin inhibition. Upon receiving this result of the large H_2S peak intensity, the medical examiner would have to conclude that either 1) there is an over production of H_2S in the body and as such perhaps the body is responding to cardiac arrest or some other problem; 2) the patient is suffering from low blood pressure; 3) the patient is unable to break down H_2S or 4) there is a lower quantity of one of the many competitive binders of H_2S (in this case hemoglobin). In order to interpret the result of the measurement, 2-3 more tests must be conducted, assuming that the patient only has one disease at a time which is not always the case. Although hemolytic anemia was given as an example, the same applies to each of the other competitive binding proteins mentioned and their corresponding diseases, making this method not practical. As such, based on the current technology, other mechanisms may be more reliable and useful.

By using nano-CuO only characteristic binding of H_2S to the CuO will be monitored, thus overcoming

3

the problems of CNT binding. The benefits of using nano-CuO is the reproducibility of the CuO samples, the ability to manufacture uniform CuO coupons, intense appearance of a spectral band at 472 cm^{-1} forming the Cu-S-S-Cu bond and the (expected) specificity of CuO for H_2S or HS^-. The Raman band at 472 cm^{-1} can be red or blue shifted due to size effects.

1.3. Research and Objectives

The aim of this research is to develop a coupon for the detection of H_2S over the concentration range of 0.1 μM – 0.1 M, which corresponds to 3.81×10^{-3} to 3.9×10^{-9} ppm of H_2S. In order to do this, four specific objectives must be met which are: (1) optimization of the synthesis of the CuO, (2) determination of an optimal CuO/CuS synthesis technique, (3) determine the linear detection range as well as the limit of detection of H_2S using CuO, and (4) determine the rate of accumulation of CuS in serum solution.

1.4. Thesis Organization

The purpose of Chapter 2 is of two-fold; the first purpose is to provide background information on the two main compounds of interest (H_2S and CuO) and the second purpose is to provide a justification for the objectives mentioned in section 1.3 as well as the techniques used throughout this thesis.

Chapter 3 is focused on the materials and methods of the samples prepared and the experiments performed. The results and discussions are reported in Chapter 4. The results for the selection of the optimal synthetic technique, the 4-hour experiment, determination of the rate of accumulation and the H_2S specificity tests. Lastly, Chapter 5 describes the conclusion where the successes and limitations of the methods employed in this thesis are highlighted. Future recommendations are also made.

CHAPTER 2: LITERATURE OVERVIEW

A literature review is presented in the following section. Section 2.1 discusses hydrogen sulfide, and its role in the biological systems and its role in biological systems and section 2.2 provides a brief overview on the synthesis of nano-CuO materials and 2.3 provides a brief description of Raman spectroscopy.

2.1. H₂S in Biological Systems

Hydrogen sulfide is a deadly yet necessary compound. Since the initial studies in the 1990s revealed that endogenous hydrogen sulfide (H_2S) is an important neurotransmitter and a vasodilator involved in the control of blood pressure, the discoveries have yet to cease[6]. The importance and relevance of H_2S to physiological systems have been predicted since the 1940s. Modern science recognizes the importance of H_2S as a signalling molecule with many diverse functions ranging from angiogenesis to the healing of wounds[35–38]. In mammals H_2S is derived mainly from three enzymes: cystathionine γ-lyase (CSE), cystathionine-β-synthase (CBS), and 3-mercaptopyruvate sulfurtransferase (3-MST)[35]. These three enzymes are expressed differentially in various tissues, implying that there are many functions of H_2S in the nervous, circulatory, cardiovascular, respiratory, musculoskeletal and urinary systems in addition to anti-inflammatory properties and prevention of mitochondrial damage[12]. Mutations or otherwise abnormal regulation of H_2S have been shown to result in diabetes, cardiovascular diseases, hypertension, renal and hepatic malfunction, antioxidant and anti-inflammatory properties, erectile dysfunction, as well as Alzheimer's Disease, and Parkinson's Disease[4–14]. At the cellular level, H_2S has been found to interact with cellular targets such as *heme* proteins, nitric oxide, and cysteine residuces[12-14]. As further research expounds more light on to the importance of H_2S on various biological functions, a demand for medical devices to measure H_2S becomes evident.

In summary, H_2S serves three main physiological functions in the body: as a signalling molecule[9,12], as an

antioxidant[12], and as a muscle relaxant/vasodilant[39]. Through these functions, H_2S has an intimate connection with many cellular pathways, including the cardiovascular and renal systems, liver, pancreas, gastrointestinal system, urinary system and the reproductive system[10].

2.1.1. The Role of H_2S in Diabetes

H_2S is intricately involved in blood glucose regulation. It has been found that insulin inhibits CSE activity, which in turn down regulates H_2S production[40,41]. H_2S has been found to upregulate the enzyme PEPCK, while downregulating AKT-P and AMPK-P. PEPCK, is an upregulator of glucose production. AKT-P, AKT, and AMPK-P are enzymes involved in the inhibition of gluconeogenesis. The AMPK-P pathway involves a key enzyme, glucokinase, which is a primary enzyme involved in glucose consumption and storage in the liver. Increases in H_2S lead to high glucose production and the pancreas begins to over-produce insulin in retaliation. An excessive amount of insulin results in insulin insensitivity (insulin resistance), a state where insulin no longer causes a consumption of the glucose, thus leaving elevated levels of blood glucose. Thus, H_2S is intimately involved with type-2 diabetes and may be used for screening for early detection[17,18].

2.1.2. The Role of H_2S in Cardiovascular Diseases

The involvement of H_2S in cardiovascular diseases, is tied to its role in muscle relaxation. H_2S relaxes smooth muscle, such as the heart, as a result of activating potassium ATP-channels[42]. There are three main mechanisms through which sulfide poisoning leads to cardiac arrest: 1) inhibiting L-type calcium channels on cardiomyocytes (thus preventing muscle contraction), 2) reducing available ATP by reducing mitochondrial cytochrome C activity (through reducing aerobic respiration and through the promotion of gluconeogenesis which requires energy) and 3) an upregulation of the neurotransmitter NO, which is known to have depressive effects in muscles[7]. However, it is also well known that with the correct concentrations, H_2S has healing properties for heart attack patients; H_2S induces angiogenesis and promotes blood-vessel growth[43]. Diallyl trisulphide, an organosulfur compound commonly found in garlic which steadily releases H_2S, has been utilized in H_2S-based treatment to reduce damage due to heart attacks[20]. Thus, there is a delicate balance between too much and too little H_2S for cardiovascular patients.

Due to its muscle relaxing properties, an increase in endogenous H_2S can lead to a cardiac arrest[7]. It is difficult to diagnose cardiac arrest as it occurs almost instantly after symptoms appear and thus the need for early detection is critical. On the other hand, a heart attack, or myocardial infarction, is the death of heart muscle tissue. It has been found that an increase in endogenous H_2S is beneficial to heart attack patients, but dangerous to patients of cardiac arrest[43]. Interestingly, after a heart attack, natural mechanisms of the body recruit H_2S towards the heart in order to minimize damage, thus the H_2S levels after a heart attack are higher than before the heart attack[44]. However, a heart attack may lead to cardiac arrest, so if H_2S is used as a therapeutic then the treatment dosage of H_2S must be carefully administered.

This is further complicated by the fact that heart attacks can be "mimicked" by several other diseases, which may result in a misdiagnosis and therefore risk either over-looking the disease (under-diagnosis) or unnecessary expensive tests (over-diagnosis) of the known myocardial infarction biomarkers such as lactate dehydrogenate (LDH) and troponin. Hypertension is among diseases that may mimic a heart attack.

LDH and troponin are dependable biomarkers (among others) of heart attacks because there is a specific version (differential expression) of these biomarkers which, under ordinary conditions, is only present within the heart and have short half-lives. Following a heart attack, damaged tissue "leaks" these differential proteins into the blood for a short period of time and by analyzing the concentration of these biomarkers medical professionals can derive the details of a heart attack, including the approximate time of the incident and the extent of damage[45]. However, an indirect method of determining a heart attack can be significantly cheaper, require less laboratory resources and maybe more feasible for consistent, at-home patient monitoring as well as provide an earlier risk assessment of possible cardiac related diseases. H_2S maybe a useful indicator. It has found that increased levels of urinary sulfur metabolites (thus bodily sulfides) are correlated to more favourable cardiovascular risk profiles[46]. Furthermore, H_2S inhibits calcification and osteoblastic differentiation, both of which are responsible for vascular calcification[47]. Since vascular calcification is a strong indicator of many diseases including myocardial infarction and is known to be a strong indicator of future cardiac events in patients with chronic kidney disease and diabetes, H_2S could possibly be a method to establish risk profiles of future cardiac events in order to facilitate early detection within diabetics and patients of chronic kidney disease[47–49].

As mentioned earlier, hypertension may sometimes be misdiagnosed for heart disease. Hypertension, or

high blood pressure, occurs when the blood flows through the arteries at a higher pressure than normal. The symptoms of hypertension are: shortness of breath, chest pain, tiredness, a racing heart beat among others. The most common symptom for a heart attack is also chest pain or discomfort in the chest, but patients also experience light- headedness or dizziness, tiredness and breathing problems among others. With so many overlapping symptoms, some misdiagnoses are to be expected. H_2S is responsible for vasodilation of the blood vessels through the activation of potassium-gated ATP channels, which decreases blood pressure[13,38,50–52]. A lack of H_2S then causes an increase in blood pressure, or hypertension[38,50]. Thus, a distinction between a heart attack and hypertension can be made with regard to levels of H_2S present. Beyond the circulatory system, H_2S also causes vasodilation in reproductive systems of men and have many implications with erectile dysfunction[6]. Animal model treatments of H_2S have been shown to improve erectile dysfunction[6,14].

To further complicate the situation, hypertension itself is commonly misdiagnosed. The "white collar effect" describes the phenomenon where the blood pressure of a patient is higher when in a medical setting than in a relaxed setting, such as home. Furthermore, estimates predict that approximately 10 – 20% of the population are likely to have undetected hypertension, also known as "masked hypertension" [53]. It is evident from the above that a novel technique to diagnose and monitor hypertension detection must be developed.

2.1.3. The Role of H_2S in Renal Disorders

Beyond the cardiovascular and circulatory systems, H_2S is also greatly involved in the renal pathway[10]. H_2S concentrations has been found to be correlated to renal blood flow, glomerular filtration rate, urinary excretion, natriuresis and kaliuresis[54]. Moreover, H_2S is an upregulator of many antioxidants including glutathione, catalyse, Nrf-2, superoxide dismutase as well as a downregulator of reactive oxygen species' generators including NADPH-oxidase[10,54]. Unregulated H_2S is thought to be a contributing factor of renal disease and also a potential therapeutic target for its cure[10].

2.1.4. The Role of H_2S in Neurological Disorders

Regarding mental disorders, H_2S has a history with neurological disorders. Interestingly, while CSE is the

primary source of H_2S in many systems such as the cardiovascular and respiratory systems, CBS is the primary enzyme for H_2S production in the brain[12]. It has been found that H_2S helps regulate the N-methyl-D-aspartate receptors in the brain, which are responsible for controlling synaptic activity and are heavily involved with memory control[12,55]. The intricate involvement of H_2S with memory has made it a prime target for the treatment of Alzheimer's Disease (the most prominent form of dementia with the most common symptoms being loss of short-term memory, mood changes, and disorientation). Moreover, CBE activators such as S-adenosylmethionine, are negatively correlated with patients of Alzheimer's disease[12,56]. Furthermore, concentration of Homocysteine (Hcy), a neurotoxin produced in the brain, is increased since CBE is involved in its degradation pathway[12]. It has also been found that H_2S donors such as NaHS detoxify Hcy through its antioxidant properties as well as reduce the accumulation of other toxins, such as hypochlorous acid, in the temporal and frontal cortex (associated with attention, short-term memory and memory associated tasks)[6,12,56]. It has been demonstrated that H_2S treatments impair Alzheimer's Disease and increase memory and learning in rat models[44,55,57]. It has been found that there was a deficiency in H_2S levels in Alzheimer's patients, and *in vitro* studies have shown promise of H_2S as a possible therapy for the disease[12]. As such, H_2S may also be useful as a diagnostic test for Alzheimer's disease as well as a possible therapy.

H_2S may also have potential benefits for Parkinson's disease[6]. Parkinson's disease is a neural disorder, mainly effecting motor-control but also effect mood, behaviour and thought, caused by a dopamine deficiency usually due to the death of dopamine-producing cells[58]. Medication for Parkinson's disease largely involve administering the precursor of dopamine, L-Dihydroxyphenolalanine (L-DOPA). L-DOPA is processed into Dopamine by specialized neural cells called nigrostriatal cells. However, as the disease progresses, the inflammatory response of microglial cells cause permanent damage to the neural cells which cause damage to the nigrostrial neurons, preventing them from being able to process L-DOPA into Dopamine. Moreover, the accumulation of L-DOPA is thought to create oxidative stress onto the cellular environment[59]. As such L-DOPA derivatives that would slowly release H_2S were developed. H_2S, being a potent anti-inflammatory, was able to reduce microglial cells and their toxic effects, while its property as an antioxidant reduced the oxidative stress of the excess L-DOPA. The overall result of the production of H_2S is retarding neurodegeneration and thus reducing the symptoms of Parkinson's disease[6,58–60].

Table 2.1: A summary of the change in H_2S levels of a patient based on a number of diseases. Downward arrows represent low levels of H_2S whereas upward arrows indicate increased levels of H_2S.

	Disease	H_2S (level)	Description
1.	Hypertension	⬇	A lack of H_2S causes high blood pressure.
2.	Cardiac Arrest	⬆	H_2S inhibits ATP generation, thus causing a heat to stop.
3.	Myocardial Infarction	⬆	H_2S increases healing process after an infarction.
4.	Vascular Calcification	⬇	H_2S inhibits vascular calcification, which is an indicator of future cardiovascular issues for people with chronic kidney disease.
5.	Type-2 Diabetes	⬇	Insulin inhibits CSE, thus down regulating H_2S production.
6.	Alzheimer's Disease	⬇	A lack of H_2S causes an increase of toxins in neural cells.
7.	Parkinson's Disease	⬇	H_2S reduces oxidative stress, thus slowing disease progression.
8.	Erectile Dysfunction	⬇	Lack of H_2S reduces blood flow to the reproductive organs.

2.1.5. H_2S and its Therapeutic Applications

Table 2.1 summarizes the change in the H_2S levels in a patient with the corresponding disease. However, a question may arise as to determine which disease caused the H_2S imbalance. The answer is to use the method of elimination to deduce the disease. For example, when a patient who has not had a heart attack (myocardial infarction) has high levels of H_2S, it can be known that the patient is at risk of cardiac arrest or a heart attack. Another example is the case of a patient without any neurological disorders who is having trouble breathing and has an irregular heart beat and low H_2S levels. This patient is having hypertension. Many other examples can be provided.

It may also be asked that in the case of a patient with neurological disorders, how can H_2S be a viable detector for their condition? The answer is that a patient with a particular disease will have the symptoms of that disease. For example, if a healthcare professional measures the H_2S levels of an Alzheimer's patient, then the levels of H_2S reflect the condition of Alzheimer's rather than a disease the patient does

not have. This is similar to the case of the blood glucose detectors. Apart from diabetes, there are more than 18 diseases associated with blood sugar (high and low blood sugar). However, the blood sugar levels of a diabetic specifically reflect their diabetes (i.e. if should they take insulin or not).

Kimura, H., and SpringerLink have published a book, *Hydrogen Sulfide and its Therapeutic Applications,* outlining the different potential uses of H_2S as a therapeutic medicine[52]. However, as there is a fine balance between lack of H_2S and intoxication due to H_2S, proper measuring tools are necessary if H_2S is ever to become a feasible therapeutic agent. The physiological H_2S level in blood is under serious debate in the literature. The range of possibilities is between 0.4 µM – 1 mM, a variance of four orders of magnitude[4,61,62]. Some techniques have reported 100-10 µM and claim that levels up to 300 µM do not effect cell viability[61]. However other research has approximated that the physiological concentration to be up to 1 mM[4] and still others have suggested that baseline levels have been found to be on the order of 0.4 - 0.9 µM[62]. In total the variance in the literature regarding the concentration of free sulfide in the blood differs greatly and is likely a result of the variety of techniques used for the measurements. To the extent of my knowledge all methods require a series of reactions (usually acidic or reducing) to first isolate the free sulfide and subsequently measure this sulfide level. However, before the present work, a simple 1-step measuring method has yet to be proposed. It is hypothesized that the proposed method will find the H_2S levels on the order of 0.4 - 0.9 µM, as measured using a monobromodimane measurement[38]. The reason for this hypothesis is that the monobromobimane method is the closest to the presented method and it's likely the correct concentration of H_2S is in the 0.1 µM range[63].
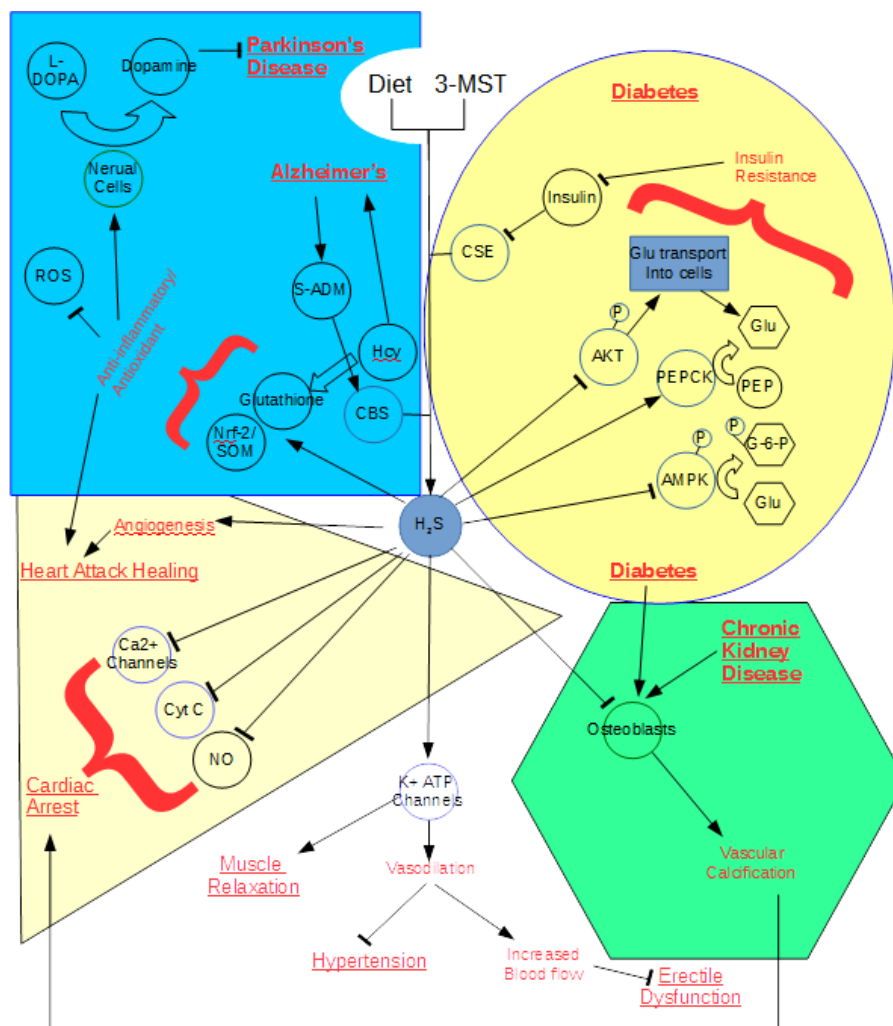
Figure 2.1. A summary of the effects of H_2S in various diseases. The yellow oval represents Diabetes, the blue rectangle represents neurological diseases, the pale-yellow triangle represents cardiovascular complications, the green hexagon represents vascular calcification and the colorless, shapeless section represents circulatory and muscular system effects. Underlined words are major physiological diseases or benefits, while non-underlined words are minor physiological effects. Straight arrows represent activation or promotion, truncated lines represent inhibition, straight bubble arrows represent transportation of the first compound to the second and curved bubble arrows represent a transformation of the original compound to the end compound. Blue circles represent enzymes, while green circles represent cells and black circles (or hexagons) represent biomolecules.

2.2. Nano-CuO Overview

CuO has been found to be a strong and reliable sensor for gaseous H_2S. This section provides a brief

overview of CuO with the intent to provide background information. This overview presents a summary of the plethora of synthetic techniques as well as the rationales for the selection of CuO as the sensor material and the synthetic methods utilized in this thesis.

Nano-particles of copper (II) oxide (nano-CuO) has been developed and worked on since the 1980s. The 1980s represents the dawn of nano-CuO research, putting out less than 50 papers in 2 decades. A significant increase in the number of publications has been observed from the year 2000 onwards. In 1986 copper removal from common copper nitrate solutions was studied[64]. In doing so, the investigators reported the production of very fine black powder – copper oxide. In 1991, Metallo Organic Chemical Vapor Deposition was used to study the superconductivity of CuO nanoparticles and their Y-Ba-Cu-O derivative films[65]. From 1991 to 1994 there was an increase in the interest in the study of CuO and as a result a significant amount of work has been done on the synthesis of nano-CuO and its various derivatives[66–71]. Since then the interest in the subject has only increased with time. This brief review will show the humble beginnings of nano-CuO research as well its modern day counterpart. It will begin with a description of the physical – chemical properties of nano-CuO. Afterwards, a brief discussion on the methods of synthesis of nano-CuO is presented and finally, a number of the applications of nano-CuO are presented, with an emphasis on biosensors.

2.2.1. Basic Chemical-Physical Properties of CuO:

First solved in 1933, the crystal structure of CuO has an unusual symmetry. CuO has a monoclinic crystal structure with c_{2h}^6 (C2/c) group symmetry giving 4 atoms per unit cell of Cu and O, but only 2 CuO atoms in the primitive cell. The Cu^{2+} ions occupy the 4c locations on the unit cell and the O^{2-} are in the 4e locations, as shown in Fig 2.2. The parameters of the CuO unit cells have been calculated and are summarized in Table 2.2. [72,73].
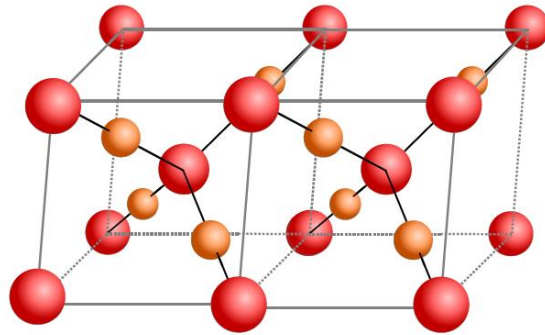
Figure 2.2. The structure of CuO. The large red balls represent oxygen and smaller orange balls represent copper[72].

.

Table 2.2: Crystallographic properties of the bulk CuO Unit Cell at 25 °C[72,73]

Quantity	Value
Space group	C2/c
Unit cell	$a = 4.6837$ Å
	$b = 3.4226$ Å
	$c = 5.1288$ Å
	$\alpha, \gamma = 90°$
	$\beta = 99.54°$
Volume	81.08 Å^3
Density	6.515 g/cm^3
Atomic Distances	Cu – O
Cu – O	1.96 Å
O – O	2.62 Å
Cu – Cu	2.90 Å

It has been established that there are no phase transitions between the temperature range of 673.15 K – 973.15 K and 1300 K – 3000 K as well as pressures of up to 700 kbar[74–76]. However, the lattice parameters of the bulk CuO monocrystalline structure increase as a function of temperature. The data is summarized in Figure 2.3.
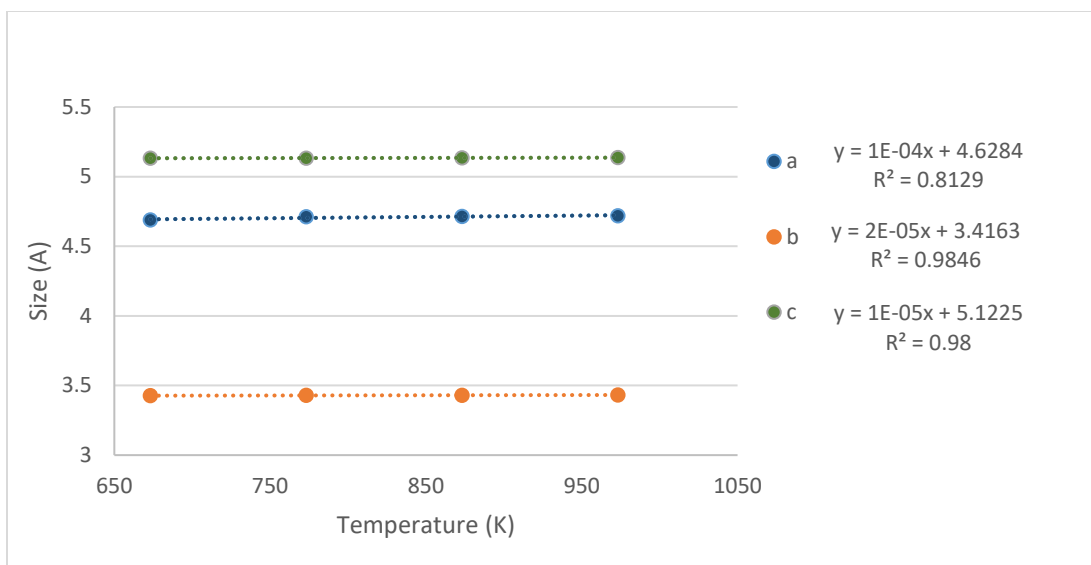
Figure 2.3. Variation of the lattice parameters a, b and c in units of Angstrom (Å) with temperature (K)[77].

2.2.2. IR and Raman Spectra of CuO

As mentioned earlier, the symmetry of the CuO molecule is C_{2h}^6 which gives a total of 12 phonons. There are three Raman active modes ($1A_g + 2B_g$), 6 infrared active ($3A_u + 3B_u$) and 3 acoustic modes ($A_u + 2B_u$). The Raman spectra shows bands at 288 cm^{-1} (A_g), 330 cm^{-1} (B_g) and 621 cm^{-1} (B_g). The largest peak appears at 288 cm^{-1}, while the 330 cm^{-1} is the smallest peak[77–79]. It has been found that a smaller grain size leads to red shifting due to size-effect interferences[80–83]. Shifted CuO peaks located at 277.5 cm^{-1}, 329.9 cm^{-1} and 610.8 cm^{-1} to the A_g, and $2B_g$ phonons respectively have also been reported[75].

2.2.3. The Electromagnetic Properties of CuO

Electric:

It has long been known that CuO is a *p*-type semiconductor with a narrow electronic bandgap of 1.0 - 1.4 eV[72,77,84–86]. Furthermore it was discovered that CuO is antiferromagnetic below 220 K and CuO deficiencies arise from Cu vacancies[72]. Interestingly, evidence suggests that the reason CuO is a *p*-type semiconductor, a semiconductor containing electron holes, is also due to this vacancy of copper atoms in the CuO material[72,87].

15

The electronic band gap of CuO depends on the crystalline size and the morphology of the structure[88]. Energies can be 1.425, 1.429, 1.447 and 1.371 eV for flower shaped, boat shaped, plate-shaped and ellipsoid shaped CuO crystal structures respectively[88]. Furthermore, a bandgap of 4.13 eV for 10 nm quantum particles and 3.02 eV for nanoplatelets have even reported as well as 3.48 eV for nanowires and 3.02 eV for nanoplatelets[81,83,89].

Furthermore, seven main surface structures of CuO have been produced, each defined by growth along a different plane. Comparisons of the various growth directions of (111), ($\bar{1}$11), (110), (011), (101), (010) as well as (100), have concluded that CuO growth along the (111) and ($\bar{1}$11) planes were the most stable surface structures[90]. The stability of these structures arises from the electronic configuration of the Cu and O atoms; in the (111) and ($\bar{1}$11) CuO surfaces, the electrostatic repulsion is minimized. In contrast, it has been found that the (100) surface has the lowest stability of the seven surface structures that were investigated[90].

Semi-conducting:

As mentioned above, CuO is a p-type semiconductor due to vacancies of Cu atoms. A semiconductor is a material that has conductivity between insulators and conductors, and are usually associated with impurities/defects. The defects either result in an increase in the number of electrons, called n-type semiconductors, or an increase the number of holes, called p-type semiconductors. Conductivity of p-type semiconductors is generally due to the holes in their valence shells rather than free electrons. CuO is a p-type semiconductor and its conductivity, 1.59×10^{-3} to 0.11 $(\Omega \text{ cm})^{-1}$, is due to deficiencies in the Cu atoms, leaving excess holes in the valence shells allowing for conductivity. As such electrical conductivity can be controlled by controlling the dopant in the CuO material. It has been found that the adsorption of oxidizing gases, such as O_2 or N_2, result in a decrease in the conductivity of CuO, similarly the adsorption of H_2O results in a decrease in the conductivity because H_2O increases the band gap and acts as a source of electrons.[72,90]. It has been found that CuO and Cu_2O are usable as ethanol detectors, showing a decrease in conductivity with an increase in ethanol binding[91]. The electrical conductivity can be controlled by the partial pressure of O_2 gas during the growth of the CuO. It was found that the resistivity of CuO increased by 1000x from 10^{17} to 10^{20} by increasing the oxygen flow from 6.0 sccm to 8.0 sccm[73] (sccm = standard

cubic centimeters per minute).

Certain physical structures, specifically grain boundaries, play a significant role in growth and conductivities. Conductivity is influenced by many parameters including structural and morphological factors, including grain size, grain boundary, full thickness, specific phase and dopants[92–96]. Moreover, the conductivity of CuO is strongly correlated to temperature and growth conditions[95]. It has been found that the conductivity is negatively correlated to the temperature, but deviates quickly from a linear model. Furthermore, an increase of conductivity from 1.59 x10^{-3} to 0.11 Ω^{-1} was reported with an increase from 200 nm to 400 nm in the grain size of nano-CuO. Moreover, there is a positive correlation between the conductivity and the thickness of CuO. It is suspected that the cause of this increase in conductivity is due to the increase of defects – increased grain boundaries and the scattering of charge carriers[96]. CuO nanostructures synthesized by a sol-gel method using copper acetate heated between 573.15 K to 973.15 K show an increase in conductivity from 10^{-6} to 10^{-5} $(\Omega\ cm)^{-1}$, which is attributed to a removal of H_2O which would otherwise resist conduction between the CuO grains. They also observed an increase in electron carrier concentration and mobility from 4.6 x10^{19} cm^{-3} to 7.2 x10^{19} cm^{-3} and a decrease in the optical bandgap from 1.64 eV to 1.46 eV[97].

Most defects in CuO have been reported along the grain boundaries. However, there is a considerable amount of debate regarding the defects of CuO. Deviances from the stoichiometry and a strong following to the stoichiometry have been reported, meaning that CuO structures with ratios of 1 Cu for every 1 O atom as well as l Cu for every 3 O atoms have been reported, along with others ratios.[72,98]. Although the discussion continues in the literature. Interestingly, certain monoclinic CuO structures are insulators at low temperatures, particularly Mott insulators, while others are not. This clearly emphasizes the need to study the various synthetic techniques of CuO and the levels of defects present[99,100].

Magnetic:
A diameter of at least 10 nm is a critical size for CuO particles to exhibit magnetic properties. Below 10 nm the magnetic properties seem to be dominated by electron spin[101–103]. Initially it was reported that bulk CuO is antiferromagnetic, but there have been contradicting reports which present the presence of a weak ferromagnetism[104,105]. Weak ferrormagnetism was found in CuO particles between the sizes of 13 – 33 nm and a Néel temperature T_N = 230 K has been reported [106]. Further research has shown that the magnetic

phase of CuO can vary with temperature[103,107–110].

2.2.4. The Synthesis of Nano-CuO

Several techniques have been developed for the effective and efficient synthesis of CuO nanomaterials. This overview briefly discusses three main methods of synthesis including thermal oxidation, solution based synthesis, and electrochemical methods.

Thermal Oxidation Method:

Thermal oxidation is the most common method of synthesis and consists of heating Cu substrates (usually foil) at high temperatures in air, oxygen or nitrogen.

CuO nanowhiskers, of lengths less than 5 μm and a thickness greater than 100 nm, have been prepared with growth along the (111) plane by heating Cu to 400 °C – 600 °C under nitrogen gas[111]. Furthermore, CuO nanowires have been synthesized through treating Cu at 400 °C to 500 °C with various oxygen flow rates[112]. Similar results were found by other investigators[113]. Synthesis of CuO nanwires on a Cu film on a Si substrate was prepared by heating at 350 °C – 550 °C for 4 hours in air and a 21% O_2 gas flow[114]. Regarding the effects of annealing time on CuO crystal growth, it was found that heating at 300 °C – 500 °C, an increasing annealing time results in longer nanowires. Catalysts have also been employed in CuO synthesis. Using a cobalt tungsten phosphide catalyst, single crystals of CuO nanowires were synthesized at 200 °C – 400 °C. It was found that the nanowires increased in length, yet not diameter due to the catalyst. However the catalyst was only effective for a maximum of 2 hours[115]. It has been found that stress is an important factor in the first step of the formation of the CuO nanowires: the formation of CuO hills and troughs[116,117]. CuO nanowires with lengths of 1 μm to 5.5 μm were synthesized by initially roughing the Cu substrate then treated at 200 °C – 500 °C[118]. The experiments have shown that the major factors affecting CuO nanostructures are the Cu substrate, the annealing time and the calcination temperature.

Solution Based Synthetic Techniques:

In contrast to the simplicity and relatively few options for Cu precursors of the thermal oxidation method, the solution based techniques offer a greater variety of precursors. Solution based synthesis techniques range from relatively easy to moderately difficult and offer a plethora of techniques and Cu precursors for the synthesis. Most, but not all, solution based methods require the dehydration of $Cu(OH)_2$ into CuO. The most common and successful wet synthetic method is the hydrothermal synthetic method.

In the hydrothermal synthetic method reactions are conducted in solutions under high pressures and above the critical temperature conditions of water[119–121]. The requirement of high temperature and pressure are obvious disadvantages to this technique, but these are offset by the advantages. Firstly, the high temperature and pressure allows for easy production of supersaturated solutions. Solutions can be supersaturated with catalysts, surfactants, etc. as one needs. Moreover, water is a cheap and well-studied solvent with an abundance of separation/filtration methods and so there are a variety of methods which may allow the removal, and thus reuse, of some catalysts. Furthermore, the hydrothermal method can be "green", with no unnecessary toxic solvents or by-products. Lastly, the polarity of water may be involved in the growth and orientation of the CuO crystals[120].

As mentioned earlier, the synthesis is generally based on a 2 step process: 1) the formation of $Cu(OH)_2$ particles from Cupric precursors and a basic solution and 2) The $Cu(OH)_2$ particles are then thermally dehydrated in an autoclave to yield CuO. The literature shows an abundance of morphologies that can be obtained using the hydrothermal technique by varying the experimental parameters, including Cu^{2+} concentration, pH, growth time, pressure and temperature. The disadvantage of the hydrothermal technique is it is incapable at studies requiring low temperatures and pressures.

CuO nanorods have been synthesized from the precursor $CuCl_2$. The results yielded nanorods with diameters between $10 - 35$ nm and a length of $0.5 - 1$ μm were preferentially grown along the [111] direction when heated at 120 °C[122–125]. In contrast, CuO microspheres and nanoribbons were successfully prepared using the precursor $Cu(NO_3)_2 \cdot 3H_2O$ in ethyl alcohol when treated at 180 °C for $2 - 24$ hours. It is believed that the rhombic structure of the CuO crystal lattice supplies the curvature of the sphere[126]. Similar results have been reported from other investigators[127,128]. Expanding on these results, oval shaped

2D CuO nanosheets and 3D nanoellipsoids have been synthesized from a solution of $Cu(CH_3COO)_2 \cdot H_2O$ heated at relatively low temperatures and various pH values. An interesting result was found in that the pH of the solution can alter the 2D or 3D structure of the nanoellipsoid and also the size of the nanostructure. The results are summarized in Table 2.3 below. The data shows that low temperatures (65 °C) and lengthy annealing times allow for the production of 3D nanoelipsoids. Furthermore, a basic pH heavily supports the creation of 2D nanosheets instead of the 3D nanoellipoids[129–131]. CuO nanostructures of various shapes have also been synthesized namely shuttle-like (leaf shaped) CuO nanostructures, polyhedrons, nanosheets and nanowires through heating a solution prepared from $Cu(CH_3COO)_2$ at 120 °C for 12 hours[132,133].

Table 2.3: Results of the production of nanosheets and nanoellipsoids[129].

pH	Temp (°C)	Time (min)	Morphology
7.5	65	5	0D nanoparticles
7.5	65	40	Almost 3D nanoellipsoids
7.5	65	1140	3D nanoellipsoid formation
7.5	85	1140	Well developed 2D nanosheets
8.5	65	40	2D incomplete nanosheets
8.5	65	1140	2D nanoribbon based sheets
8.5	85	1140	2D nanorod based sheets with sharp tips
8.5*	65	1140	Irregular nanoflakes

* NaOH instead of $NH_3 \cdot H_2O$

Furthermore, in 2008, highly crystalline CuO nanoneedles with ultra thin nanotips were reported. The synthesis procedure involved heating $Cu(NO_3)_2 \cdot 3H_2O$ at relatively low experimental temperatures between 120 °C – 180 °C for 20 - 60 hours[134]. In contrast to the nanoneedles, nanoflakes were prepared by heating $Cu(NO_3)_2 \cdot 3H_2O$ at 200 °C for 2 hours[135]. Furthermore, the effects of the size, purity and yield of the formation of CuO nanoparticles from a $Cu(NO_3)_2$ precursor were investigated through the variation of treatment temperature, annealing time, pH and concentration of the precursor. The results have shown that a temperature of 500 °C, duration of 2 hours and a concentration of 0.1 mol/dm^{-3} of $Cu(NO_3)_2$ at pH

3 was the optimal synthesis condition. The authors also reported that the morphology depends on the concentrations and temperature of the reaction[136].

Continued research on CuO nanostructures from $Cu(NO_3)_2$ and $CuSO_4$ was conducted. CuO from $Cu(NO_3)_2$ were prepared with lactic acid and also with NaOH, whereas CuO from the $CuSO_4$ was prepared using NaOH. Interestingly, the nanorods of the $Cu(NO_3)_2$ and lactic acid formed a sphere (thickness 20 – 150 nm and breadth of 100 -200 nm) instead of individual rods. In the NaOH case, those rods formed but aggregated in a random fashion rather than spherical shapes. The rods were 5 µm in length and 50 nm in diameter. In the case of the $CuSO_4$, the rods are more and less separate with lengths of approximately 5 µm and width of approximately 50 nm[137]. Nano flowers have also been reported[138]. The authors successfully created CuO nanoflowers using $Cu(C_5H_7)_2$: $Cu(AA)_2$ and $Cu(NO_3)_2 \cdot 3H_2O$ at various concentrations in water. Afterwards, the solutions were autoclaved for 22 hours at 180 °C. The results showed that both methods lead to the formation of flower like structures of CuO in single phase, but had different vibrational properties, yielding an unexpected peak at 218 cm^{-1} in the Raman spectra of the first method (utilizing the $Cu(AA)_2$). Although it is clear that this peak is from a defect in the final product, it is not entirely clear what causes it. It is suspected to be caused by either presence of the $Cu(AA)_2$ or presence of Cu_2O. For both methods, it was also found that increased concentrations of the precursors lead to an increase of grain sizes[138]. In 2011, the authors prepared a plethora of nanostructures of CuO including pseudo-flower, pseudo-boat, pseudo-plate and pseudo-ellipsoid. $Cu(NO_3)_2 \cdot 3H_2O$ and polyethylene glycol (PEG)[139]. The results show that the three greatest influencers of morphology were the reactants, the temperature of the reaction and the reaction time. The thickness of the nanostructures was between 100 – 150 nm. Plate and ellipsoid CuO nanostructures were formed using polyethylene glycol and NH_3OH while flower and boat morphologies were obtained by increasing the reaction time.

The presence of PEG affects the morphology of CuO through the formation of a Cu-PEG complex. Upon heating, the complex would deteriorate leaving CuO, and the PEG would become absorbed onto some CuO structures thus stunting its growth and causing layers to form on top of one another. Although many questions remain, these results provide an interesting starting point onto the discovery of the mechanism of CuO production[88]. Further researchers could try to determine what type of CuO surfaces are capable of absorbing PEG or if there is an unusual Cu-PEG complex formed during the $Cu(OH)_2$ phase. In another work, the authors have found that CuO is a possible detector for gaseous HCN. Using a similar procedure,

they produced microspheres composed of sharp nanorods with a band gap of 3.02 eV. They also reported that CuO nanoplates had the highest sensitivity (2.26 Hz/µg) of the flower structures, boat-like structures, nanoellipses or the nanoplates[139].

Simple nanoparticles were grown using a unique apparatus called a T-type mixer. A number of metal oxides including CuO, Fe_2O_3 and NiO were synthesized. In the procedure, water was added at a temperature of 673 K (400 °C) at 30 MPa to a starting solution of $Cu(NO_3)_2·3H_2O$ at 298 K (25 °C). This resulted in the rapid heating of the solution and arrival at supersaturated solutions past the supercritical point. At the end of the reaction, the mixed solution was cooled using an external water jacket flowing at 100 g of water per minute. The metallic oxides precipitated out of solution and were analyzed. It was found that the average particle size of CuO increased from 23.7 nm to 34.3 nm as residence time moves from 0.002 seconds to 2.008 seconds. Growth of the nanoparticles occurs through nucleation and is suspected to occur through the Ostwald Ripening process[140].

Surfactants have been used to produce specific morphologies and pores. In one experiment, investigators dissolved $CuSO_4·5H_2O$ in water followed by addition of specifically denatured alcohols heated at 30 °C. It was found that by increasing annealing time from 0.5 hours to 2 hours, CuO-ethanol go from small whisks of CuO nanoparticles to flowers of CuO. The whisks tended to aggregate and were less than 100 nm in length and less than 30 nm in width and the flowers were several micrometers in diameter and grew in all directions. Very similar results were found for the rest of the surfactants[141].

The Electrochemical Method of Synthesis:

The electrochemical method is defined by its dependence on redox reactions initiated by electric currents. The parameters for these reactions are dependent upon the voltage, current, temperature and concentrations of the reagents and the protocols are much less involved than the thermal oxidation and the solution based methods. Furthermore, interestingly, often it does not require the Cu_2O or $Cu(OH)_2$ intermediates as seen in the thermal oxidation or solution based methods, but contain similar intermediates.

A novel electrochemical technique was developed to produce CuO. The experimental procedure was as follows: A Cu anode was submerged in tetraoctylammonium bromide in acetonitrile (75%) and

tetrahydrofuran (25%) at room temperature. The cathode used was platinum and a constant current of 5 mA cm^{-2} was applied under oxygen atmosphere. The result of the experiment produces CuO nanowires of various lengths of 3.5 nm, 6.5 nm and 10.0 nm. He also described a blue-shifting of the optical band gap of 1 eV to 2.35 eV due to quantum confinement[142]. An improvement on the above method was made by increasing the temperature to 25 - 30 °C and increasing the pH to 13. The authors report CuO crystal growth in the [010] direction[143].

Synthesis of CuO nanospindles were reported using a Cu cathode and stainless steel anode in a NaNO$_3^-$ solution. The reaction was performed under constant currents of 5, 10 and 15 mA cm^{-2} at room temperature. The results revealed that there were several easily adjusted reaction parameters: the reaction media (electrolytes and electrolyte solution) and current density. As for the influence of the reaction media, it was found that that an addition of ethanol effected the diameters and aggregation of the nanospindles. NaNO$_3$ in dH$_2$O gave nearly uniform nano-splindles with blunt ends of about 80 – 100 nm in diameter and 200 – 300 nm in length. Moreover, it appears these nanospindles aggregate together to form bunches. However, addition of ethanol produced nanospindles with diameters of 20 – 50 nm and equal lengths as before. Moreover, they seem to be more "individual" rather than aggregated. The growth direction of both methods seems to be along the ($\bar{1}$11) plane. Current denisy has a profound impact on the morphology. By increasing from 5 mA to 10 mA to 15 mA cm^{-2} to 20 mA cm^{-2} the morphology changes from nanospindles to nanoplates. At 5 mA cm^{-2}, CuO nanospindles are formed and at 20 mA cm^{-2} CuO nanoplates are formed. However, at 10 and 15 mA cm^{-2}, both CuO and Cu$_2$O were observed. These results are inspiring in that they state that even simple changes can easily lead to different morphological forms of CuO, especially simple ones including change in current density. The reaction with NaNO$_3$ gradually changed colors from clear and colorless to blue to dark-green and finally to black precipitates. This clearly indicates that the reaction occurred in multiple steps. Firstly, the blue color is characteristic of Cu(OH)$_2$ and the dark green color may be Cu$_2$O. Regardless, the black precipitates are the final product, CuO[144].

Synthesis of CuO honeycombs were reported using a two – step electrochemical deposition process. A Cu foil cleaned with acetone and HCl was placed in a 3 M KOH solution containing CuSO$_4$·5H$_2$O. Afterwards the solution was aged for a week at 15 °C. Throughout the week, the solution turned from blue to dark-brown, suggesting the creation and degradation of Cu(OH)$_2$ and the brown-black color is characteristic of the CuO. The Cu(OH)$_2$ precipitate was then dried at 80 °C for 12 hours. The proposed mechanism of the

reaction is the removal of Cu^{2+} ions from the Cu substrate and then the formation of $Cu(OH)_2$. Subsequent to the addition of NH_3, the $Cu(OH)_2$ transforms into an orthorhombic structure, which then slowly decomposes into CuO[145].

CuO nanorods were also synthesized on glass substrates using the electrochemical method. The experimental parameters studied in this investigation were the deposition time and the voltage. The experimental setup was as follows: Cu plate ($0.5 cm^3$ x $2.2 cm^3$ x $0.16 cm^3$) and a steel plate, of similar size, attached to a glass substrate dissolved in deionized water were subjected to a constant current while varying the voltage ($10 - 30$ V of direct current) or the deposition time ($1 - 8$ hours). The voltage was varied by increasing the distance between the plates. The results showed that an increase in the distance (i.e. increase in voltage) is correlated by a decrease in the diameters of the nanorods (from 27 ± 5 nm to 25 ± 5 nm) and a decrease in the thickness (from 23 ± 3 nm to 1 ± 3 nm). Increasing the deposition time causes increasing aggregation. With only 1 hour of deposition, mainly nanorods are found whereas 8 hours resulted in nanorods and bundles. By increasing the reaction time to 8 hours, the nanorods began to aggregate and form nanobundles instead of nanorods. The maximum of 635 nm thickness with a minimum thickness of ~25 nm.

Furthermore, CuO nano-flowers were synthesized using the electrochemical method. The experimental setup included a glass discharge with two Cu electrodes in distilled water (dH_2O) supplied with 32 V. They investigated the effect of the distance between the plates by setting the electrodes at 1, 3, 5 and 7 mm distances and then producing a plasma discharge, the voltage and current were kept constant. Unfortunately, CuO and Cu_2O spectra were both observed using the XRD spectra. The percentage of CuO to Cu_2O was roughly 66% and had no dependence on the gap between the electrodes. As for the morphology, each of the experiments resulted in micro-flower nanostructures. The nanostructure was composed of nanorods over the range of $0.5 - 1$ μm and the nanorods thinned towards the top, as compared to their base. The major benefits of this method include an ecologically friendly technique that is cost effective. However, before it's widespread usage, it must be able to make many other shapes[146].

2.2.5. The Mechanisms of Growth

The Ostwald process:

The Ostwald ripening process was discovered in 1896 by Wilhelm Ostwald. The process describes the spontaneous growth of crystal structures from smaller crystallites in a solution[147–151]. The process has been extended to explain crystal growth in sol gels as well. Briefly, the Ostwald process is based on the concepts of Gibbs energy and thermodynamic stability: surface particles have higher total Gibbs energy than their internal counter-parts, thus making larger particles with higher internal particles–to–surface particle ratios, more thermodynamically stable than smaller particles.

The Ostwald process has been very well studied for the growth of many crysals including CuO[83,127,152–154]. Through the Ostwald process, well aligned CuO nanoplatelets were grown with only slight variations in thicknesses (50 – 80 nm), width (150 – 250 nm) and length (0.8 – 1.5 µm). The growth process for the nanoplatelets was 1) dissolving of atoms into solution, 2) spontaneous attachment of atoms to large nanopatches 3) the CuO nanoflakes serve as seeds for the nanoplatelets, and 4) atoms spontaneously leave the small nanopatches and attach themselves to the nanoflakes to form the nanoplatelets[83,154]. Synthesis of CuO as long as 6 µm have been reported via the Ostwald ripening process for the growth of smaller single crystals and an aggregation of these smaller crystals, via Van der Waals forces, for the production of the final plates[152].

Aggregation Mechanism of CuO:

Work by many authors, have shown that monoclinic CuO crystal growth stems from smaller crystals through aggregation[129,131]. The aggregation method describes the growth process of crystals which come together due to Van der Waals attraction between the crystals. Typically, the smaller crystals grow through another process such as the Ostwald ripening process described above and then aggregate together to form the final structures.

The production of 3D monocrystalline architectures using CuO along the (001) direction was done using an aggregation method[131]. A hydrothermal route was used under varied reaction times. Both authors describe methods to produce highly oriented CuO nanoplatelets using the aggregation method[83]. As mentioned earlier researchers were motivated to develop an environmentally friendly technique to develop

CuO nanostructures. They succeeded in creating CuO plates using a hydrothermal technique using microwaves. The methodology was a typical reaction of 1M NaOH and 2.5 x10^{-3} mol of $CuCl_2 \cdot 2H_2O$. The following solution was heated and autoclaved in a Teflon autoclave at 130 °C for 30 mins at 294 kPa. The washed solution was then subjected to drying at 60 °C for 5 hours. The Ostwald ripening process is responsible for the formation of the larger CuO platelets from smaller CuO nanoparticles. It is thought that microwaves increase the vibrations of the $Cu(OH)_2$ molecules, causing the nanoparticles to heat. The increase of thermal energy causes a weakening of the hydrogen bonds which destabilizes the $Cu(OH)_2$ structure and increases water loss. Then the smaller crystals then aggregate together to form larger plates[152].

The synthesis of hollowed microspheres of CuO, via a "green method", has also been reported. Most methods required toxic raw materials for their production and caused contamination of the microspheres. The method of synthesis was to dissolve $Cu(CH_3COO)_2 \cdot H_2O$ in dH_2O, forming $Cu(OH)_2$ which is then autoclaved at 120 °C for 24 hours and subsequently cooled to room temperature. The CuO was purified by washing with dH_2O followed by vacuum drying at 150 °C. The heating times were adjusted between 12 hours and 24 hours to test the effects of the experimental time on the morphology. The morphology of the CuO structures was that of microspheres. Closer inspection of the microspheres revealed nanorods of width 5 – 20 nm oriented perpendicular to the microspheres The authors ascribed the formation of the microspheres to the aggregation method, asserting that the nanorods were formed through the Ostwald process, but then aggregated to form the microspheres[127].

The Dehydration Method:

The third method to discuss is the method of dehydration. Nanosheets are the primary example of the dehydration method since they could not be formed by the above two processes. Nanosheets of CuO are thin pieces of foil made up of CuO molecules which grow in a particular orientation. Inherently, the production of nanosheets could not be due to the Ostwald process because of a few reasons. The first reason is that the Ostwald process depends on the difference in thermodynamic stability of the internal particles as compared to the surface particles. In the case of nanosheets, there is a significantly higher percentage of surface particles and thus much less internal particles, thus making the nanosheets unstable from the perspective of the Ostwald process. Furthermore, the Ostwald process generally develops near-spherical particles (symmetrical particles), whereas in nanosheets the growth is directional. Secondly,

nanosheets could not be due to the process of aggregation either since aggregates are pieces of differently oriented crystals merging into one. Nanosheets, however, were found to be single directional.

The simplest process of nanosheets and nanoribbon formation is via the dehydration process. Under alkaline and oxidative conditions, Cu becomes Cu^{2+}, and the alkaline solution favors a square planar formation of $Cu(OH)_2$ along the [100] direction. Subsequently, the long polymer chains attach to each other to form lengthy 2D structures. These polymers can stack on top of each other using hydrogen bonding (H-bonding) to form 3D structures. However, in highly alkaline environments, the H-bonding may become weak and thus the 3D structures begin to deteriorate. The deteriorating 3D structures become 2D structures that roll to form tubes. Finally, heating the polymeric $Cu(OH)_2$ forms CuO nanosheets through the process of olation[127,155–159].

Stress and Grain-boundary Diffusion:

Most of the above methods correspond to wet synthetic methods. However, another train of thought, thermal oxidation, can also be utilized for the formation of CuO crystalline structures. Despite the numerous benefits of the thermal oxidation method, the mechanism of crystallite growth is shrouded with uncertainty. One of the most famous synthetic methods has been the Vapor-Liquid-Solid (VLS) method, but it has been discredited as the method of formation for CuO preparation by thermal oxidation by many researchers[112,116,160–167].

The VLS method is a growth mechanism of 1D structures of uniform diameters such as nanowires. It begins with a metal catalyst at the tip of the nanowire which then adsorbs vapors of a compound to increase the local concentrations to the level of supersaturation. Subsequently, the compound crystalizes between the metal catalyst and the metal substrate and forms the 1D nanowire structure. Investigations on the nanowires formed from the thermal oxidation method and discovered that the wires are thinner at the tip in comparison to the base. Moreover, they were not able to detect the metal catalyst at the tip of the nanowires[116]. It has been reported that the diameter of the nanorods was related to the oxygen flow rate and the annealing temperature. Moreover, they ascribed the CuO formation to the changes of the volume and structure causing compressive and relaxation stress. By heating copper foil at high temperatures (300 °C – 400 °C) for varying lengths of time under an oxygen flow rate and taking images at different stages, it was discovered that under all conditions the first stage of synthesis was the formation of hill and

valley structures at grain boundaries. Upon further heating, the hills and valleys become triangular and grow in size. These new triangular shapes are a combination of Cu_2O and CuO crystallites. The cause of the triangular shape is thought to be the result of the difference in the crystallographic parameters of CuO (monoclinic) and Cu_2O (simple cubic) and thus there is a significant amount of stress on the boundaries of the triangular prisms. Upon further oxidation, the stress continues to increase until a critical point is reached. After this critical point, nano-CuO rods are produced to reduce the stress. Thus, the top layer of the Cu substrate is entirely covered by the CuO nano-rods. The results were an interesting find; heated at 400 °C for 5 minutes and 350 °C for 30 minutes produced successful results. However, heated at 350 °C for 10 minutes, or a lower temperature, did not produce CuO nanowires[112].

Furthermore, the thermal oxidation of Cu foil at various annealing temperatures has lead to many interesting conclusions. Growth was found in the [010] direction. Cu was heated at various temperature between 500 – 800 °C under a steady oxygen flow for 4 hours. It was found that the optimal growth temperature between 600 – 700 °C, is 675 °C. It was found that CuO nanowires could grow in both crests and troughs of CuO films covering the Cu. However, there is a distinct difference in the length and thicknesses of the CuO nanowires; nanowires in crests ("hills") are thinner yet longer whereas in troughs ("valleys") they are thicker and shorter. In both cases, the thickness of the nanowires at the bottom is greater than at the tips. Lastly, they established that the CuO nanowires are composed of smaller crystalline structures of CuO. These results agree with other investigators' results[160].

Moreover, Cu (though not restricted to Cu as Fe, Zn and other metals can also be fabricated using this method) boat shaped micro-containers on glass substrates were fabricated and exposed to oxygen flow while being heated at 400 °C for 3 hours. The glass substrates of 1.1 mm thickness were washed and cleaned followed by an ultrasonic bath and dried with nitrogen. A thin layer (2.5 µm) of photoresist was spun on and exposed to UV light through a mask. Successively, Cu is deposited by direct current (DC) sputtering to a thickness of 400 nm. Then the photoresist is removed using acetone, leaving the Cu boat on the glass substrate. As it turned out, CuO nanowires were obtained only on the inner, flat surface of the boats. It is thought that as the oxygen flowed, a layer of CuO will form on both the inside and outside of the boats, causing an expansion of the boat. On the inner side of the boat, the expansion brings the CuO molecules closer and an increase of concentration is observed. Whereas, the outer surface just experiences tensile stress and the CuO become more distant. Due compactness of the film, the preferred direction of

growth is normal to the film, the [110] direction. Eventually an increase in concentration leads to a significant increase in CuO nanowires along the flat surface on the inner of the boats. In contrast, the tensile forces at the outer surface prevents the formation of nanowires[161].

Some researchers have investigated the mechanism of CuO formation in the thermal oxidation method. They found that compressive forces present at the grain boundary at the CuO and Cu_2O crossing point were responsible for the formation of the CuO nanowires. They also presented a kinetic model of CuO formation focusing on grain boundary diffusion as the predominant factor for the continuation of growth. Briefly, they proposed at the copper surface was originally coated with Cu_2O and then completely covered again with a thin layer of CuO. It is in this configuration that, under heat, there are compressive forces which cause Cu^+ ions to migrate from the Cu source to the grain boundaries of CuO and Cu_2O, due to the defects. It has been shown that rougher surfaces can significantly increase the CuO nanowire formation rate. It is thought that by roughing the surface of the Cu, then smaller grains of CuO and Cu_2O are produced implying that perhaps Cu is better capable of transporting along grain boundaries for enhanced nanowire formation[168].

CuO was formed using the thermal oxidation method using annealing temperatures between $600 - 1000\ °C$ with different purities of oxygen gas at a final pressure of 0.1 MPa. It was found that the growth of CuO was not parabolic yet grew slowly at the beginning and then maintained an almost consistent thickness throughout. It was found that the CuO remained as whiskers and did not develop further to become plates or long wires. The mechanism used in this synthesis is also thought to be based on grain boundary diffusion of Cu atoms[167]. Similar reports have been provided by many other researchers[117,168–171].

The Self-Diffusion Method:
Lastly, a novel technique for the fabrication of one-dimensional CuO nanoneedles was developed and provided a novel explanation of the process. The synthesis was done using copper electrodes in an electrolytic solution made up of cupric sulfate, boric acid, saccharin and sodium fluoride adjusted to a pH of 1.0 using H_2SO_4 and KOH. By sending electrical pulses, they could produce CuO nanoneedles. The proposed mechanism for CuO nanoneedle development is one of self-diffusion. Initially, local electric fields are established by oxygen atoms at the solid/gas interface which cause the diffusion of copper ions (from the substrate) to accumulate at this interface. When the temperature rises above the critical value,

the Cu ions react with the oxygen ions, forming a Cu_2O precipitate. The Cu_2O then acts as a catalyst allowing more Cu and O ions to diffuse within itself. In doing so, the CuO nanoneedles are produced. However, many details are still lacking including why Cu_2O is produced first and why subsequent diffusion of Cu and O result in the formation of CuO rather than more Cu_2O.

2.1.1. The Applications of Nano-CuO

Nano-CuO has been studied for a wide range of applications, either in its pure form or as a dopant, including as biosensors, H_2S sensors, nanofluidics, superhydrophobic surfaces, photodetectors and solar cells and purification of water of arsenic and organic pollutants[172–183]. There is enough work for each of these topics to have their own review, however this review will focus mainly on the applications of CuO as a sensor.

CuO has been used as a catalyst for many reactions. This includes as a heterogeneous catalyst for complete combustion, as a cathode in an electrochemical cell with elements such as lithium[184–186], and solar-cell and solar energy transformation[174–178].

General Biosensors:

Biosensing is a vast and growing field of metabolite detection. There are two main branches of biosensing: external biosensors and implantable biosensors. External biosensors generally rely on test strips which measure the metabolite (e.g. glucose) from a small sample of blood. A common example of an external biosensor is a diabetes blood glucose monitor. This method is simple, cheap, easy to use, less invasive and easy to upgrade, however, it causes a small amount of daily discomfort for every use and it depends on the patient to take the measurement – if they forget or lose it, the measurement is not taken. In contrast, implantable biosensors are surgically placed inside the body and measure continuously. There are advantages and disadvantages of both methods and many researchers aim to improve both methods. The main disadvantages of the implantable biosensors are biofouling (degradation), foreign body response, sensor drifts, lack of temporal resolution and difficulty to upgrade (the device would have to be surgically removed and then surgically replanted). The main benefits of these devices are constant measurements, statistically significant number of measurements leading to significantly more accurate measurements and lack of daily (or hourly depending on the patient's needs) discomfort. Two examples where implantable

biosensors maybe more advantageous are cases where a patient is in critical condition and constant monitoring is crucial to their health and the other example is of elderly patients who may not remember to take measurements so frequently[176–178,187–196]. A debate continues in the literature as to which method is more useful.

CuO based Glucose Sensors:

Biosensors for glucose detection are extremely important for clinical monitoring of glucose in the blood as well as the food industry and environmental monitoring. It has been said that all biosensing can be traced back to the search for a viable glucose detector[172,173]. Regarding the clinical relevance of glucose detection, diabetes is a growing problem for our population. The current approach for glucose measurements is an electrochemical method stemming from the catalytic oxidation of glucose (from the blood) into gluconic acid by the enzyme *glucose oxidase*. A by-product of this reaction is hydrogen peroxide, which is then oxidized to O_2 by an oxidizing electrode. The amount of current produced is correlated to the moles of glucose oxidized, and thus a measurement of the glucose concentration in the blood is obtained. Many researchers have developed nanodevices to add onto the electrode to increase sensitivity[197–199].

However, due to the shelf-life of *glucose oxidase* and its highly specific storage conditions (i.e. pH = 7, physiological osmolality, etc.) result in high cost of production of the glucose test strips. Moreover, the enzyme must be protected from its own by-product, as high concentrations of H_2O_2 can denature the enzyme. Furthermore, the current technology uses reactions with relatively slow kinetics and/or require large voltages both of which decrease the specificity of the sensor [197,200].

Due to these limitations, researchers have developed electrochemical biosensors without the use of enzymes. Biosensors based on metals, carbon nano-tubes, conductive polymers, and transition metal oxides were extensively tested. A one-step production of 1D nanorods has been reported from potassium and sodium nitrates and CuO nanoflowers from sodium and potassium hydroxides. The results showed that composites of the nanoproducts with the graphite electrodes were both more sensitive than the graphite electrodes by themselves. The nanoflowers were the most sensitive, however they have a small linear range due to slow electron transfer and possible contaminants. The nanorods on the other hand had an equally low detection limit (4 μM) but were linear over the range of 4 μM – 8 mM of glucose

concentrations. The only drawback to this experiment is that the presence of dopamine and ascorbic acid were required to obtain these results. However, it is noteworthy to point out that the storage and handling conditions of both of these compounds is easier and cheaper than that of glucose oxidase[201].

An ion based method was developed to produce 2D CuO nanoleaves[202]. Cu^{2+} ions were used as the starting material through successive reactions in the presence of sodium oleate. Although nanoleaves were the main products, it was also found that further incubation in the sodium oleate solution produced some 1D nanorods on the tops of the nanoleaves. The resulting nanoleaves were then added to an electrode of naffion and a glassy carbon electrode and were tested against a glucose/sodium hydroxide solution. The sensitivity of the electrode was found to be 26.6 μA $mmol^{-1}$. The response was linear over the range of 10 μM to 7.3 mM. Unfortunately, the testing was done under a heavily basic solution, rather than at physiological pH. However, the results show that monitoring glucose with CuO is possible[202].

Researchers have developed an electrode utilizing CuO nanowires. CuO nanowires were synthesized by heating Cu nanowires at 400˚C for 5 hours. Then the CuO was suspended in ethanol (5 mg/mL) before being dropped onto a cleaned glassy carbon electrode followed by addition of 20 μL of Naffion. The resulting nanowires had an average diameter of 200 nm. The resulting electrode was then utilized to measure glucose in a highly basic solution of sodium hydroxide. The explanation of the increase of voltage as the concentration of NaOH increases is due to the fact that the hydroxide ions allow for a greater increase in the aniodic current transfer during the catalytic oxidation of glucose. The resulting electrode has a limit of detection of 2 μM at a voltage of +0.55 V. The authors then utilized their CuO glucose detector to measure glucose concentrations in human serum. The human serum samples were injected with 5 mL of 50 mM NaOH to increase the pH before measurement. The result of the comparison between commercially available glucose detectors and the CuO detectors are shown below in Table 2.4 at +0.3 V[200]. The average accuracy of the CuO sensor as compared to the commercial sensor is 1.01%. However, further work must be done to ensure that the measurement is accurate over a wide range of blood sugars. The glucose measurements were obtained over the range of 6 – 7.5 mM, whereas blood sugar can range from less than 4 mM to greater than 12 mM (in extreme conditions)[172].

Table 2.4: Comparing the results of glucose concentration measurement by a CuO electrode with a commercially available electrode in an alkaline solution at +0.3 V[200].

Sample	[Glucose] (mM) from CuO sensor	Relative Standard Deviation of CuO Sensor (%) (N=5)	[Glucose] (mM) from commercial sensor	Percent Accuracy of CuO Sensor (%)
1	6.50	2.4	6.3	1.03
2	6.52	4.2	6.5	1.00
3	6.78	2.1	6.5	1.04
4	6.54	2.2	6.4	1.02
5	7.45	2.3	7.8	0.96

Other researchers have used CuO nanoparticles along with multi-walled carbon nanotubes[203]. In this procedure, carbon multi-walled nanotubes were prepared using a tube reactor heated to 800 – 900˚C and then a quartz plate was added inside under N_2 gas flow. In a separate glass bottle, N_2 was bubbled in ethylenediamine at a flow rate of 500 sccm to form the "feeding gas" with 8% ethylenediamine. The feeding gas was then put into the reactor and reacted for 5 – 45 mins. Then cooled to room temperature under ambient N_2[204].) The CuO was added to the multi-walled carbon nanotube via Cu sputtering. The Cu was oxidized to CuO by oxygen at 100 mL min^{-1} O_2. It was determined from the XRD spectra that all of the Cu was oxidized to CuO. The resulting CuO/multi-walled carbon nanotube was tested in alkaline solution made with 0.1M NaOH. The sensor was linear over the range of 0.4 µM to 1.2 mM glucose with the sensitivity of 2596 µA mM^{-1} cm^{-2} with a detection limit of 0.2 µM. Further worked on human serum samples, 40 µL of serum samples were added to 10 mL of 0.1 M NaOH and recorded to +0.4 V. The results of the tests have shown that there is a 95% accuracy. The results of the above mentioned CuO electrode are tabulated in Table 2.5[203].

Table 2.5: Results of the measurements of the CuO with multiwalled carbon nanotubes.

Sample	Concentration of Sample (mM)	Relative Standard Deviation (%) (N=3)	Measured Concentration (mM)	Recovery (%)
1	12.3	1.7	11.93	97
2	5.0	4.3	4.90	98
3	4.8	3.8	4.61	96
4	5.4	1.3	5.29	98
5	4.9	1.9	4.66	95

CuO Based Cholesterol Sensor:

In 2015, a ZnO – CuO matrix capable of sensing cholesterol levels was synthesized. The electrodes were capable of detecting free cholesterol over the range of 0.12 – 12.93 mM, with sensitivity of 680 µA mM^{-1} cm^{-2} and the total cholesterol concentration over the range of 0.5 – 12 mM with a sensitivity of 760 µA mM^{-1} cm^{-2}. The most promising aspect of this electrode is that the response time is only 5 seconds. The ZnO – CuO composite thin film was made using a pulsed laser deposition technique. The two parameters that were studied were pressure (50 – 500 mT) and temperature (25 – 400 °C) giving the optimal parameters of 100 mT and 300 °C. The ZnO and CuO composities were deposited onto IT/glass using a pulse rate of 10 Hz and $\lambda = 266$ nm sequentially to a thickness of 120 nm. Finally, the composite matrix was annealed at 300 °C for 2 hours. The main purposes for the incorporation of CuO was to increase the conductivity of the electrode. ZnO has a DC conductivity of 1.95 x10^{-6} Ω^{-1} cm^{-1} while ZnO – CuO has 4.8 x10^{-6} Ω^{-1} cm^{-1} In order to measure cholesterol, ChOx was added to the ZnO – CuO electrode electrostatically and thus becomes absorbed via the physical adsorption technique[205].

However, different methods of cholesterol and glucose detection have been proposed. A rapid fluorescent method using luminol-CuO nanoparticles with H_2O_2 has shown to be effective. Cupric oxide was prepared by a reaction of Cu(As)$_2$ with glacial acetic acid with 4 g/mL NaOH heated at 80 °C. When the pH reached 6.0 – 7.5, CuO spontaneously precipitated and were purified by centrifugation, washing (ethanol and dH$_2$O) followed by air drying at room temperature. The powder was then further annealed at 400 °C for an hour in order to yield the nanoparticles. The morphology of the nanoparticles was spherical with diameters between 24.2 – 33.2 nm. To test with glucose or cholesterol: two solutions were made, the first involved 200 µL of luminol with the CuO nanospheres and the second was made using 250 µL of glucose (or cholesterol) and 250 µL of glucose oxidase (cholesterol esterase and cholesterol oxidase) in a 0.1 M phosphate buffer in a dark cell. The first solution was incubated at room temperature for 20 minutes following its preparation and the 200 µL of the second solution was added. The concentration of measurement for glucose 1.2 x10^{-6} – 1.0 x10^{-3} M (R^2 = 1.00) with a detection limit of 7.1 x10^{-7} M and a range of 2.5 x10^{-5} – 7.17 x10^{-3} M (R^2 = 1.00) with a detection limit of 6.4 x10^{-6} M[179]. Similar work was done by other researchers[206–208].

Lastly, CuO nanowires were also used as cholesterol sensors. Unlike the above mentioned methods, pure

CuO was used as the detector. The authors grew CuO nanowires in along the [010] direction using the hydrothermal technique on gold coated glass substrates using $Cu(CH_3COO)_2 \cdot H_2O$. By dissolving $Cu(CH_3COO)_2 \cdot H_2O$ into methanol and then added a solution of KOH (also dissolved in methanol) dropwise while heating to 60 °C and continuous stirring. The solution forms the characteristic blue of $Cu(OH)_2$. The $Cu(OH)_2$ solution was spin coated onto the gold coated glass substrate before annealing at 120 °C for 20 minutes with an equimolar solution of 0.025 M hexamethylenetetramine and copper nitrate hemi pentahydrate. Afterwards, the solution was again heated at 80 °C for 2 – 6 hours. The CuO was then washed with dH_2O. To prepare the cholesterol detection technique, *cholesterol oxidase* was electrostatically attracted to the CuO using the dip coating technique at a pH of 7.3. The cholesterol sensing was done using the CuO – cholesterol oxidase electrode. The detection limit of the sensor was 1.00×10^{-3} mM with a linear range of $5.00 \times 10^{-3} - 5.00 \times 10^{0}$ mM with an R^2 value of 0.99 and a slope of 33.88 mV/decade in a 0.1 mM PBS buffer at pH =7.5. The response time for the sensor was less than 10 seconds. Furthermore, the CuO nanowires showed indifference to the concentration of glucose, uric acid, urea and ascorbic acid – it only responded to the cholesterol[209].

CuO Based Gas Sensors:

CuO is intrinsically a cheap, *p*-type metal oxide. In general, *n*-type metal oxides behave differently from *p*-types in that *n*-types have mobile electrons whereas *p*-types have mobile holes which allow them to conduct. The absorption of gasses complicates this simple picture. Freshly prepared CuO is capable of conduction, however, if left in air for long enough, it will decrease in conductivity. It is thought that oxygen molecules are adsorbed into the CuO with time and once adsorbed they form oxygen ions (O^-, O^{2-}, O_2^-). The oxygen ions then negatively charge the CuO and cause an increase in electrons and decrease in holes. This results in a decrease in the conductivity of CuO. In contrast, when exposed to an oxidizing gas e.g. NO_2, H_2S, etc., the gas relieves the excess electrons, thereby increasing the holes and restoring the conductivity of CuO. Gas testing have been done with many different gasses including organic gases such as ammonia, cyclohexane, 1,2-dichloroethane, formaldehyde, methanol, acetone, ethanol and propanol[210,211], CO[180–183], NO_2 [182,212], NH_3[213], HCN[214], petroleum[215], Cl_2 and Cl^- (*aq*)[215], H_2 (g) [215], oxygen[211,182,183,212–216] and water[216]. This review is most focused on the H_2S[215], however for convenience the references of other gases are provided and the curious reader is encouraged to read through the articles.

CuO Based H₂S (*g*) detector:

CuO nanowires have also been utilized, prepared by an *in situ* micromanipulation, to measure gaseous H₂S. CuO nanowires were fabricated by heating copper foil to 500 °C for 5 hours. The measured nanowires were 80 – 200 nm in diameter. After oxidization, the CuO nanowire foil was cut into squares of 2 mm x 2 mm. To test for the H₂S, the 2 mm x 2 mm CuO foil was taken and pasted on to a copper plate. The conductivity of CuO was measured during exposure to H₂S at different rates (500 ppb, 1 ppm, 5 ppm, 10 ppm, 50 ppm, 100 ppm and 1000 ppm) at room temperature and at 160 °C. It was determined that no saturation was observed for concentrations at any concentrations lower than 100 ppm. It was also found that the current response was unrecoverable at concentrations over 5 ppm, due to the formation of CuS. Consistent with other researchers, it was determined that CuO is highly selective for H₂S in comparison to H₂, CO and NH₃[217].

CuO leaf-like nanosheets have also been used for the selective H₂S detection in an environmentally friendly method, using CuSO₄·5H₂O as a precursor for a wet synthetic method. The 0.2 mM CuSO₄·5H₂O was reacted with 0.08 mM KOH were mixed and 300 mL of 13.8% of ammonia was added. After filtration, the Cu(OH)₂ was heated, incubated over night at 60˚C and then calcined at 500˚C for 1 hour. Concentrated H₂S and air were mixed and then exposed to the substrate. Before measurements, the chambers were purged with air for 0.5 hours. The resistivity of CuO when reacted with H₂S was tested at various levels of relative humidity were tested (10%, 30%, 50%, 70% and 90%) as well as different substrate temperatures (90 °C, 140 °C, 190 °C, 240 °C and 300 °C). The linear range of the detection was from 0.880 μM to 35.2 μM (30 ppb to 1.2 ppm) with a detection range of 58.7 nm (2 ppb), with a signal to noise ratio of 3:1[218].

Combinations of various synthesis techniques have also been employed to produce CuO sensors. CuO nanowire based sensors used a thermal oxidation combination of an electrodeposition technique, dielectrophoresis and thermal oxidation. The CuO nanowire was created in several steps. In the first step, orange-red Cu nanowires were grown inside hollow polycarbonate membranes which were coated with a thin layer of Ag on the reverse side. On the front side of the polycarbonate, was a glass tube filled with copper plating solution. The cathode used was a Cu plate. A constant current of 2 mA was applied through a platinum electrode and a copper plate. To release the Cu nanowires, the membrane was dissolved in

dichloromethane. The nanowires were then washed and stored in ethanol. The next step was to orient the nanowires, which was done through dielectrophoresis. The Cu nanowires – ethanol solution was placed on substrate electrode under non-uniform electric field using an AC voltage. The result was that the nanowires were oriented vertically to the substrates (pointing from one electrode to the other), also the Cu wires became dark orange. The dark orange Cu nanowires were than heated at 700 °C for 4 hours to form CuO, which was dark black. The resulting nanowires had a detection limit of 73.4 nM (2.5 ppb) with a linear range of 0.293 µM (10 ppb) to 2.93 µM (100 ppb). The sensing tests were conducted for 10 minute intervals of H_2S at 100 ppb at 9 different temperatures (25 °C, 80 °C, 140 °C, 180 °C, 240, 280 °C, 320 °C, 380 °C and 420 °C). It was found that the highest resistance occurs at 180 °C[219].

Nano-spheres have also been used for H_2S detection. CuO hollow spheres with 3 types of pores were fabricated; the first are the quasi-micropores (1.0 – 1.2 nm), the second are the mesopores (5 – 30 nm), and the last are the macropores (2 – 4 µm). The spheres were created using a wet synthetic method involving 3 mL of 0.4 M $CuSO_4·5H_2O$ and 1 mL of 0.48 M KOH mixed with 0.9 mL ammonia and 15 mL of dH_2O. The resulting $Cu(OH)_2$ was then incubated at 68 °C until a black precipitate was seen. Then the black precipitate was centrifuged and washed with dH_2O. Before being utilized, the CuO was coated with Au at 500 °C for approximately 1 hour. Before measurements the chamber was purged with fresh air for 30 minutes. Then H_2S was introduced to the system via a microsyringe at different temperatures (90 °C, 140 °C, 190 °C, 240 °C and 300 °C). The hollow spheres were tested for their H_2S sensing capability and it was found that the limit of detection was 58.7 nM (2 ppb) and a large linear range from 0.880 µM (30 ppb) to 39.6 µM (1350 ppb). An inverse relationship between the temperature and the response was found, meaning that the 90 °C gave the largest response and 300 °C gave the lowest response, although beyond 200 °C, there was very little difference[154].

CuO thin films prepared by a spray pyrolysis technique have also been used for H_2S detection. The weight of the CuO was determined by weighing the substrates before and after. The resultant CuO nano-thin films was then tested for the reactivity against H_2S, among other gasses, at different temperatures. Four samples of CuO were created at deposition times of 10 (labelled S1), 20 (labelled S2), 30 (labelled S3) and 40 (labelled S4) minutes. The CuO was exposed to H_2S at a rate of 100 ppm at various temperatures between 200 – 400˚C. The maximum response with H_2S occurs at 250˚C and the highest response was given by S3, followed by S2, S4 and lastly S1. It has been discovered that the sensing capability of a substance is

based on the interaction of the gas and the surface of the CuO. However, interestingly, different samples (S1 – S4) react differently and give different levels of response for different gases. For example, the third sample is the most responsive for H_2S, yet the second sample was the most responsive for H_2 gas. Another important observation is that hydrogen sulfide provides a response almost two – to – three orders of magnitude greater than any of the other gasses[215]. Similar results have been found by other researchers[183,220–222].

CuO and single walled carbon nanotubes (CuO-SWCNT) were synthesized and subsequently tested for its capability as an H_2S detector. The morphology of the CuO was flower-shaped, with diameters of several micrometers, and the device had a shelf life of 1 month. The device also shows a remarkably low limit of detection of 100 ppb H_2S (*g*). The synthesis of the detector began with the preparation of the CuO nanoflowers. $Cu(NO_3)_2$ was dissolved in dH_2O while stirring. After 5 minutes $NaBH_4$ was added followed by 15 minutes of more stirring. The pH of the solution was adjusted to 2 – 3 using HCl. The solution was transferred to an autoclave and different temperatures were tested ranging from 130 – 150 °C for 3 hours. Subsequently, the solution was washed with dimethylformamide to reach pH = 7. Afterwards, 20 mg of functionalized SWCNT were added to the solution and the solution was heated again at 100 °C for 30 minutes to obtain the flower shaped nano-CuO-SWCNT. The nano-CuO-SWCNT was washed with ethanol and filtered using a 0.45 μm pore filter. To test for the H_2S sensing properties, 5 mg of the CuO-SWCNT was mixed with 50 mL of dimethylformamide, which was sonicated before being spin coated at 500 rpm for 30 seconds onto gold interdigitated arrays. The device was annealed at 90 °C. The principle of the device is: CuO will absorb oxygen gas and form an O_2^- ion. H_2S will react with the responded O_2^- to form SO_2 and H_2O. The reaction also releases 3 electrons, which will tend to move toward the SWCNT (due to the higher affinity for electrons). This will cause a decrease in the conductivity of the electrode, corresponding to the concentration of H_2S present. This work is interesting as compared to the rest as it uses a reducing agent ($NaBH_4$) and an acidic solution[223].

2.2. Raman Spectroscopy

Raman Spectroscopy is a quick, non-destructive structural identification method of characterization. Raman spectroscopy measures vibrational energy coming from inelastic interactions between photons and molecules. For wavelengths of light within the infrared and ultraviolet range, most of the interactions

occur between photons and electrons. Many of the photons interact with the molecule in such a manner that its incident and emitted wavelengths are the same, this is called *elastic scattering* or *Rayleigh scattering*. However, *inelastic scattering* occurs as well. Some photons are absorbed by the electrons such that the emitted photon contains either less or more energy. If the emitted photon has less energy than the incident photon (thus higher wavelength) it is known as *Stokes scattering.* Under this circumstance, the electron absorbs the incident photon and rises to an excited state, but upon returning down, it remains in a higher energy state than in which it began. The other possibility is for the electron to absorb the photon and rise to a higher energy level and fall to a lower level than the initial state, releasing a photon with greater energy than the incident (thus lower wavelength), and this is known as *anti-Stokes*. The difference in energy from the two inelastic scattering of the photons is converted into rotational and vibrational energy in the bonds of the molecule. Since each type of molecule is unique, thus each molecule gives off a unique vibrational spectrum, similar to a "finger print", with the intensity of the peaks corresponding to the concentration. Thus, to identify an unknown compound, one can take a reading of its Raman spectra and compare it to a library. An identical match must mean the same compound[224,79].
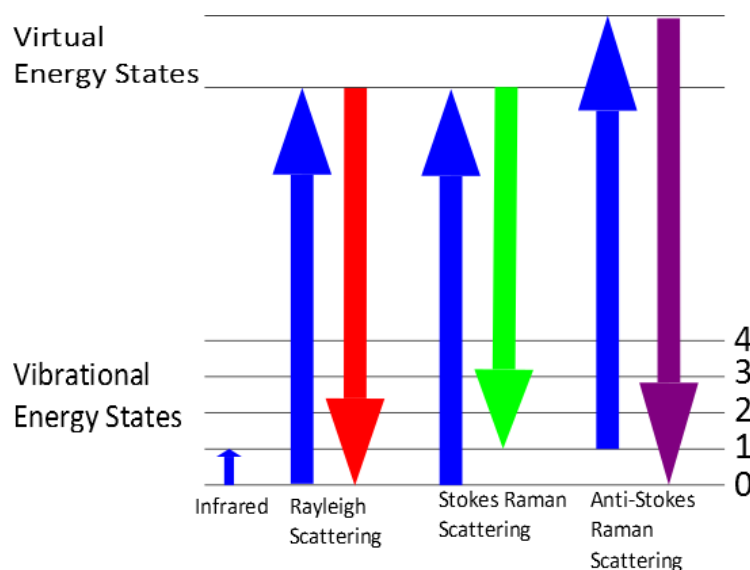
Figure 2.4. An energy diagram comparing the infrared (far-left) state and the Raman energy states. The blue arrows represent the molecules absorbing energy and increasing to higher energy states. After energy absorption, the molecule shifts to either real or virtual energy states. The infrared absorption takes molecules to higher real energy states. In Raman Spectrometry, the molecule rises to "virtual" states. The red arrow represents Rayleigh scattering, the green arrow represents the Stokes Scattering and the purple arrow represents Anti-stokes scattering. This image was adapted from www.geo.arizona.edu.

CHAPTER 3: MATERIALS AND METHODS

Introduction

In this chapter, the materials utilized throughout the experiments in this thesis are described. Some of the materials have been used more than once and sometimes the final product of one preparation may be the initial material of another preparation. For example, CuO is the final product in its own preparation and an initial material of CuS preparation. The materials include copper foil, copper pellets (<1 mm), ground copper (149 μm), copper (II) nitrate, copper (II) acetate, hydrogen sulfide gas, sodium sulfide nanahydrate, blood plasma, blood serum, magnesium sulfate heptahydrate, L-cysteine·HCl, L-methionine, sodium sulfate and sodium sulfite. The methods of H_2S (*aq*) solution preparation are by bubbling H_2S (*g*) in water and form sodium sulfide solution preparation. CuO was prepared by the thermal oxidation and wet synthetic method. The method used to analyze the uniformity of CuO or CuS was Raman spectroscopy.

3.1. Materials

Copper precursors used in this these are Cu foil (0.1 mm thickness) (Cat# 349178), ground Cu pellets (< 1 mm), $Cu(NO_3)_2$ (Cat# 305340) and $Cu(oAs)_2$ (Cat # 326755-25G) were ordered from Sigma-Aldrich, Edmonton, Canada except Cu mesh (100 mesh, 149 μm) (Cat# 90682) which was ordered from Alfa Aesar, USA. Other reagents NH_3OH (*l*) (Cat# 320145-6X500ML), $Na_2S·9H_2O$ (Cat# 407410-10 g), $Pb(ClO_4)_2$ (Cat# 205311-25g) and NaOH (Cat# S5881-500G) from Sigma-Aldrich, Edmonton, Canada. Furthermore, SAOB (Cat# 941609) from Thermo-Fisher, Mississauga, Canada. Distilled water (dH_2O) and distilled and deionized H_2O (ddH_2O) were prepared from Milli-Q water.

Sulfide measurements are made from a pH meter and Cole-Parmer ISE Silver/Sulfide electrode (Cat # 27502-41) purchased from Cole-Parmer, Montreal, Canada. Raman measurements were made with a

Renishaw Invia Reflex Raman Microscope (Renishaw, Gloucestershire, UK).

3.1.1. Preparation of H₂S solutions

Aqueous H$_2$S solutions were prepared by two different methods: bubbling H$_2$S (g) into dH$_2$O and dissolving Na$_2$S·9H$_2$O with ddH$_2$O followed by a pH adjustment.

H₂S solutions by bubbling H₂S (g):

H$_2$S water was prepared fresh everyday for the experiment. H$_2$S gas (90% H$_2$ (g) and 10% H$_2$S (g)) was bubbled into 100 mL of dH$_2$O at a flow rate of 60 mL min^{-1} for 5 minutes. The gaseous H$_2$S was generously supplied by Dr. Dalai (Chemical Engineering, University of Saskatchewan) and his lab.

Figure 3.1. Preparation of a H$_2$S through bubbling.

H₂S solutions prepared from Na₂S·9H₂O:

The second method of H$_2$S (aq) preparation involved 100 g of Na$_2$S·9H$_2$O was dissolved in 100 ml of ddH$_2$O over night. Subsequently, an aliquot was pH adjusted to 7.53 using concentrated H$_2$SO$_4$.

3.1.2. Preparations of CuO

There were two methods of CuO production used in this thesis – the thermal oxidation method and the wet synthetic method.

Thermal Oxidation Method:

CuO was prepared by heating a substrate of copper in a tube furnace, shown in Figure 3.2. The diameter of the heating tube is approximately 5 cm. Caps were placed on the ends of the heating tubes with holes with diameters of approximately 0.75 cm. The air pipe was attached to one end of the cap, and air was released from the other side. The first substrate heated in the tube furnace was a thin, shiny, orange piece of copper foil of dimensions of 4 cm x 7 cm x 0.25 mm which was cut into small pieces of 0.25 cm x 0.25 cm x 0.25 mm. The second substrate were copper pellets of the size <1 mm which were heated without further modification. The last substrate was copper mesh, <149 μm (100 mesh), which were layered on glass wool and then heated.

Figure 3.2. The tube furnace used in the thermal oxidation preparations. The end cap through which the air exits is not shown.

The Wet Synthetic Method:

Two techniques of wet synthetic method were used for CuO production. The first involved $Cu(NO_3)_2$ and NH_3OH. The bright blue crystals of $Cu(NO_3)_2$ were dissolved in dH_2O, with a drop of glycerol, and reacted with NH_3OH to the precipitate which was heated. The second technique involved $Cu(oAs)_2$ and NaOH,. similar to the $Cu(NO_3)_2$, the $Cu(oAs)_2$ was dissolved in dH_2O, mixed with a drop of glycerol, reacted with NaOH and the precipitate was heated. These compounds are generous gifts from the laboratory of Dr. Foley.

3.2. Methods

3.2.1. Preparation of H₂S solution by H₂S bubbling

H₂S water was prepared fresh every day for the experiment. H₂S gas (90% H$_2$ (*g*) and 10% H₂S (*g*)) was bubbled into 100 mL of dH$_2$O was at a flow rate of 60 mL min^{-1} for 5 minutes. It was then closed by an air-tight lid until the experiment.

3.2.2. Preparation of the concentrated sulfide solution and the weekly stock solution

To begin, ddH$_2$O was obtained by bubbling dH$_2$O (Milli-Q water) with N$_2$ (*g*) for at least 1 hour. Next, 100 g of Na$_2$S·9H$_2$O was dissolved in 100 ml of ddH$_2$O over night. After 13 hours, a clear and colorless solution of concentrated Na$_2$S (*aq*) was obtained. The pH of this concentrated sulfide solution was 13.4. Subsequently, 10 mL of the concentrated Na$_2$S solution was diluted x 1000 by 990 mL of a solution of 1:1 SAOB to ddH$_2$O to prepare the "weekly stock solution". To determine the concentration of the weekly stock solution, 30 mL of the weekly stock solution it was titrated with 0.1 M Pb(ClO$_4$)$_2$. The concentration of the weekly sulfide solution was given by the equation (derived from the manufacturer's instructions):

$$[S^{2-}](ppm) =$$

$$\frac{mol\ Pb(ClO_4)_2}{L} \cdot \frac{1\ mol\ PbS}{1\ mol\ Pb(ClO_4)_2} \cdot \frac{1\ mol\ S^{2-}}{1\ mol\ PbS} \cdot \frac{32.06\ g\ S^{2-}}{1\ mol\ S^{2-}} \cdot \frac{1000\ mg}{1\ g} \cdot \frac{1\ ppm}{1\ mg/L} \cdot \frac{V_{Pb(ClO_4)_2}}{V_{WSS}} \qquad (3.1)$$

The above equation can easily be converted to mol/L. The titration curve of the 0.1 M Pb(ClO$_4$)$_2$ vs 30 mL of weekly stock solution is shown below.
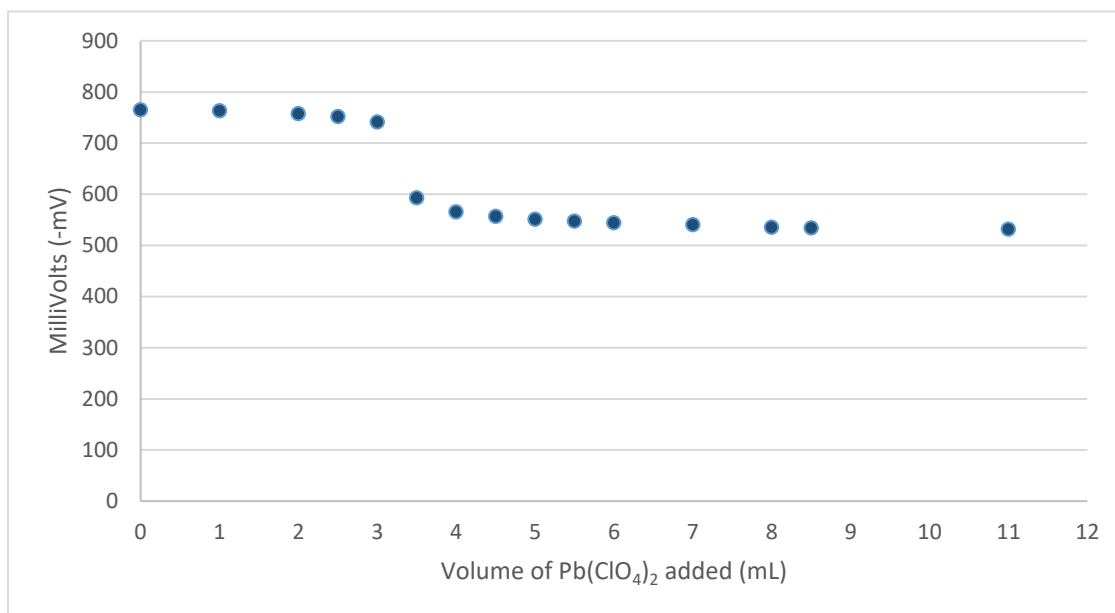
Figure 3.3. Titration of the Weekly sulfide solution with 0.1 M Pb(ClO$_4$)$_2$. The endpoint of the reaction occurs between 3 mL and 3.5 mL, thus the average value of 3.25 mL was utilized for the calculation. The concentration of the weekly stock solution was determined to be 528 ppm (1.65 x 10^{-2} M).

3.1.1. Calibration of the Sulfide Electrode

The sulfide electrode used to measure the total sulfide concentration was the Cole-Parmer ISE Silver/Sulfide electrode. The calibration was done as per the manufacturers instructions.

A standard curve was prepared by diluting the weekly stock solution with a solution of 1:1 sulfur antioxidant buffer (SAOB) and ddH$_2$O (as prepared in the section 3.2.2) to the following concentrations: 176 ppm (5.5x10^{-3} M), 17.6 ppm (5.5x10^{-4} M), 1.76 ppm (5.5x10^{-5} M) and 0.176 ppm (5.5x10^{-6} M). According to the manufacturer's instruction, the acceptable slope of a line connecting a 10x change in concentration must be ±26. An example of a curve is presented below.
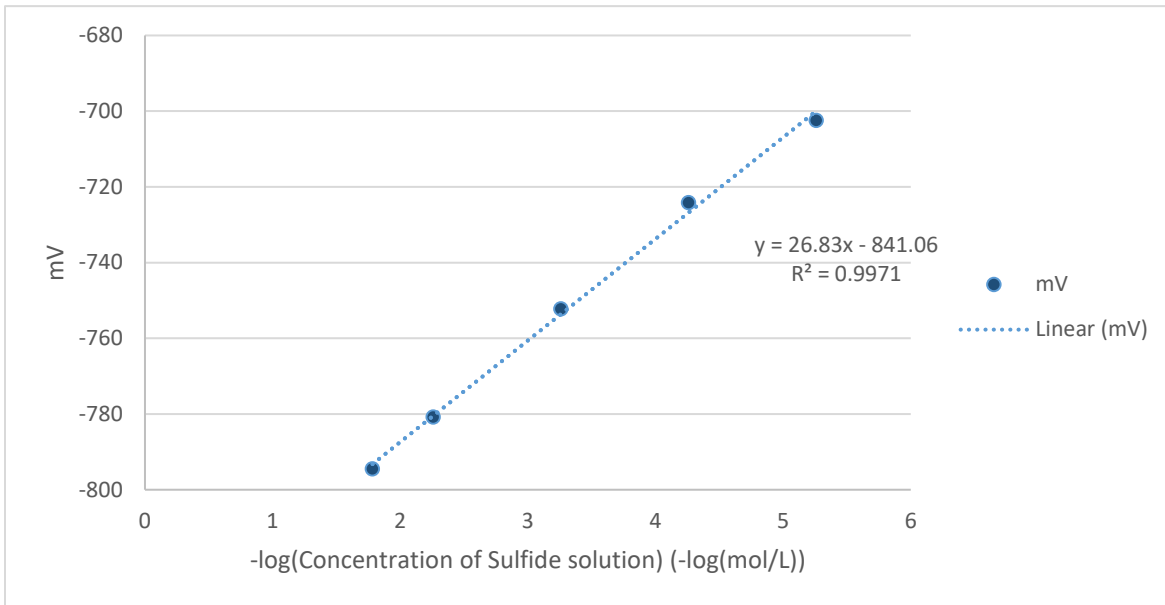
Figure 3.4. A representative calibration curve of the ISE Ag/S electrode.

3.1.2. Preparation of H₂S solutions ranging from theoretical concentrations of 3.41x10³ ppm (1x10⁻¹ M) to 3.41x10⁻⁵ ppm (1x10⁻⁹ M)

The pH dependence of the ratios of H₂S (*aq*), HS⁻ (*aq*) and S²⁻ (*aq*)

Given that H₂S is in fact a weak acid, there is some dissociation constant that can be derived from the reactions. Although it is difficult to determine the exact concentrations, the ratios of H₂S:HS⁻, HS⁻:S²⁻ and H₂S:S²⁻.The derivation is provided in the appendix in section A. The final equations are:

$$\frac{[H_2S]}{[HS^-]} = 1.12234 \ x \ 10^7 \cdot 10^{-pH} \tag{3.2}$$

$$\frac{[HS^-]}{[S^{2-}]} = 1x10^{19} \cdot 10^{-pH} \tag{3.3}$$

$$\frac{[H_2S]}{[S^{2-}]} = 1.12233446 \ x10^{26} \cdot 10^{-2pH} \tag{3.4}$$

Substituting pH = 7 to the above equations yields:

$$\frac{[H_2S]}{[HS^-]} = 1.12234 \tag{3.5}$$

45

$$\frac{[HS^-]}{[S^{2-}]} = 1x10^{12} \tag{3.6}$$

$$\frac{[H_2S]}{[S^{2-}]} = 1.12233446\ x10^{12} \tag{3.7}$$

It is important to notice that at pH = 7, [H₂S] = ~[HS⁻] and [S²⁻] is approximately 0.

Determination of H₂S *(aq)* concentration from the sulfur electrode

The sulfide electrode is only capable of providing the concentration of S²⁻ *(aq)* in a solution. As such a reverse calculation is required to determine the concentration of H₂S *(aq)* in the original sample from the S²⁻ *(aq)* concentration of the measured sample. The pH of the original solution was adjusted using H₂SO₄ until it reached pH = 7.4. The resulting solution will be referred to as the "hydrogen sulfide solution" or "H₂S solution" since most of the S²⁻ has converted to H₂S. The concentration of the total sulfide (S²⁻) in mol/L was obtained from mixing an aliquot of the H₂S solution (V_i) with SOAB (to reduce all of the H₂S and HS⁻ into S²⁻), thus making a S²⁻ solution of volume = V_T, and then measure the S²⁻ *(aq)* concentration with the sulfur electrode. The total number of moles of S²⁻, was then obtained by multiplying the concentration of S²⁻ by the volume of the S²⁻ sample used in the measurement. It is also known that the total moles of S²⁻ in the solution come from the sum of the total moles of S²⁻, Hˢ⁻ and H₂S in the original H₂S *(aq)* solution. Figure 3.5 shows the experimental setup.

$$[S^{2-}]_T\ V_T = \text{mol } S^{2-} + \text{mol } HS^- + \text{mol } H_2S \tag{3.8}$$

Dividing both sides by the volume of the aliquot of the initial solution (V_i),

$$\frac{[S^{2-}]_T V_T}{V_i} = \frac{\text{mol } S^{2-} + \text{mol } HS^- + \text{mol } H_2S}{V_i} \tag{3.9}$$

$$\frac{[S^{2-}]_T V_T}{V_i} = \frac{\text{mol } S^{2-}}{V_i} + \frac{\text{mol } HS^-}{V_i} + \frac{\text{mol } H_2S}{V_i} \tag{3.10}$$

$$\frac{[S^{2-}]_T V_T}{V_i} = [S^{2-}] + [HS^-] + [H_2S] \tag{3.11}$$

$$\frac{[S^{2-}]_T V_T}{V_i} = [S^{2-}] + [S^{2-}]1.12x10^{12} + [S^{2-}]1.122x10^{12} \tag{3.12}$$

$$\frac{[S^{2-}]_T V_T}{V_i} = [H_2S](1 + 1.122x10^{12} + 1.12x10^{12}) \tag{3.13}$$

$$\frac{[S^{2-}]_T V_T}{V_i(1+2.24x10^{12})} = [S^{2-}] \tag{3.14}$$

Subbing in V_T = 2 mL and V_i = 2 mL and that [H₂S] = [S²⁻] x 1.12 x10¹².,

$$\frac{[S^{2-}]_T \times 1.12x10^{12}}{(1+2.24x10^{12})} = [H_2S] \qquad (3.15)$$
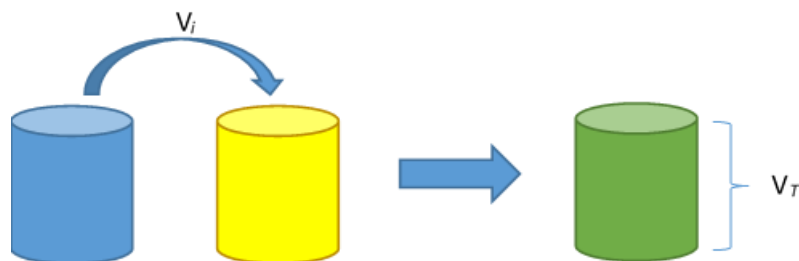
Figure 3.5. Preparation of the SAOB - S^{2-} (*aq*) solution used for the measurement of [S^{2-} (*aq*)] with the ISE Ag/S electrode. The blue solution represents the initial H$_2$S solution containing all H$_2$S, HS$^-$ and S^{2-} species. The yellow solution represents the SAOB solution. An aliquot (V$_i$) is taken from the blue H$_2$S solution and mixed with the yellow SAOB solution, giving the green solution with a final volume of V$_T$. By determining the concentration of the green solution and multiplying by V$_T$, the total moles of H$_2$S, HS$^-$ and S^{2-} transferred from V$_i$ can be determined as well as its concentration. Since the concentration of the entire blue solution is assumed to be equal, the concentration of V$_i$ is equivalent to the concentration of the blue H$_2$S solution. Subsequently, the pH and the H$_2$S, HS$^-$ and S^{2-} ratios can then be used to determine the actual concentrations of the blue H$_2$S solution. Please note: the solutions are not actually blue, yellow and green. The colors are added for clarity.

The Dilution Methodology

The concentrated sulfide solution (pH = 12.9) was titrated with H$_2$SO$_4$ until it reached a pH of 7.58. Using the sulfide electrode (calibrated as described earlier) the concentration of the H$_2$S solution was determined. Subsequently, the H$_2$S solution was diluted in blood serum as needed to make H$_2$S solutions ranging from concentrations of 3.41 x10^3 ppm (1 x10^{-1} M) to 3.41 x10^{-5} ppm (1 x10^{-9} M) of total sulfide concentration.

3.1.3. Determination of the actual concentrations of the H₂S *(aq)* solutions

The actual concentrations of the H$_2$S solutions were determined by diluting the above prepared sulfide in SAOB buffer (as described in section 3.2.2) and measuring the S^{2-} (*aq*) concentrations with the sulfide electrode and then back calculating the H$_2$S concentration as described in section 3.2.4.

3.1.4. Preparation of H$_2$S – Blood Serum Solutions

The sulfide solution was prepared as mentioned in section 3.2.2. Subsequently, 10 mL of sulfide solution was aliquoted and 200 µL of concentrated H$_2$SO$_4$ was added. The final pH of the solution as measured with a pH meter, was 7.34 while the pH of pure blood serum was determined to be 7.43. The concentration of the sulfide in the above mentioned H$_2$S solution was determined as described in section 3.2.5. Successively the SAOB dilutions were made and actual concentrations of sulfide in the blood serum were determined using the sulfur electrode as described in 3.2.3. The results are shown in Table 3.1.

The samples were subsequently then reacted with CuO as described in section 3.4.1. The experiment was also repeated 3x to determine the standard deviation of the reaction. Figure 3.6 shows the materials used.

3.1.5. Raman Spectral Accumulation Conditions

Raman Spectra were measured using a Reinshaw Invia Raman Spectrometer. A 514.5 nm laser was used as the excitation source. The scan range was from 100 to 800 cm^{-1}. Three sets of data were collected at an integration that was set at 30 seconds.

a)　　　　　　　　b)
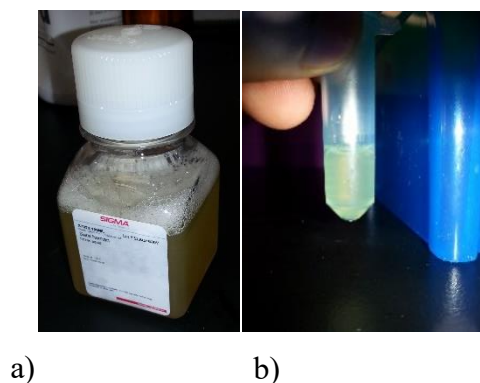
Figure 3.6. The blood serum used in the reaction is shown in Figure 3.6 a), while Figure 3.6 b) shows the SAOB solution with the aliquot of H$_2$S solution.

Table 3.1: Details of the calculation of the H_2S (aq) concentration from the S^{2-}. The S^{2-} (aq) solution was prepared and measured with the ISE Ag/S electrode as described in section 3.2.3. The calculations for the back calculation of H_2S were performed as described in section 3.2.4.

Calculated concentration of S^{2-} ppm (Concentration in mol/L)	mV Reading of ½ concentration	Actual Concentration of concentration of the total S moles in ppm (in mol/L)	Experimental [H_2S]
3.41×10^3 ppm 1×10^{-1} M	-799	2.10×10^3 ppm 6.17×10^{-2} M	1.05×10^3 ppm 3.09×10^{-2} M
3.41×10^2 ppm 1×10^{-2} M	-765	1.22×10^2 ppm 3.57×10^{-3} M	6.08×10^1 ppm 1.79×10^{-3} M
3.41×10^1 ppm 1×10^{-3} M	-719	2.57 ppm 7.54×10^{-5} M	1.28 ppm 3.77×10^{-5} M
3.41 ppm 1×10^{-4} M	-700	5.21×10^{-1} ppm 1.53×10^{-5} M	2.61×10^{-1} ppm 7.65×10^{-6} M
3.41×10^{-1} ppm 1×10^{-5} M	-690	2.26×10^{-1} ppm 6.63×10^{-6} M	1.13×10^{-1} ppm 3.32×10^{-6} M
3.41×10^{-2} ppm 1×10^{-6} M	-683	1.26×10^{-1} ppm 3.69×10^{-6} M	6.29×10^{-2} ppm 1.85×10^{-6} M
3.41×10^{-3} ppm 1×10^{-7} M	-670	4.23×10^{-2} ppm 1.24×10^{-6} M	2.11×10^{-2} ppm 6.20×10^{-7} M
3.41×10^{-4} ppm 1×10^{-8} M	-660	1.83×10^{-2} ppm 5.37×10^{-7} M	9.15×10^{-3} ppm 2.69×10^{-7} M
3.41×10^{-5} ppm 1×10^{-9} M	-610*	2.76×10^{-4} ppm * 8.10×10^{-9} M *	1.38×10^{-4} ppm * 4.05×10^{-9} M *

*The numbers in red are unsure because they are below the concentration limit of the ISE electrode.

Raman spectra were processed with Origin (2016) software. The baseline was subtracted using a "User Defined" method using a straight line with slope = 0 and y-intercept = 0 and 8 anchor points. After baseline subtraction, the peak(s) of the Raman spectra were found using the peak find method.

Peak Finding Method: Local Maximum

Smoothing Window Size: 3

Threshold: 0.05

Number of Points: 8

Interpolation method: Spline

3.2. Preparation of CuO Samples

CuO samples were prepared using two techniques: the thermal oxidation technique and the wet synthetic technique. Air and oxygen gas entered and exited the tube furnace through 0.5 cm holes in the endcaps of the heating tube. Using various cylinder gauge pressures of 1, 2 and 3 psi, "light", "medium" and "high" gas flows were obtained.

3.2.1. Thermal Oxidation Method

The thermal oxidation method was adapted from the works mentioned earlier with some modifications[112,115,117]. Firstly, copper foil (20 cm x 10 cm x 0.1 mm), copper pellets (<1 mm) and copper pellets (149 µm) were heated directly in a quartz tube (with or without fiberglass). Moreover, the Cu foil was cleaned by 100 mM HCl for 2 minutes (on both sides) followed by a wash of dH_2O. Furthermore, the samples were heated in a tube furnace, as shown in Figure 3.5. The tube furnace was preheated to the desired temperature before the samples were put inside. Also, the nominal calcination temperature range was from 200 °C to 400 °C. Lastly, a light flow of gas (air or oxygen) was added to the reaction.

CuO Preparation from Cu Foil Samples:
A thin copper foil of dimensions of 4 cm x 7 cm x 0.1 mm was obtained and cut into small pieces of 0.25 cm x 0.25 cm x 0.1 mm which were placed in a quartz boat (as shown in Figure 3.7) and then heated in the tube furnace at different temperatures between 200 °C to 400 °C for an interval of 1 hour from 1 hour to 4 hours under a light flow of air. The samples were then taken on the Raman Spectra as described in section 3.2.7.

Figure 3.7. Cu foil clippings in a quartz tube ready to enter the furnace tube. The sizes of the clippings were approximately 0.25 cm x 0.25 cm x 0.1 mm.

CuO from Ground (<1 mm) Cu Samples:

Copper pellets of the size 1 mm were placed in a quartz boat and heated in a tube furnace for the same temperatures, time durations and Raman spectral accumulation conditions as in section 3.3.7.

Figure 3.8. Copper pellets (<1 mm) in a quartz tube before heating. The discoloration is due to the lighting and the camera. The copper pellets (< 1mm) are the bright orange color as depicted in the far left of the image.

CuO from 149 μm Cu Samples:

A small portion of glass wool was obtained and spread out on a quartz boat. 100 mesh ground copper (size of 149 μm) were lightly sprinkled on the glass wool. Then this was layered with another layer of glass wool and then had more copper mesh was sprinkled on the glass wool. Then these layers were heated in the tube furnace at 400 °C between 1 to 3 hours. The Raman spectra were obtained as described in section 3.2.7.

a)   b)   c)

Figure 3.9. Cu pellets (149 μm) and the CuO from the pellets after heating at 400 °C in air. Figure 3.9a) shows the Cu pellets (149 μm) as obtained from the manufacturer. Figure 3.9b) shows the layered Cu in the quartz tube ready for heating. Lastly, Figure 3.9c) shows the CuO that resulted after heated at 400 °C in air.

3.2.2. CuO Preparation using the Wet Synthetic Method

The wet synthetic technique, also known as the sol-gel technique, was used for the preparation of nano-CuO structures. The wet synthetic technique was adapted from previous protocols with some differences[125,128]. Firstly, two different precursors were explored: $Cu(NO_3)_2$ with NH_4OH and $Cu(oAs)_2$ with NaOH. Glycerol was added to $Cu(oAs)_2$ substituting thioglycerol. Lastly, the nomial calcination temperature range was from 200 °C to 450 °C.

CuO Preparation from $Cu(NO_3)_2$ Samples:

CuO was prepared as described earlier, with a slight modifications: the calcination temperature range was from 200 °C to 450 °C[128]. Briefly, 1.199 g of $Cu(NO_3)_2 \cdot H_2O$ was dissolved in 6.393 mL of dH_2O in a round-bottom flask and then stirred for 20 minutes. After stirring, the precipitate, $Cu(OH)_2$, was isolated using suction filtration and subsequently heated in a tube furnace under airflow, as described in section 3.3.1 and the Raman spectra was collected as described in section 3.2.7.

a)   b)   c)   d)
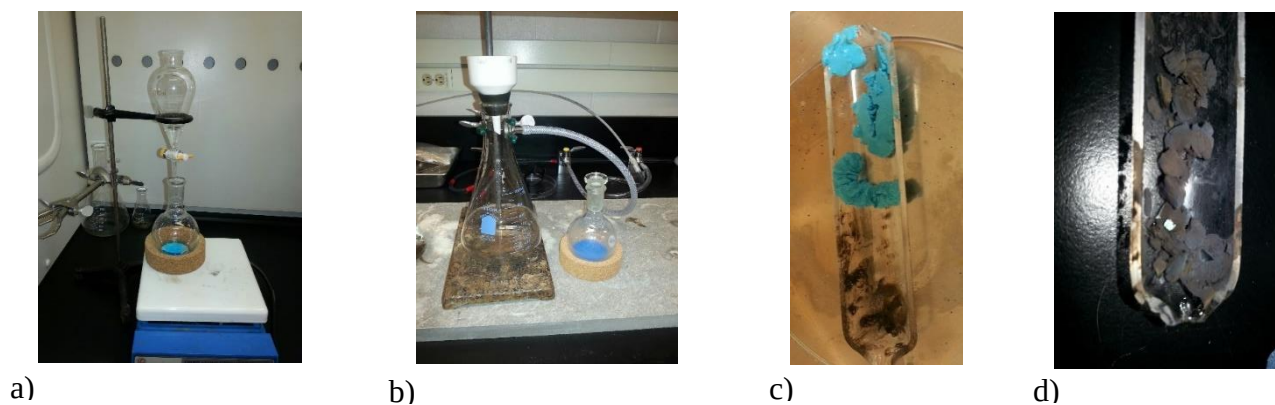
Figure 3.10. The setup for the $Cu(NO_3)_2$ sol-gel preparation of CuO. The reaction was conducted in stages. Figure 3.10 a) shows the first stage where $Cu(NO_3)_2$ and NH_3OH are mixed under constant stirring. Figure 3.10 b) shows the filtration of the $Cu(OH)_2$, which is then put onto a quartz tube, Figure 3.10 c), and heated at 400 °C for 4 hours. The final CuO product is shown in Figure 3.10 d).

CuO production using the $Cu(oAs)_2$ Method:

The CuO was prepared as described earlier with two minor changes[125]. Firstly, glycerol was added to

replace thioglycerol and secondly, the calcination temperatures were between 200 °C to 450 °C to determine the optimal synthesis temperature. Briefly, 1.901 g of copper (II) acetate (Cu(oAs)$_2$) was dissolved in 19 mL of dH$_2$O and then stirred. Afterwards, a drop of glycerol (~100 µL) was added to the Cu(oAs)2 and it was stirred for another 10 minutes. Subsequently, 3.809 mL 5M NaOH (1.90×10^{-2} mol) was added dropwise to the Cu(oAs)$_2$ solution along with 120 mL of dH$_2$O. The blue solution was further stirred for another half hour after which it was suction filtered for 5 hours. The experimental setup was nearly identical to that of CuO from Cu(NO$_3$)$_2$ with only slight modifications as shown in Fig 3.10.

3.2.3. CuO preparation in Oxygen

CuO Preparation of Cu foil in Oxygen:
Small clippings of Cu foil (0.25 cm x 0.25 cm x 0.1 mm) were prepared as mentioned in section 3.3.1. These were then placed onto the quartz boat and placed onto the tube furnace at 300 °C and 400 °C, for 1 to 3 hours under low, medium and high oxygen flow. At the designated times, small samples were removed from the tube furnace.

CuO Prepared from Cu (<1 mm) Pellets

The Cu pellets (<1 mm) were prepared and heated as described in section 3.3.1.

CuO Preparation from Cu 149 µm Pellets

CuO 149 µm pellets were prepared by layering Cu on glass wool (3 layers) on a quartz tube and then heated in the tube furnace with the same oxygen flow, times and heat as described in section 3.3.3.

3.3. Preparation of CuS Samples

CuS was prepared from the reaction of CuO and H$_2$S solutions as described in section 3.4.

3.3.1. 4-hour CuS samples

CuO samples prepared from the Cu mesh (149 µm) was prepared as described in section 3.3.1. Small amounts of these samples, ~130 grains (a volume of approximately 0.3 cm x 0.3 cm x 0.02 cm), were placed into 9 eppendorf tubes, one for each concentration sample. Then 500 µL of the H_2S solution + H_2SO_4 + Blood serum (as prepared in section 3.2.6) was added to the tube. To ensure all the CuO samples were exposed, the tube lid was closed and the tube was inverted multiple times. After the required time had elapsed, the H_2S solution was pipetted out and the tube was rinsed with dH_2O twice. All experiments were repeated three times. The Raman spectra was obtained as described in section 3.2.7.

3.3.2. Determination of the Rate of Accumulation of H_2S of 3.41×10^{-2} ppm (1×10^{-6} M) when exposed from 2 hours to 12 hours

The rate of accumulation was determined by taking the time derivative of the relation between the band intensity and time. The procedure was the same as in section 3.5.1 with the following differences. Firstly, CuO was placed into 5 eppendorf tubes labelled 2 hours, 6 hours, 12 hours, 16 hours and 24 hours. Moreover, 500 µL of only the 3.41×10^{-2} ppm (1×10^{-6} M) of H_2S + H_2SO_4 + Blood serum solution (as prepared in section 3.2.6) was added to each of the tubes. Lastly, the time of exposure were different, varying from 2 hours to 24 hours. However, each experiment was conducted 3 times to determine the standard deviation of the reaction. The Raman spectra was obtained as described in section 3.2.7.

3.4. Specificity Tests

To test for the specificity of CuO, solutions of common sulfur compounds were prepared at clinically relevance concentrations. CuO pellets (<1 mm), as prepared in section 3.3.1., were used for the experiment and the raman spectra was obtained as described in section 3.2.7.

3.4.1. CuO Interaction with L-Cysteine (Cys) Solutions

Cys·HCl
2.31 mg of L-Cys·HCl was dissolved 100 mL of freshly obtained dH_2O (Milli-Q water). CuO pellets (<1mm) were exposed to this solution for 5 mins before being washed with dH_2O.

Cys·HCl + NaBH₄ in blood plasma

To ensure that the Cys was not dimerizing a weak acid, NaBH₄, was added. Initially 6 mg of L-Cys·HCl was added to 100 mL of fresh dH_2O to make a 6 mg/ 100 mL solution. Furthermore, 1 mL of the 6 mg/100 mL solution was added to 1 mL of blood plasma, with a final solution of 3 mg/100 mL in 50% blood plasma. Preparation of the NaBH₄ solution began by dissolving 0.946 g of NaBH₄ in 100 mL of dH_2O to make a 0.25 M solution. Then 76 µL of the 0.25 M solution was added to 3 mg/ 100 mL solution of L-Cys in blood plasma. This solution was then reacted with CuO for 5 minutes as described in section 3.4.

3.4.2. CuO Interaction with Methionine in blood plasma

Similar to section 3.5.1., 4.0 mg of L-Methionine was dissolved in 100 mL of dH_2O and then subsequently 1 mL of the 4 mg/100 mL solution was mixed with 1 mL of blood plasma, thus making a 2 mg/100 mL solution of L-Methionine in 50% blood plasma. The solution was then exposed to CuO for 5 minutes as described in section 3.5.1.

3.4.3. CuO Interaction with SO_3^{2-} in blood plasma

Similar to section 3.5.1, 300 mg of Na_2SO_3 was dissolved in 100 mL to make a 4.72 mg/100 mL solution of SO_3^{2-} (*aq*). Subsequently, 1 mL of the 4.72 mg/100 mL solution was mixed with 99 mL of dH_2O to make a 3.0 mg/100 mL solution of SO_3^{2-} (*aq*).

3.4.4. CuO Interaction with SO_4^{2-} in blood plasma

The preparation of 3.0 mg/mL solution of SO_4^{2-} (*aq*) was prepared just as in section 3.5.3. The only variance was the use of Na_2SO_4 (*aq*) instead of Na_2SO_3 (*aq*).

3.5. Coupon Production

Small rectangles of plastic (1 cm x 2 cm) were cut out and washed with acetone. A drop of crazy glue was added to the plastic and CuO (as prepared in section 3.4.1.3) was lightly sprinkled onto the glue.
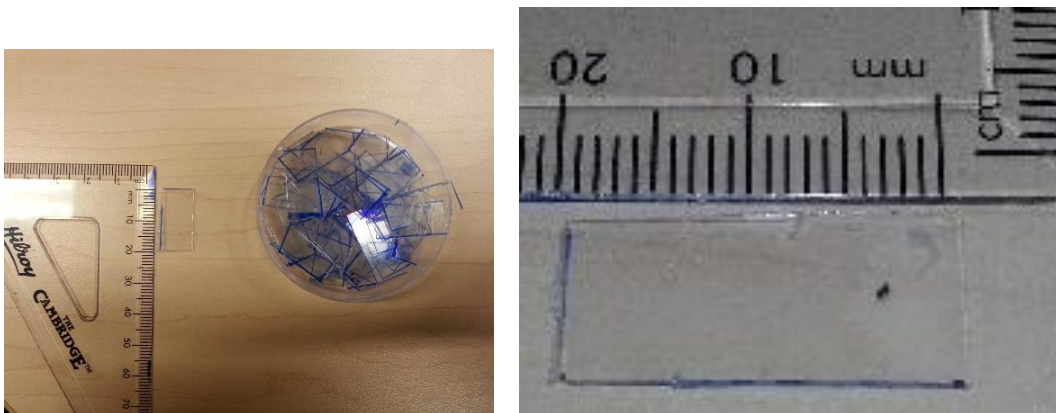
Figure 3.11. The mock 1 CuO coupons.

CHAPTER 4: RESULTS

In this section the results from the four experiments are presented. The first set of experiments are referred to as the "Results of the CuO/CuS Preparation Techniques" determine the optimal method for the synthesis of CuO which will be used for the subsequent experiments. The experiment utilizes the Raman spectra of the samples to judge the quality of the CuO and CuS samples. The second set of experiments are referred to as the "4-hour experiment". The purpose of this experiment is to determine the correlation between the peak intensity of the $Cu - S - S - Cu$ (475 cm^{-1}) peak and the concentration of H_2S in the samples. The third experiment is called "the Determination of the Rate of Accumulation" and its purpose is to determine the rate at which the band intensity changes with time for a 1.22×10^{-6} ppm concentration, the most probable concentration of H_2S in the body. The last experiment is referred to the "Specificity Tests". The purpose of this ensure that the peak at 475 cm^{-1} is specific to the H_2S and not other sulfur compounds.

4.1. CuO/CuS Preparation Techniques

CuO was prepared by several methods. The objective was to determine the optimal CuO synthesis method for the production of CuS. CuO was prepared from copper foil, copper pellets (<1 mm), copper pellets (149 μm) all in air and oxygen gas as well as $Cu(NO_3)_2$ and $Cu(oAs)_2$. The CuO samples were then reacted with H_2S solutions. The quality was analyzed by using Raman spectroscopy. The criteria for selection were:

1. High quality CuO (having only 3 peaks located at the A_g and 2 B_g peaks of CuO)
2. Reproducibility
3. Good CuS spectra

4.1.1. Results of Thermal oxidation with Airflow

CuO preparation from Cu Foil

Cu foil clippings were prepared as described in section 3.3.1. Uniformity and reproducibility were determined by Raman spectral accumulations as described in section 3.2.7. The most uniform and reproducible CuO was prepared from Cu foil heated at 400 °C at 3 hours. Raman spectra were obtained of the optimal CuO from Cu foil along with the Cu foil background spectra in Fig 4.1. There are 4 peaks observed in the mentioned CuO spectra: 160 cm^{-1}, 310 cm^{-1}, 340 cm^{-1} and 620 cm^{-1}. Subsequently, scanning electron microscopy (SEM) images were obtained in order to determine the morphology of the CuO. SEM images were taken and the results are shown in Fig 4.2. It can be seen from Fig 4.2 that the CuO morphology of the foil is flowershaped. Figure 4.3 furthermore the size of the nanoparticles are shown to be approximately 1.4 nm by atomic fluorescent microscopy.
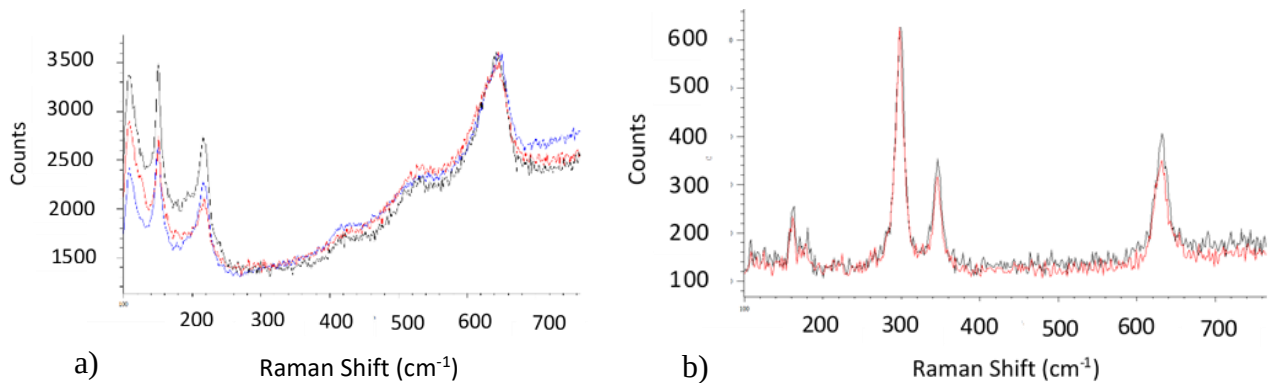
Figure 4.1. Copper background spectra and the CuO spectra obtained from heating Cu foil (0.25 cm x 0.25 cm x 0.1 mm) in a tube furnace for 3 hours at 400 °C. Fig 4.1a) shows 3 overlapping background spectra of copper foil. In contrast Fig 4.1b) shows the CuO spectra after the thermal oxidation. It contains 4 peaks at 160 cm^{-1}, 310 cm^{-1}, 340 cm^{-1} and 620 cm^{-1}. A high degree of uniformity can be observed from the spectra. It is important to note that there are no peaks between the 340 cm^{-1} and 620 cm^{-1} peaks.
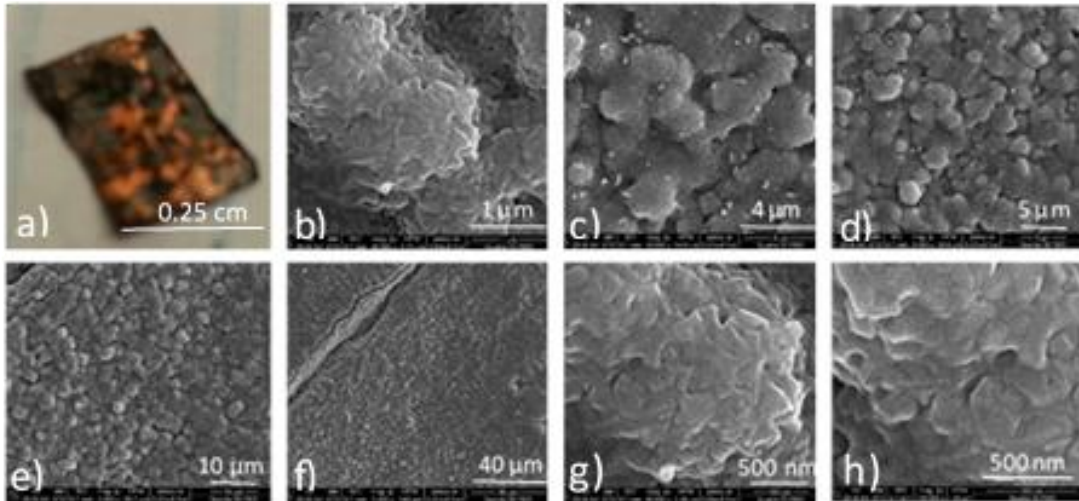
Figure 4.2. Results of the SEM imaging on CuO from Cu foil heated at 400 °C for 3 hours. Figure 4.2a) shows the CuO foil while b-h) show the various SEM images at different magnifications.
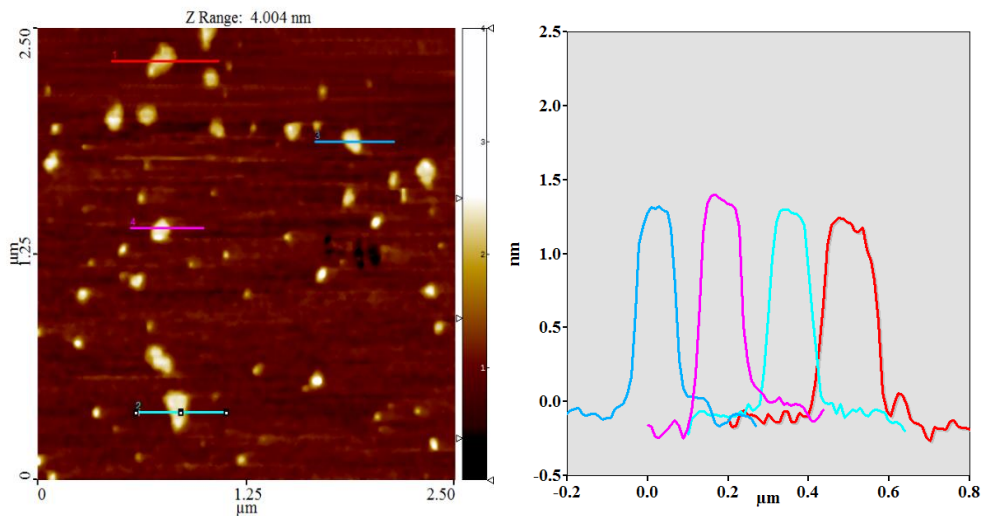
Figure 4.3. Atomic Fluorescent Microscopy of the CuO flakes. The average size of the CuO flakes is approximately 1.4 nm.

CuO from Cu pellets (<1 mm)

Copper pellets (< 1 mm) were obtained and heated as described in section 3.3.1. The uniformity and reproducibility were determined by Raman spectral accumulations as described in section 3.2.7. The

optimal CuO formation from the Cu pellets < 1 mm also occurred when heated at 400 °C for 3 hours. The Raman spectra of the Cu pellets (<1 mm) (background spectra) and the optimal CuO are shown in Fig 4.4. Subsequently, morphological information was obtained through SEM images as shown in Fig 4.5. The results of the SEM clearly show the CuO nanorods.

a)   b)
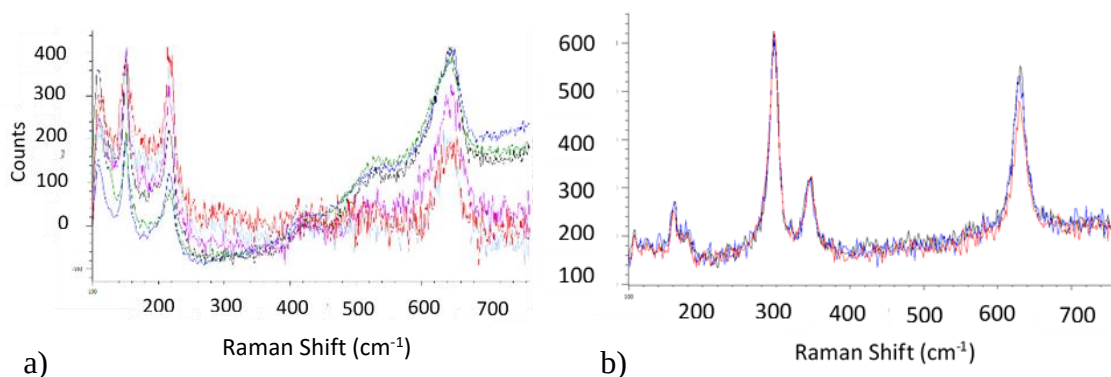
Figure 4.4. Raman spectra of the copper pellet (< 1mm) background spectra and the optimal CuO prepared from it. Fig 4.3a) shows the overlapping of 7 background spectra. Figure 4.4b) shows three overlapping CuO spectra (heated at 400 °C for 3 hours). There are 4 notable peaks on the spectra located at 180 cm^{-1}, 300 cm^{-1}, 340 cm^{-1} and 640 cm^{-1}. It is also noteworthy that there are no peaks from 340 cm^{-1} until 640 cm^{-1} in CuO.
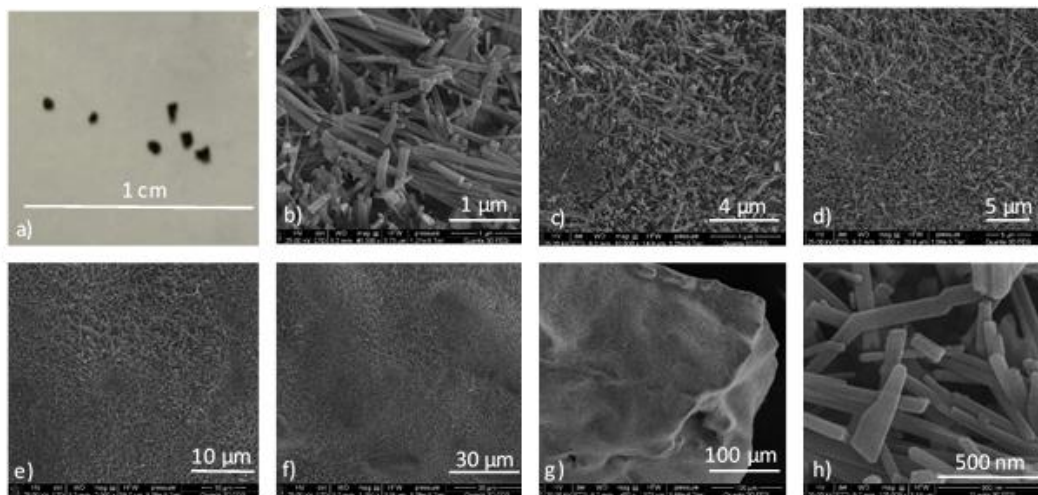
Figure 4.5. Results of the SEM imaging on CuO from Cu pellets (< 1mm) heated at 400 °C for 3 hours. Figure a) shows the CuO pellet (<1 mm) while b-h) show the various SEM images at different magnifications. The morphology of the CuO at the nanoscale are nanorods.

60

CuO from Cu 149 µm pellets

CuO was prepared from Cu 149 µm pellets as described in section 3.3.1. The reproducibility and purity of CuO was determined by Raman spectral accumulations as described in section 3.2.1. The results have shown that after 2 hours of heating at 400 °C, nearly perfect, uniform and highly reproducible CuO Raman spectra were obtained. The Raman spectra are shown below in Figure 4.6.
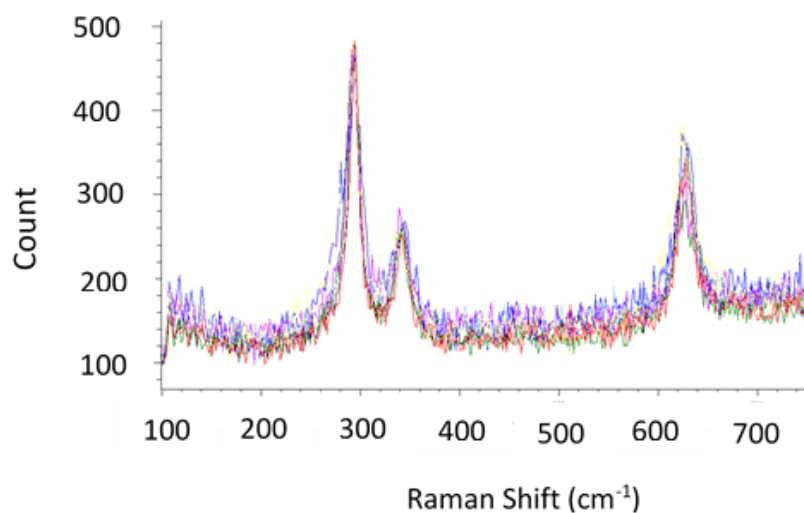
Figure 4.6. Seven overlapping spectra of CuO prepared from Cu 149 um pellets heated at 400 °C for 2 hours. There are 3 peaks in the spectra located at 300 cm^{-1}, 320 cm^{-1} and 610 cm^{-1}. Moreover, there are no peaks in between the 320 cm^{-1} and 610 cm^{-1} spectra.

The Raman spectra of CuO prepared from Cu 149 um pellets is among the highest quality of CuO and among the most reproducible. There are three peaks in the CuO spectra corresponding to the 1A$_g$, 1B$_g$ and 2B$_g$ spectral peaks of CuO. Their peak locations are at 300 cm^{-1}, 320 cm^{-1}, and 620 cm^{-1} respectively.

CuO from Cu(oAs)$_2$

CuO from Cu(oAs)$_2$ was prepared as described in section 3.3.2. Briefly, a drop of glycerol was added to a 0.5 molar solution of Cu(oAs)$_2$. Subsequently, a 5 M NaOH solution was added dropwise to the Cu(oAs)$_2$ solution and immediately after 120 mL of dH$_2$O was added. The mixture went from clear and colorless to

61

bright blue and the resulting solution was stirred for an hour. Afterwards, the $Cu(OH)_2$ was separated by suction filtration, placed in a quartz boat and then heated in a tube furnace at 380 °C and 400 °C for 1 to 4 hours. The resulting CuO was then examined under Raman spectroscopy for quality and reproducibility. According to the results, the optimal CuO spectra was formed by heating at 400 °C for 2 hours, however, the three and four hour samples were just as successful. Fig 4.7 shows the Raman spectra of CuO from $Cu(oAs)_2$ heated at 400 °C for 2 hours, 3 hours and 4 hours. It can be seen from Fig 4.7 that CuO prepared through this method has high purity and reproducibility.
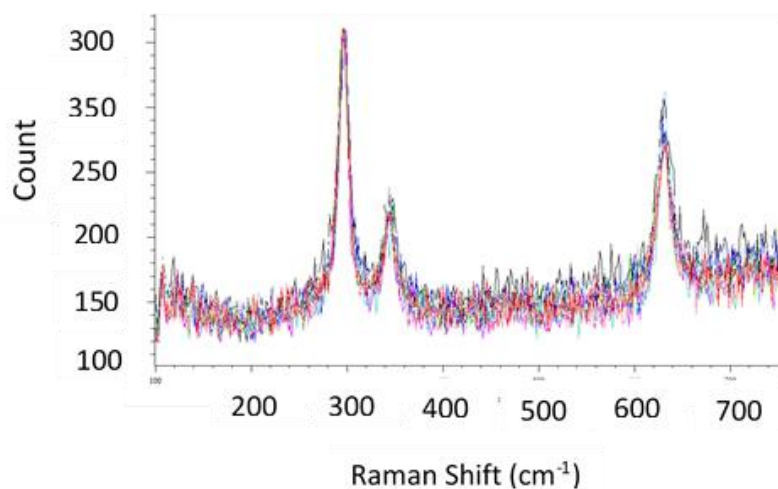
Figure 4.7. Raman spectra of CuO as prepared from $Cu(oAs)_2$. The figure shows samples heated at 400 °C for 2 - 4 hours, with a total of 9 spectra. There are three notable peaks at 300 cm^{-1}, 320 cm^{-1} and 620 cm^{-1}. Also, there are no peaks in between the 320 cm^{-1} and 620 cm^{-1} peak.

CuO from $Cu(NO_3)_2$

CuO prepared from $Cu(NO_3)_2$ was prepared in the manner described in section 3.3.2. Unfortunately, there was no optimal CuO spectra obtained - the purity was low, yet the reproducibility was quite high. Fig 4.8 shows the Raman spectra of CuO as prepared from a 1 M $Cu(NO_3)_2$ and 1.5 M NH_3OH at 400 °C for 2 – 4 hours.
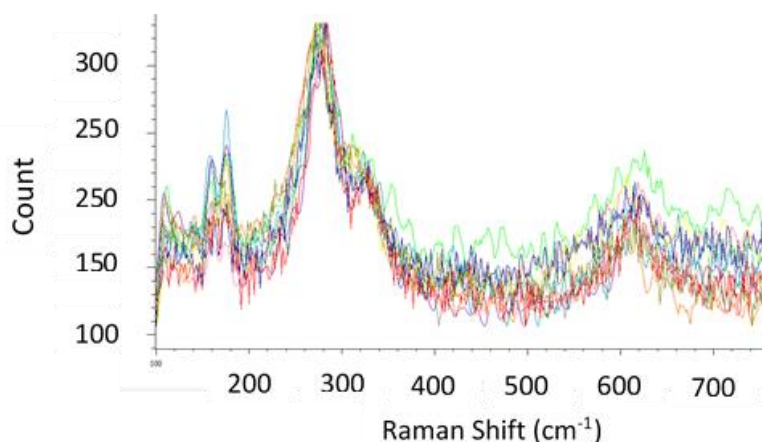
Figure 4.8. Raman spectra of CuO as prepared from $Cu(NO_3)_2$ and NH_3OH heated at 400 °C for 2 – 4 hours. Raman spectral accumulations were taken over the range of 100 cm^{-1} to 700 cm^{-1} for 30 seconds an accumulation. The spectra are highly reproducible but lack clear and concise peaks. there are 4 visible peaks in the spectra: 190 cm^{-1}, 290 cm^{-1}, 320 cm^{-1} and 610 cm^{-1}. It is also noteworthy that although there are no peaks between the 320 cm^{-1} and 610 cm^{-1} peak, there is a high signal – to – noise ratio in between the peaks.

As can be seen from the Figure 4.8, that the CuO samples are reproducible, albeit not of high quality. Nevertheless, there are 4 visible peaks in the spectra: 190 cm^{-1}, 290 cm^{-1}, 320 cm^{-1} and 610 cm^{-1}. It is also noteworthy that although there are no peaks between the 320 cm-1 and 610 cm-1 peak, there is a high signal – to – noise ratio in between the peaks making the possibility of measuring a 474 cm^{-1} (Cu – S – S – Cu) peak difficult.

4.1.2. CuO preparation in Oxygen gas

The samples were prepared exactly as described in 3.4.3. Different levels of oxygen flow were tested; the flows were high, medium and low oxygen flows and each were defined in comparison to each other (i.e. the medium flow is greater than the low flow, yet less than the high flow rate). Then the copper substrates were heated at temperatures between 350 – 450 °C.

Preparation of CuO from Cu foil

Cu foil was prepared as described in 3.4.3.1. The optimal Raman spectra for CuO from Cu foil was seen

to be at 400 °C under medium oxygen flow for 2 hours (see Figure 4.9).
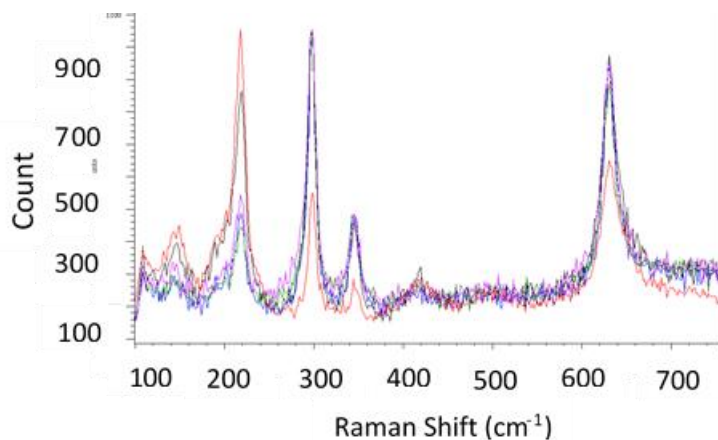
Fig 4.9. Raman spectra CuO as prepared by heating Cu foil clippings of size ~0.25 cm x 0.25 cm x 0.1 mm in a tube furnace at 400 °C for 3 hours under medium oxygen flow. There are a total of 7 peaks in the spectra located at 120 cm^{-1}, 210 cm^{-1}, 300 cm^{-1}, 320 cm^{-1}, 410 cm^{-1}, 500 cm^{-1}, and 620 cm^{-1}.

The Raman spectra of CuO from Cu foil under oxygen gas is not uniform and contains many of the Cu background peaks (as seen in Figure 4.9). The spectra are non-reproducible, with every spectrum having a slight difference in peak ratios or an extra peak.

Preparation of CuO from Cu pellets (<1 mm) in oxygen gas

CuO from Cu pellets (<1 mm) was prepared under oxygen gas as described in section 3.3.1. The Raman spectra is shown in Fig 4.10. The Raman spectra of the CuO are non-reproducible and non-uniform. There are 7 visible peaks in the spectra located at 120 cm^{-1}, 210 cm^{-1}, 300 cm^{-1}, 320 cm^{-1}, 410 cm^{-1}, 500 cm^{-1} and 620 cm^{-1}. Majority of the spectra correspond the background spectra of Cu pellets (see Figure 4.10).

Figure 4.10 shows the spectra of CuO prepared from Cu pellets (< 1mm) as prepared by heating the pellets for 3 hours at 400 °C under medium oxygen flow. The spectra are of mediocre quality, having the 3 peaks of CuO at 300 cm^{-1}, 320 cm^{-1} and 610 cm^{-1} and the impurity peak at 210 cm^{-1}. The spectra are also reproducible which implies an ease in production. Moreover, there are no peaks in between the 320 cm^{-1} and 610 cm$_{-1}$ peak which does allow for detection of the 474 cm^{-1} peak.
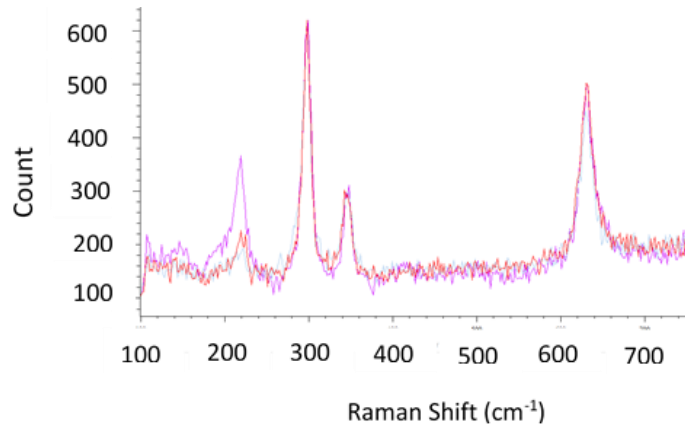
Figure 4.10. CuO Raman spectra as prepared from heating Cu pellets (<1 mm) for 3 hours at 400 °C under medium oxygen flow. The spectra are moderately reproducible and of fair quality, giving 4 peaks at 210 cm^{-1}, 300 cm^{-1}, 320 cm^{-1} and 610 cm^{-1}. Moreover, there is no peak between 320 cm^{-1} and 620 cm^{-1}.

Preparation of CuO from Cu 149 μm pellets in oxygen gas

CuO was also produced from the thermal oxidation of Cu 149 μm pellets in a tube furnace at 380 °C 400 °C for 1 to 3 hours as described in section 3.3.1. The optimal CuO preparation technique for Cu 149 μm pellets was to heated at 400 °C for 3 hours. The Raman spectra are shown in Figure 4.11. The spectra are moderately reproducible yet the reaction is not uniform.
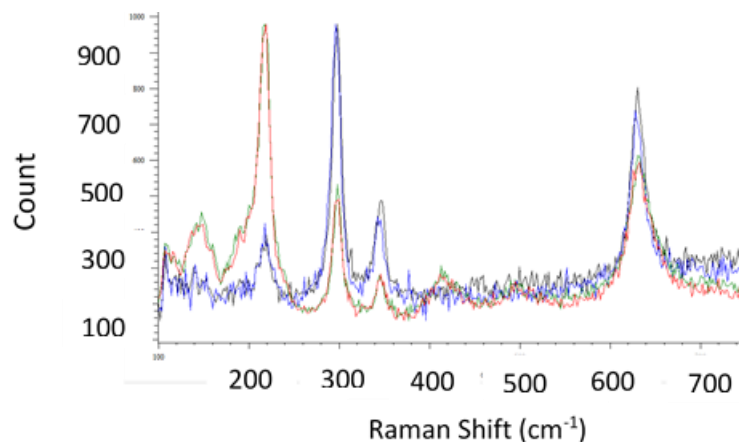
Figure 4.11. Raman spectra of CuO prepared from Cu 149 μm pellets being heated at 400 °C for 3 hours under medium oxygen flow. The spectra show a non-uniform oxidation of the Cu pellets giving rise to the two types of spectra.

The Raman spectra of the CuO from the thermal oxidation of Cu 149 μm of 400 °C for 3 hours are shown in Figure 4.11. The figure shows two different sets of spectra. The first set of spectra are from the Cu pellet background spectra. It contains 7 sets of peaks at 140 cm^{-1}, 210 cm^{-1}, 300 cm^{-1}, 340 cm^{-1}, 410 cm^{-1}, 500 cm^{-1} and at 640 cm^{-1}. The second set of spectra has 4 peaks at 210 cm^{-1}, 300 cm^{-1}, 320 cm^{-1} and 620 cm^{-1}. The presence of two sets of spectra suggests that the oxidation was non-uniform and the presence of the 210 cm^{-1} peak in the second set suggests that there was imperfect CuO synthesis. Furthermore, since both sets have very little deviance from the spectral peak ratios (of the sets), it implies that the oxidation is reproducible.

4.1.3. CuS Screening

All of the Cu from Cu foil, pellet (<1 mm), pellet 149 um (1 hour and 2 hour), from $Cu(NO_3)_2$ and CuO from $Cu(oAs)_2$ samples were reacted with H_2S water as prepared in section 3.3.1 and their corresponding Raman spectra obtained. The purpose of this screening was to separate the CuO preparation technique(s) that produce the highest quality CuO (in terms of number of peaks and reproducibility) and that is most sensitive to [H_2S]. The three criteria for screening are: 1) high quality of CuO (containing only 3 peaks at the locations 300 cm^{-1}, 320 cm^{-1} and 620 cm^{-1}), 2) the height of the 474 cm^{-1} peak and 3) the reproducibility of both the CuO spectra and the CuS spectra. The following data shows the most successful data of the entire screening selection of CuO.

It should be noted that CuO spectra has three peaks, the first is the 300 cm^{-1}, 320 cm^{-1} and 620 cm^{-1}. They correspond the to $1A_g$, 1 B_g and 2 B_g peaks as predicted by Group Theory. Full details were provided in section 2.2.2.

The reactions were performed as described in section 3.1. After the reaction with H_2S water, the sample substrate was rinsed with dH_2O and subsequently dried for 1 hour after which the Raman spectra was obtained as described in section 3.2.7. None of the oxygen samples were selected for CuS screening since the CuO spectra were so weak.

CuS from Cu Foil:

CuS from copper foil was prepared as described in sections 3.3.1. and 3.3.4. Interestingly, CuS was detected in the Cu foil substrates for the Cu foil heated at 400 °C at 2 hours. A comparison of the CuO spectra and CuS spectra of the Cu Foil heated at 400 °C for 2 hours are shown below in Fig 4.11. This sample is unique in that although the CuO spectra is very weak, the CuS spectra is the best recorded spectra in this thesis. In comparison to the spectra of Cu foil 2 hours, the Cu foil heated for 3 hours (the best CuO spectra from Cu foil set), has a very weak CuS spectra. The CuS spectra for Cu foil heated at 400 °C for 3 hours is shown below in Fig 4.13.
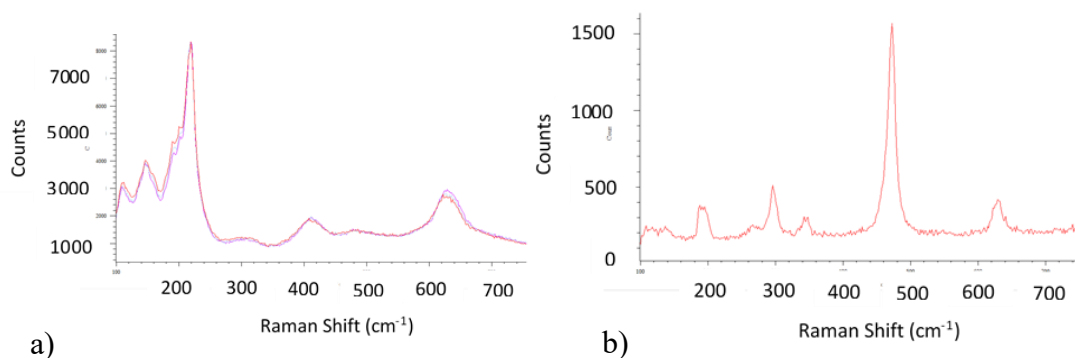
Figure 4.12. Comparing the Raman spectra of Cu foil heated at 400 °C for 2 hours and the same Cu foil reacted with H_2S water. Fig 4.12 a) shows the CuO spectra of the sample while Figure 4.12 b) shows the CuS spectra of the sample. Figure 4.12a) is the background spectra of the Cu foil. The spectra of CuS in Figure 4.12 b) has 5 peaks. The first peak is at 200 cm^{-1}, 300 cm^{-1}, 320 cm^{-1}, 475 cm^{-1} and 620 cm^{-1}.

The Raman spectra seen in Figure 4.12 b) has 5 spectral peaks at 200 cm^{-1}, 300 cm^{-1}, 320 cm^{-1}, 475 cm^{-1} and 620 cm^{-1}. The ratio of the 475 cm^{-1} spectral peak to the 300 cm^{-1} spectral peak is approximately 3. The reproducibility of this sample was not tested due to the extreme weakness of the CuO spectra as seen in Figure 4.12 a).

a)

b)
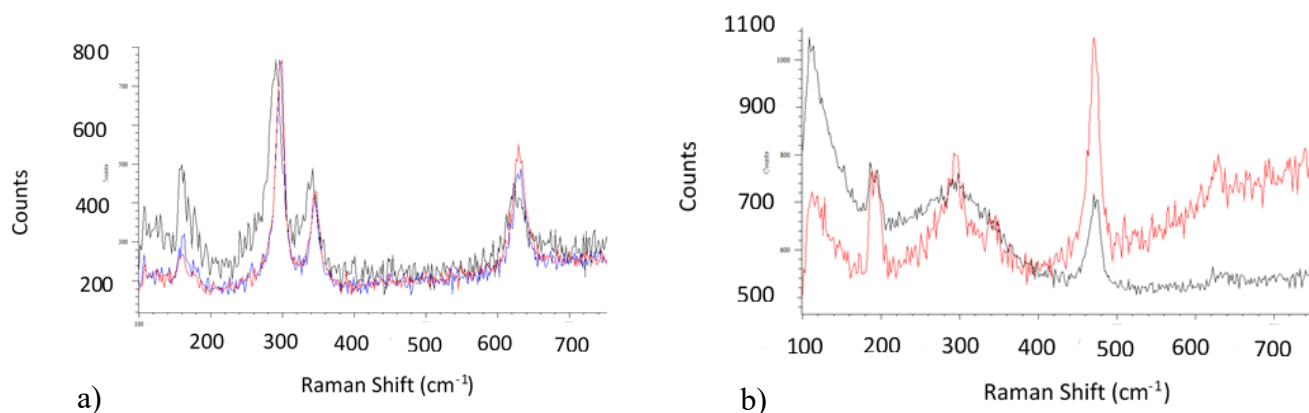
Figure 4.13. Comparing the Raman spectra of Cu foil heated at 400 °C for 3 hours and the same Cu foil reacted with H_2S water. Figure 12 a) shows the CuO spectra containing 4 peaks at 180 cm^{-1}. 300 cm^{-1}, 320 cm^{-1} and 620 cm^{-1}. The spectra of Figure 12 a) are moderately reproducible. Similarly, there are 5 peaks in Figure 12b) located at 200 cm^{-1}, 300 cm^{-1}, 320 cm^{-1}, 475 cm^{-1} and 620 cm^{-1}.

Figure 4.13 a) and b) show the Raman spectra of CuO and CuS of Cu foil heated at 400 °C for 3 hours. The Raman spectra is of low quality, owing to the 180 cm^{-1} peak, and moderately reproducible, owing to the difference between the spectra. Similarly, the CuS spectra of Fig 4.13 b) was quite weak. There are 5 peaks in the spectra located at 200 cm^{-1}, 300 cm^{-1}, 320 cm^{-1}, 475 cm^{-1} and 620 cm^{-1}. The spectra are also non-reproducible as they have a high degree in variance.

It is an interesting anomaly that although the spectra of CuO heated at 400 °C for 2 hours is weak, the CuS spectra is strong.

CuS from CuO pellets (< 1 mm)

CuO pellets (<1 mm) were prepared from Cu pellets (<1 mm) as described in section 3.3.1. Subsequently, the CuO pellets (<1 mm) were exposed to H_2S water as described in section 3.4. Small quantities of the CuO pellets (<1mm) were put in eppendorf tubes and exposed to H_2S water.

CuO pellets (< 1mm) are much more predictable as compared to the CuO from foil. The optimal CuS spectra was obtained from CuO heated at 400 °C for 3 hours as shown in Figure 4.14. The figure shows

the comparison between the Raman spectra of the CuO and CuS of the sample.

a)　　　　　　　　　　　　　　　　　　　b)
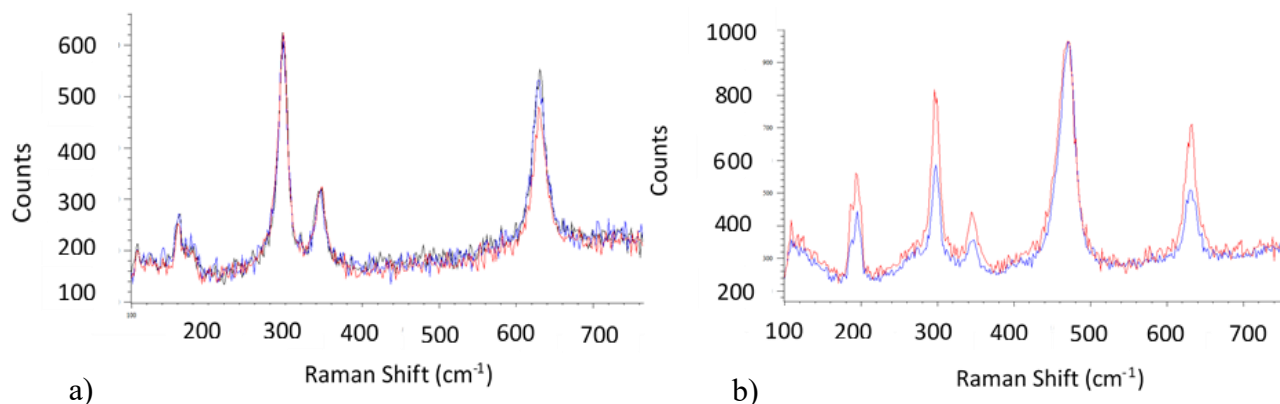
Figure 4.14. Comparison of the CuO and CuS spectra of Cu pellets (<1mm) heated at 400 °C for 3 hours.

The spectra of Figure 4.14 have certain important characteristics. Firstly, Figure 4.14 a) shows 4 spectral peaks and significant reproducibility. The spectral peaks include the 3 spectral peaks at 300 cm^{-1}, 320 cm^{-1} and 620 cm^{-1} of CuO and the spectral peak at 180 cm^{-1}. Similarly, the Figure 4.14 b) shows the 5 peaks of the CuS sample. The peaks are located at 200 cm^{-1}, 300 cm^{-1}, 320 cm^{-1}, 475 cm^{-1} and 620 cm^{-1}. The peaks show reasonable reproducibility, yet the quality is debatable. The 200 cm^{-1} peak can be interpreted in two ways. The first is that it is the same signal as observed in Figure 4.14 a), a peak of the low quality CuO. The second possibility is that it is the Cu – S peak, which is expected to be at the 200 cm^{-1} length. Unfortunately, because there are two possibilities, it cannot be used for the standard curve.

CuS from CuO pellets (149 μm)

CuO pellets (149 μm) heated at 400 °C for 2 hours in air were reacted with H$_2$S solutions as prepared from Na$_2$S solutions as described in section 3.3.1. and section 3.4. and diluted until the concentration was in the range of 7.53 x10^{-3} ppm (1x 10^{-1} M). The CuO was exposed for 5 mins and then immediately washed with dH$_2$O and dried for 1 hour. A comparison of the Raman spectra of CuO and CuS of the sample is shown below in Figure 4.15.
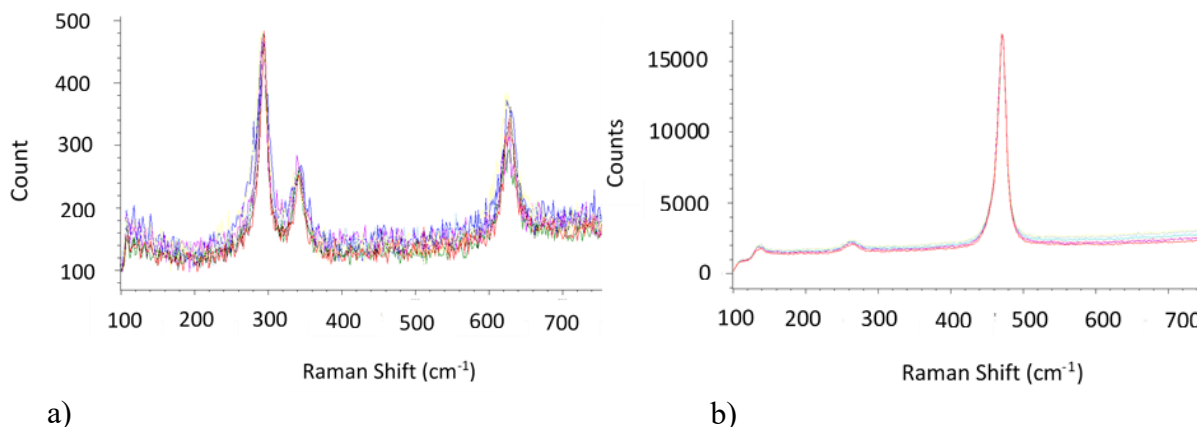
Figure 4.15. The comparison between the Raman spectra of the CuO and CuS as prepared from Cu pellets 149 μm heated at 400 °C for 2 hours. Figure 4.15 a) shows the 3 peaks of CuO located at 300 cm^{-1}, 320 cm^{-1} and 620 cm^{-1}. The spectra are also perfectly reproducible. In contrast Figure 4.15 b) shows an overlay of 6 spectra showing perhaps three peaks located at 120 cm^{-1}, 280 cm^{-1} and 475 cm^{-1}. The spectra are also highly reproducible.

Figure 4.15 shows the comparison of the Raman spectra of CuO and CuS as prepared from Cu pellets 149 μm. Figure 4.15 a) shows the Raman spectra of CuO prepared from the Cu 149 μm pellets. The spectra contain 3 peaks, each corresponding to one of the expected CuO peaks at 300 cm^{-1} (1A$_g$), 320 cm^{-1} (1B$_g$) and 620 cm^{-1} (2B$_g$). As Figure 4.15 b) shows, with such a high concentration of H$_2$S, the largest and clearest peak occurs at 475 cm^{-1}. The ratio of the 475 cm^{-1} peak and the 280 cm^{-1} peak is approximately 7000.

CuS from CuO prepared from Cu(oAs)$_2$

CuS reacted on CuO as prepared by Cu(oAs)$_2$ as heated for 400 °C for 2 – 4 hours as described in section 3.3.2. The Raman spectra of the CuS and the CuO are shown in Figure 4.16.

a)   b)
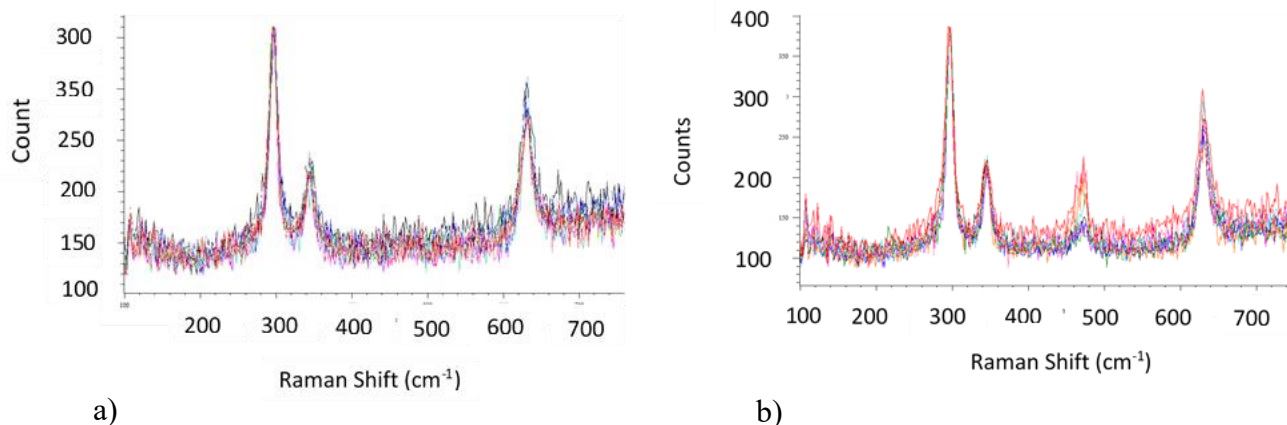
Figure 4.16: Raman spectra of the CuO and CuS as prepared by Cu(oAs)$_2$ heated at 400 °C for 2 to 4 hours. Figure 4.16 a) shows the CuO Raman spectra, which contains 3 peaks located at 300 cm^{-1}, 320 cm^{-1} and 620 cm^{-1}. Figure 4.16 b) shows the corresponding CuS spectra, with 4 peaks at 300 cm^{-1}, 320 cm^{-1}, 475 cm^{-1} and 620 cm^{-1}. The 475 cm^{-1} corresponds the Cu-S – S-Cu bond.

The Figure 4.16 shows a comparison between the CuO and CuS Raman spectra as prepared from Cu(oAs)$_2$. As mentioned earlier, CuO which contains 3 peaks located at 300 cm^{-1}, 320 cm^{-1} and 620 cm^{-1}, each corresponding to one of the expected CuO peaks with great reproducibility. In Figure 4.16 b) the CuS spectra is presented. In the spectra, the three CuO peaks are present, along with the 475 cm^{-1} corresponding to the Cu-S-S-Cu bond. Moreover, it is interesting to note that the 475 cm^{-1} peak is quite small in comparison to the others. As such, although the quality of the CuO is high, the sensitivity to H$_2$S is low.

CuS from CuO prepared from Cu(NO$_3$)$_2$

CuS from CuO as prepared from Cu(NO$_3$)$_2$ was prepared as described in section 3.3.2. The CuO was then exposed to H$_2$S water for 5 mins after which it was rinsed with dH$_2$O and subsequently dried for 1 hour before being measured by the Raman spectrometer. Figure 4.16 shows the Raman spectra of this CuO. All samples of CuO heated at 200 °C to 400 °C for 1 to 4 hours were tested, and none of them gave successful CuS spectra.
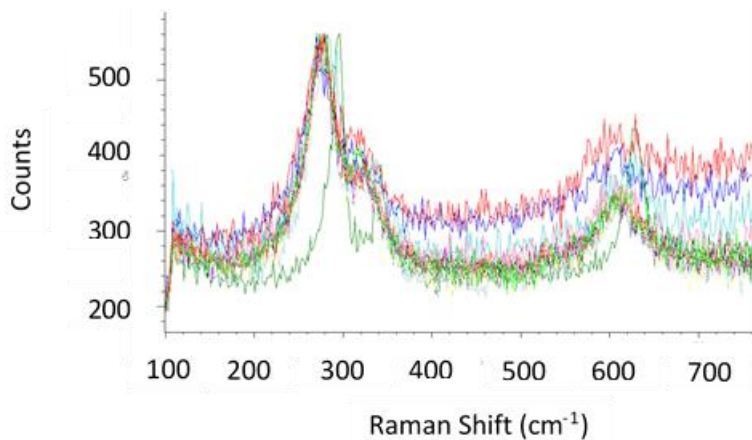
Figure 4.17. Results of the CuS experiment on CuO as prepared from the $Cu(NO_3)_2$. As it can be seen, there is no peak at 475 cm^{-1} therefore there was no CuS peak. As such these CuO samples are disregarded.

4.2. The 4 – Hour Experiment

Introduction:

The previous experiment established the optimal method of CuO synthesis. This experiment builds on the previous by utilizing the optimal CuO to determine the relation between H_2S concentration in solution and peak intensity. In this section, a detailed statistical description of the relationship between the H_2S concentration and the average spectral peak at (approximately) 475 cm^{-1} upon 4 hours of exposure is presented.

4.2.1. Results

The graph of the H_2S concentrations and corresponding peak intensities is shown in Figure 4.18. The results show an increase in the average peak intensities with increasing H_2S concentrations. Although the results show moderate linearity, with an R^2 value of 0.78, the results also show a stronger exponential fitting, with an R^2 of 0.82. Although the exponential fitting appears to be a more accurate description of the data, it's R^2 decreases to 0.75 upon removing the data below the detection limit, whereas the R^2 of the linear model increases to 0.82. As such the data is left unfitted and further measurements are required to distinguish between the two regression models.

72
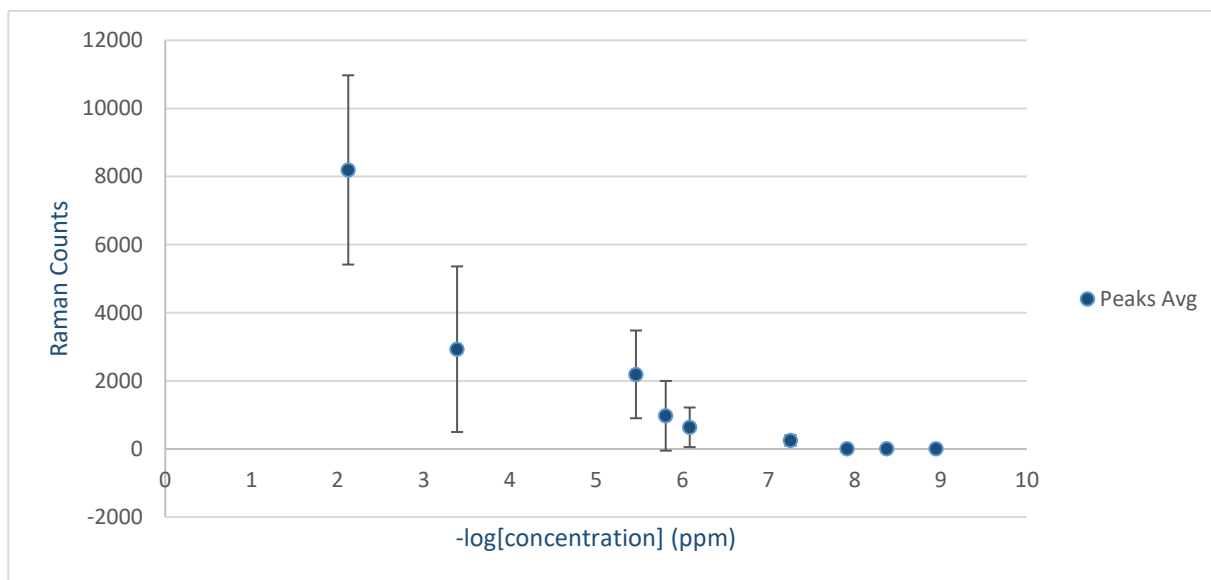
Figure 4.18. Showing the S-S bond peaks located at ~475 cm^{-1} as a function of the negative log of the concentration of H_2S after 4 hours of reaction. The concentrations of H_2S used were 7.53 x10^{-3}, 4.11 x10^{-4}, 3.44 x10^{-6}, 1.55 x10^{-6}, 8.21 x10^{-7}, 5.55 x10^{-8}, 1.22 x10^{-8}, 4.21 x10^{-9} and 1.13 x10^{-9} ppm.

There are some crucial points to discuss about the data obtained in Figure 4.18. Firstly, the data shows an effective measurement range of 7.53 x10^{-3} ppm until 1.22 x10^{-8} ppm (2.21 x10^{-1} M - 3.59 x10^{-7} M) and thus 1.22 x10^{-8} ppm is the effective detection limit.

Secondly, it was found that as concentration decreased the frequency of Cu – S – S – Cu peak decreased. Since the Raman spectra can only be obtained of one spot at a time, in cases where the 475 cm^{-1} spectral peak was not observed, more spectral trials at other locations were taken until a maximum of 1 hour was spent searching. As such, spectra where a "0" peak at 475 cm^{-1} position are obtained have been interpreted as "difficult to find"/ "statistically low frequency of reaction" rather than "no Cu-S-S-Cu bonds on the CuO". Based on this interpretation, the concentrations below the effective detection limit may have reacted with CuO, but due to the low frequency of the reaction it is improbable to find those reactive sites. A few curious observations inspired this interpretation of the data. Firstly, certain spots on the CuO were found to give the 475 cm^{-1} spectra, while directly adjacent to them there was no observed peak. This implies that the Cu-S-S-Cu reaction was not uniform over the CuO samples, but occurred sporadically. By the nature of non-uniform reactions, observation of the Cu-S-S-Cu product (via the 475 cm^{-1} spectral peak) would depend on where one searches. Secondly, the data overwhelmingly shows that higher concentrations of

73

H₂S result in more frequent reactions. As the concentration decreases, it takes longer and longer to find reactive sites yet the maximum time spent searching per sample was only 1 hour.

Furthermore, another critical trend is that as the concentration increases, the standard deviation of the peak intensities increases. The standard deviation of the peak intensities reflects the range of Cu-S-S-Cu present in a sample. As such, it implies that at higher concentrations, there is a greater variance between the extreme values. The interpretation of the result is as follows: the positions of CuO most reactive react very quickly and rapidly increase in Cu-S-S-Cu bonds thus giving large spectral peaks, whereas less reactive sites react more slowly and have much lower peaks. The difference between the highest peaks of the fastest reactions and slowest speed of the least reactive portions is the cause of the large standard deviation. In contrast, the lower concentrations do not contain enough H₂S to produce any observable increase in peak spectra of the least reactive portions. Rather, only the most reactive sites react and develop the Cu -S -S- Cu bonds. As such, the peaks are only detected on the most reactive portions and the standard deviation of the peaks among the most reactive portions is considerably less. This also explains why lower concentrations of H₂S in CuO have smaller standard deviations.

4.3. The Determination of the Rate of Accumulation

In Raman spectroscopy, the band intensities are proportional to the chemical concentration. Thus, the rate of change of the intensity represents the rate of accumulation of CuS on the surface of the CuO. In the context of a point-of-care device, the rate of accumulation is essential to distinguish between slight variations in exposure time and patients with variations in concentrations of H₂S. To illustrate this, let us suppose that the peak intensity corresponding to 7.53×10^{-3} ppm in 1 min is equal to the peak intensity as obtained from 5.56×10^{-8} ppm after 10 hours. How can a detector distinguish between these two peak intensities? The detector must be able to adjust for the time of exposure to distinguish between the two samples. In this chapter a study regarding the rate of accumulation of CuS with 5.55×10^{-8} ppm (1.63×10^{-6} M) concentration of H₂S is conducted.

CuO samples, as prepared in section 3.3.1. were reacted with H₂S solution of a concentration of 5.55×10^{-8} ppm as described in section 3.4.1. Small qualities of CuO samples (< 100 grains) were placed in eppendorf tubes and exposed to the H₂S solution for various periods of time, all at room temperature.

When the reaction time had elapsed, the CuS samples were rinsed with dH$_2$O and dried for at least 1 hour. Subsequently, the Raman spectra of the samples were obtained.

4.3.1. The Rate of Accumulation

The correlation is strongly linear with an R^2 value of 0.98 and a linear range extending from 7,200 seconds (2 hours) until 86,400 seconds (24 hours). Fig 4.19 shows a plot of the band intensity (in Raman counts) against the elapsed time.

The correlation between the concentration and the elapsed time is strongly linear with an R^2 value of 0.98 and a linear range extending from 7200 seconds (2 hours) until 86400 seconds (24 hours). The equation of the rate of accumulation is given by the equation:

$$I = 0.1441t - 1597.6 \qquad\qquad (4.6)$$

$$\frac{\partial I}{\partial t} = 0.1441 \; R/s$$

Regression statistics were obtained on the above correlation with a 95% confidence interval. The regression statistics is presented in Table 4.1, the ANOVA is shown in Table 4.2 followed by the Line of Fit plot in Figure 4.20 and lastly the plot of the residuals in Figure 4.21.
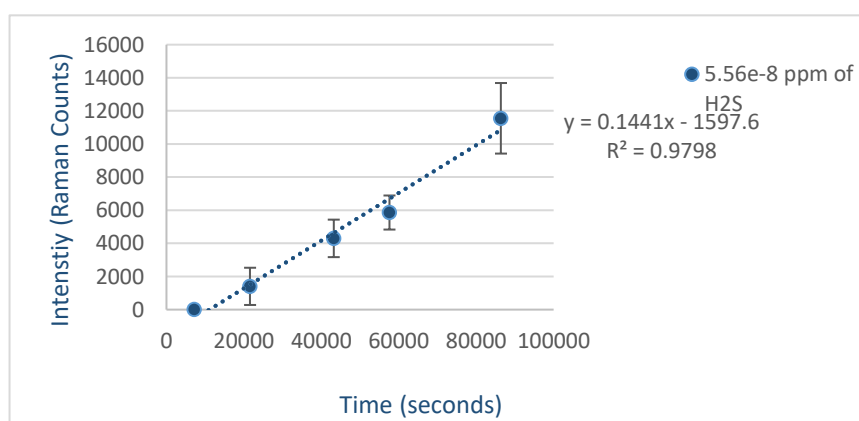
Figure 4.19. Showing the plot of the concentration (measured in Raman counts) against the time elapsed for the experiment. The concentration of H$_2$S used in the experiments was 5.56 x10-8 ppm and the times tested for were 7,200 seconds, 21,600 seconds, 43,200 seconds, 57,600 seconds, and 86,400 seconds.

The temperature is kept constant at room temperature.

Table 4.1: Regression statistics output for peak intensities of the 475 cm^{-1} peak as a function of the H_2S concentration (ppm) solutions over the effective detection limit.

Regression Statistics	
Multiple R	0.99
R Square	0.98
Adjusted R Square	0.97
Standard Error	739.67
Observations	5

Table 4.7: ANOVA for the linear relationship between the H_2S concentration (ppm) over the effective detection limit and the peak intensity of S-S peak at 475 cm^{-1}.

ANOVA

	df	SS	MS	F	Significance F
Regression	1	79648410.7	79648411	145.58	0.0012
Residual	3	1641331.944	547110.6		
Total	4	81289742.64			

	Coefficients	Standard Error	t Stat	P-value	Lower 95%	Upper 95%
Intercept	-1597.59	612.85	-2.61	0.080	-3547.95	352.77
Time (hours)	518.73	42.99	12.07	0.0012	381.91	655.55
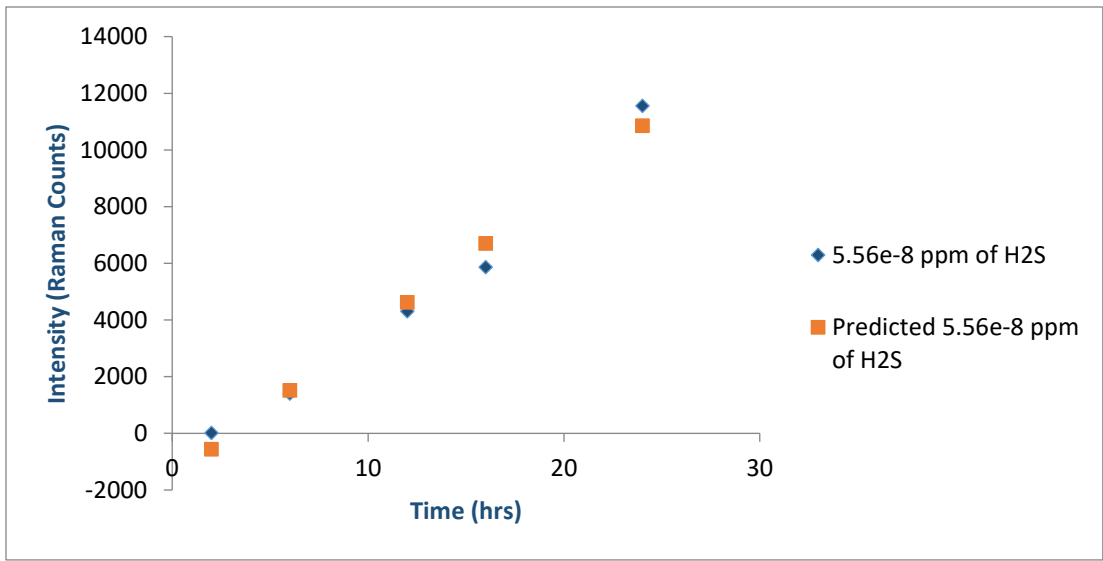
Figure 4.20: The Line Fit plot of the time (hours) and the band intensity (Raman counts). The blue diamonds represent the measured peak intensities whereas the orange squares represent the values predicted by the model. It can be seen that the linear model explains the data fairly accurately.
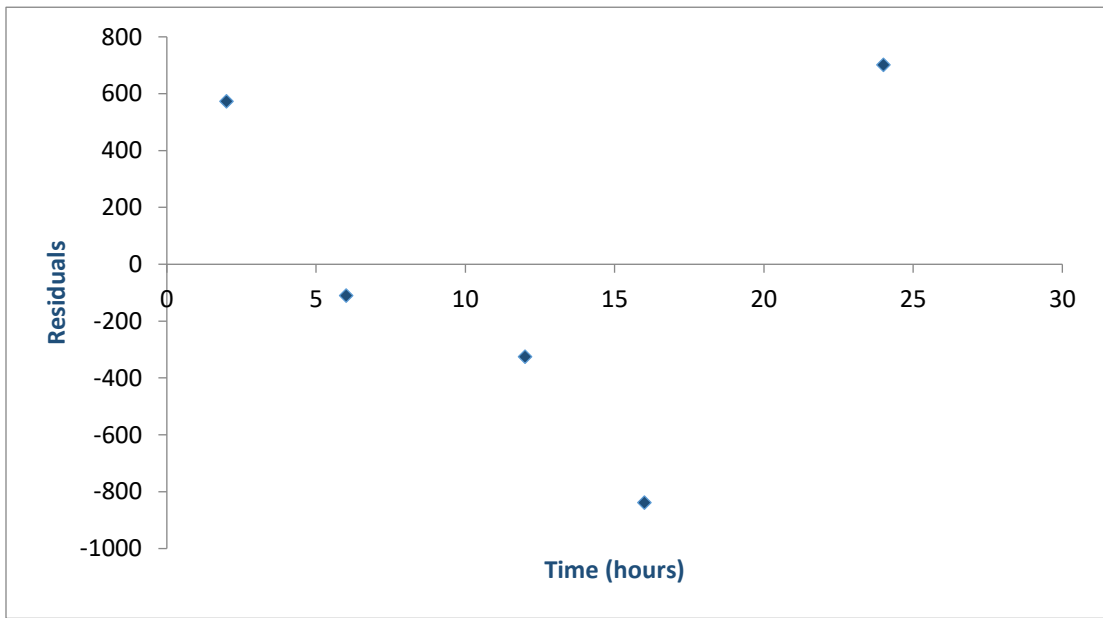
Figure 4.21: The Residual plot for band intensity over the elapsed time (hours). The blue diamonds represent the residual values between the intensity (Raman counts) and the linear regression model that describes the data. The residual plot seems to be random, which provides proof for the existence of a linear relationship between the H_2S concentration and the peak intensities.

The regression statistics show an R^2 value of 0.98. Furthermore, the ANOVA table reveals that F > Significance-F and that significance level of the data is less than 0.01. Coupled with the very strong Line Fit Plot and the random residuals, there is strong evidence that the diffusion increases linearly with time.

4.4. Results of the Specificity Tests

Over the last few hundred years, the role of H_2S has become ever more increasingly important. However, there are other sulfur containing compounds in the body, with the four main compounds being the amino acids L- Cysteine (Cys) (*aq*) and L- Methionine (Met) (*aq*) and SO_4^{2-} (*aq*) and SO_3^{2-} (*aq*). For a clinical diagnosis, the testing material must be sensitive for H_2S, yet indifferent to the other sulfur containing compounds. The clinical concentrations of these sulfur containing compounds in blood plasma are quite small. The clinical concentration of Cys is between 0.57 – 1.79 mg/ L[225] while Met is on the order of 0.85 mg/ 100 mL[226]. SO_3^{2-} and SO_4^{2-} are approximately 3.4 mg/ 100 mL[227].The experimental concentrations used for Cys, Met, SO_4^{2-} and SO_3^{2-} were 3, 2 , 3 and 3 mg/100 mL respectively.

The solutions were prepared as described in section 3.5. Taking Met as an example, 4 mg of Met were dissolved in 100 mL of dH_2O and then a 1 mL aliquot was mixed with 1 mL blood plasma. Subsequently, it was reacted with CuO as prepared in section 3.3.1. for 5 mins.

The Raman spectra of the CuS for each of the samples was obtained.

As it can be seen from the above Figures, there are no peaks at the 475 cm^{-1} location and as such the CuO detector is specific to the H_2S concentration in the blood.
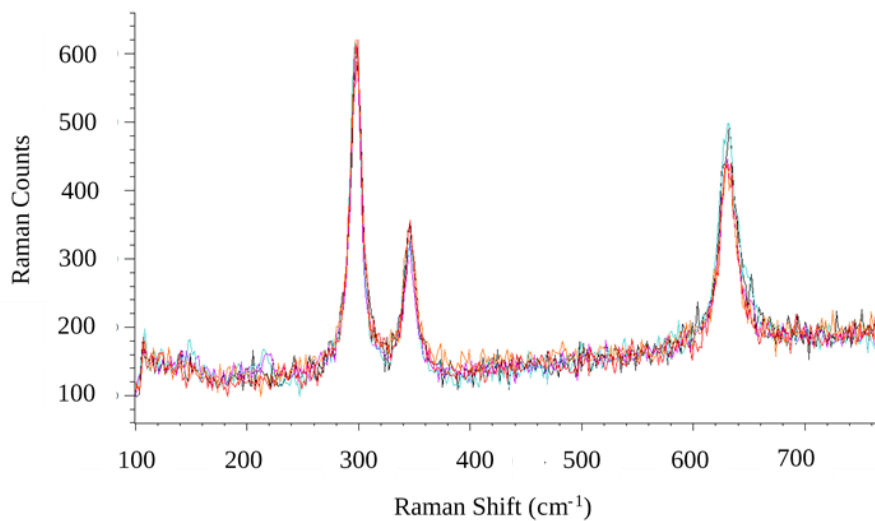
Figure 4.22. Raman spectra of 3 mg/ 100 mL Cys·HCl in blood plasma.
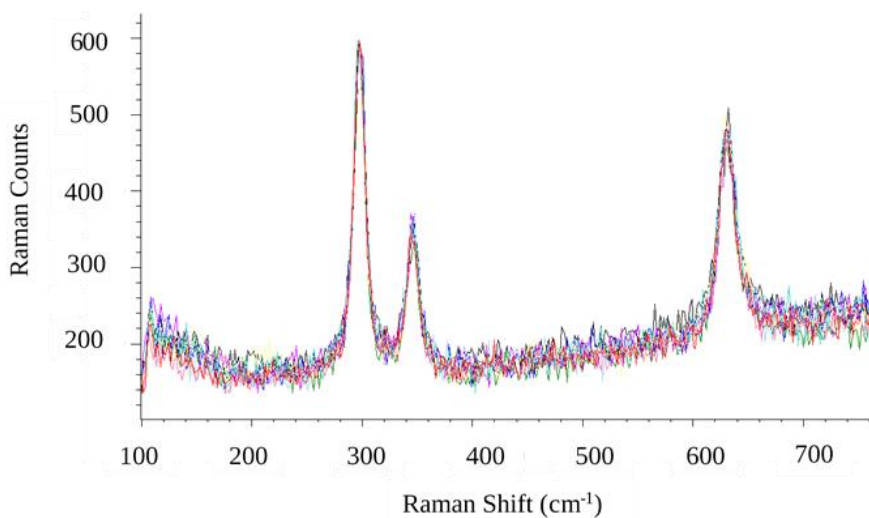
Figure 4.23. Raman spectra of 2 mg/ 100 mL Methionine in blood plasma.
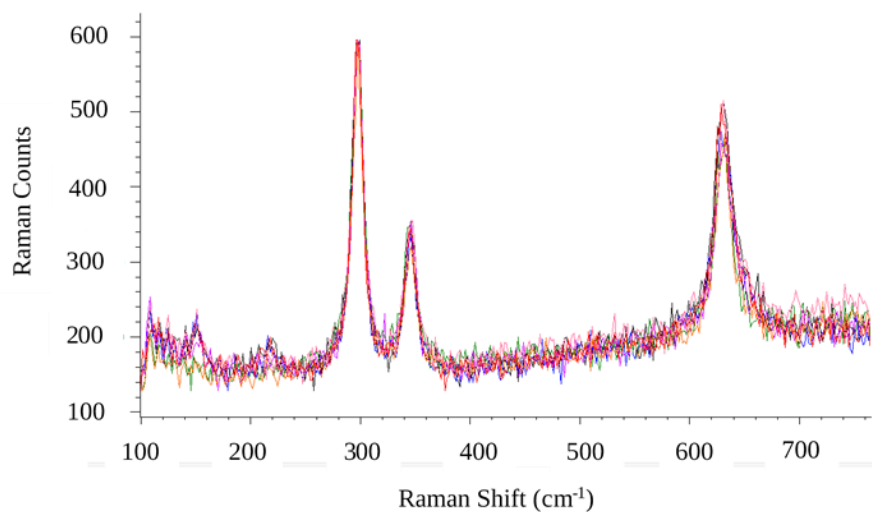
Figure 4.24. Raman spectra of 3 mg/ 100 mL SO_3^{2-} in blood plasma.
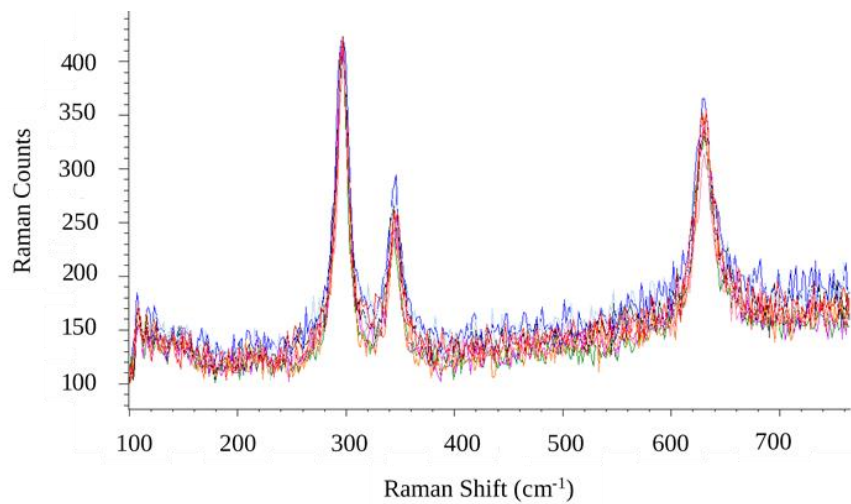
Figure 4.25. Raman spectra of 3 mg/ 100 mL SO_4^{2-} in blood plasma.

CHAPTER 5: CONCLUSIONS AND RECOMMENDATION FOR FUTURE WORK

The optimal method to prepare CuO for H_2S detection was by thermal oxidation of 100 mesh Cu (149 µm) pellets heated at 400 °C for 2 hours in low airflow. These samples were highly reproducible and gave clean and distinct Raman spectra. The reaction of CuO with sulphur containing molecules is a selective for reaction for H_2S. There is a linear response between the intensity of the Raman band at 475 cm^{-1} and the concentration of H_2S in solution. Linearity was established between the range of from 7.53 x10^{-3} and 1.22 x10^{-8} ppm (6.56 x10^{-1} and 3.57 x10^{-7} M). Prolonged exposure of CuO to ultra low concentration of H_2S (ppm) showed that the Raman response increased linearly with time. Thus, it shows that CuO binds H_2S irreversibly and that surface area and accumulation rate are optimizable parameters for better response and detection.

It was illustrated in this thesis that the combination of Raman spectroscopic detection and nano-CuO is a feasible method for development of a rapid and much needed method to detect early onset of diseases such as hypertension and diabetes.

The overall objective of this thesis research was to develop a coupon capable of determining the concentration of H_2S over the range of 0.1 µM – 0.1 M in blood serum. There were four specific objectives which served as milestones for the overall objective:

   (1) determination and optimization of the synthesis of the CuO;

   (2) determination of an optimal CuO/CuS compound;

   (3) determination of the linear detection range as well as the limit of detection of H_2S using CuO;

   (4) determination of the rate of accumulation of CuS in H_2S – serum solution.

5.1. Contributions of the research

The contributions of this research are:

(1) The finding of a novel methodology to measure H_2S (*aq*) concentration utilizing CuO via Raman spectroscopy;

(2) The finding that CuO is specific to H_2S and does not interact with other sulfur compounds;

(3) The finding that CuO is capable of H_2S detection over the 0.1 µM – 0.1 M range in a relatively easy method;

(4) The finding that the H_2S absorption is linear over the expected clinical concentration range.

5.2. Recommendation for Future Work

1: Surface Enhanced Raman Spectroscopy (SERS): With the proper nanomaterial SERS substrate, it is possible to provide 10^7 enhancement of the Raman signal. Other biomaterials, such as proteins, will not interfere with the band intensity since CuO is specific to H_2S. This substrate would allow detection of ppb of H_2S in seconds, rather than hours. Such a substrate could be fabricated from a combination of Au or Ag nano particles with the nano-CuO. A SERS enhanced signal would allow for a simple Raman device with a less sensitive detector. As a warning, one should be careful about choosing a SERS substrate that will not react with H_2S.

2: Electrochemical method of CuS detection

    2.1. Synthesis

        2.1.1. In principle, one should be able to heat the middle of a long and thin copper wire (< 100 µm) in a tube furnace (or other furnace) to obtain a copper wire with CuO in the middle. If the wire is sufficiently thin, all of the Cu would have converted to CuO. Furthermore, the formation of CuS will involve nearly all of the CuO, giving the maximum response in the change in conductivity of this wire.

    2.2. Reaction with H_2S

        2.2.1. The CuO portion can be placed in H_2S solutions and the change conductivity of the wire can be measured in real-time. This means the added information of the rate of change of conductivity can be used as a possible unique identifier of the concentration. Coupled with the change in conductivity, these two characteristic properties should be able to yield the specific H_2S solutions which produced them.

2.2.2. It should also be noted that as electricity is put through a compound, its temperature increases. For single drops of H_2S solutions, small amounts of energy can have tremendous impacts. It should also be noted that warmer solutions are less capable of dissolving H_2S solutions.

2.2.3. A question may arise as to the change in conductivity in a real sample of blood, a sample full of proteins, hormones and cells. It should be noted that since pure blood is an almost perfect insulator of electricity, the conductivity will be correlated to the levels of electrolytes in the blood sample[228,229]. In order to know for sure, experiments must be conducted. However, it is this author's hypothesis that the effects of the electrolytes can be determined and subtracted from the experiment.

2.3. Design of a Detector

2.3.1. The design of a detector will be much simpler using an electrochemical method. The detector will simply measure and record the rate of change of the conductivity and the conductivity at a particular time and compare the values with a standard curve.

2.3.2. The detector will be an incomplete circuit that requires the chip to complete the circuit

The chip will contain the CuO portion of wire (possibly marked with a red-dot to let patients know where to drop the blood).

REFERENCES

1. Kombian, S.B., Warenycia, M.W., Mele, F.G., Reiffenstein, R. J. Effects of Acute intoxication with Hydrogen Sulfide on central amino acid transmitter systems. *Neurotoxicology* **9,** 587–595 (1988).

2. Hannah, R.S., Hayden, L.J., Roth, S. H. Hydrogen sulfide exposure alters the amino acid content in developing rat CNS. *Neurosci. Lett.* **99,** 323–327 (1989).

3. Warenycia, M.W., Karpinski, E., Reiffenstein, R. J. Hydrogen sulfide in combination with taurine or cysteic acid reversibly abolishes sodium currents in neuroblastoma cells. *Neurotoxicology* **10,** 191–199 (1989).

4. Picton, R., Eggo, M. C., Merrill, G. a, Langman, M. J. S. & Singh, S. Mucosal protection against sulphide: importance of the enzyme rhodanese. *Gut* **50,** 201–5 (2002).

5. Mani, S., Cao, W., Wu, L. & Wang, R. Hydrogen sulfide and the liver. *Nitric Oxide* **41,** 62–71 (2014).

6. Bełtowski, J. Hydrogen sulfide in pharmacology and medicine - An update. *Pharmacol. Rep.* **67,** 647–658 (2015).

7. Sonobe, T. & Haouzi, P. H $_2$ S induced coma and cardiogenic shock in the rat: Effects of phenothiazinium chromophores. *Clin. Toxicol.* **53,** 525–539 (2015).

8. Davoli, A. *et al.* Evidence of Hydrogen Sulphide involvement in Amyotrophic Lateral Sclerosis. *Ann. Neurol.* n/a-n/a (2015). doi:10.1002/ana.24372

9. Abe, K. & Kimura, H. The possible role of hydrogen sulfide as an endogenous neuromodulator. *J. Neurosci.* **16,** 1066–1071 (1996).

10. Lobb, I., Sonke, E., Aboalsamh, G. & Sener, A. Hydrogen sulphide and the kidney: important roles in renal physiology and pathogenesis and treatment of kidney injury and disease. *Nitric Oxide* **46,** 55–65 (2015).

11. Kimura, H. The physiological role of hydrogen sulfide and beyond. *Nitric Oxide* **41,** 4–10 (2014).

12. Wei, H.-J., Li, X. & Tang, X.-Q. Therapeutic benefits of H_2S in Alzheimer's disease. *J. Clin. Neurosci.* **21,** 1665–9 (2014).

13. Srilatha, B., Adaikan, P. G., Li, L. & Moore, P. K. Hydrogen sulphide: a novel endogenous gasotransmitter facilitates erectile function. *J. Sex. Med.* **4,** 1304–11 (2007).

14. Qiu, X., Villalta, J., Lin, G. & Lue, T. F. Role of Hydrogen Sulfide in Physiology of Penile Erection. *J Androl* **33,** 529–535 (2012).

15. http://www.horiba.com/scientific/products/oem-mini-ccd-spectrometers/oem-miniature-Raman-systems/.

16. Wu, X. C. *et al.* Using carbon nanotubes to absorb low-concentration hydrogen sulfide in fluid. *IEEE Trans. Nanobioscience* **5,** 204–9 (2006).

17. Wu, X. C. *et al.* Measurement of low concentration and nano-quantity hydrogen sulfide in aqueous solution: measurement mechanisms and limitations. *Meas. Sci. Technol.* **18,** 1315–1320 (2007).

18. Feng, W. Hydrogen Sulfide Adsorption/Oxidation On Carbonaceous Surfaces And Its Application in Vapor Phase Mercury Control. **1,** 1689–1699 (2015).

19. Dombkowski, R. A., Russell, M. J. & Olson, K. R. Hydrogen sulfide as an endogenous regulator of vascular smooth muscle tone in trout. *Am. J. Physiol. Regul. Integr. Comp. Physiol.* **286,** R678-85 (2004).

20. Phillips, D. J. & Phillips, S. L. High temperature dissociation constants of HS- and the standard thermodynamic values for S2-. *J. Chem. Eng. Data* **45,** 981–987 (2000).

21. Eckert, W. Electrochemical Identification of the Hydrogen Sulfide System Using a pH2S (glass/Ag°, Ag2S) Electrode. *J. Electrochem. Soc.* **145,** 77–79 (1998).

22. Lide, D. R. CRC Handbook of Chemistry and Physics. 3485

23. Li, Q. & Lancaster, J. R. Chemical foundations of hydrogen sulfide biology. *Nitric Oxide - Biol. Chem.* **35,** 21–34 (2013).

24. Wang, H., Wu, Y. & Song, J. F. Interface potential sensing from adsorption of human serum albumin (HSA) on carbon nanotube (CNT) monitored by zero current potentiometry for HSA determination. *Biosens. Bioelectron.* **72,** 225–229 (2015).

25. Kremer, J. M., Wilting, J. & Janssen, L. H. Drug binding to human alpha-1-acid glycoprotein in health and disease. *Pharmacol. Rev.* **40,** 1–47 (1988).

26. Wu, X. C. *et al.* Non-functionalized carbon nanotube binding with hemoglobin. *Colloids Surfaces B Biointerfaces* **65,** 146–149 (2008).

27. Caoduro, C. *et al.* Carbon nanotube - Protamine hybrid: Evaluation of DNA cell penetration.

Carbon N. Y. **96,** 742–752 (2016).

28.   Kumar, S., Willander, M., Sharma, J. G. & Malhotra, B. D. A solution processed carbon nanotube modified conducting paper sensor for cancer detection. *J. Mater. Chem. B* **3,** 9305–9314 (2015).

29.   Yoon, J. *et al.* Colloids and Surfaces B : Biointerfaces A biomemory chip composed of a myoglobin / CNT heterolayer fabricated by the protein-adsorption-precipitation-crosslinking (PAPC) technique. **136,** 853–858 (2015).

30.   Balavoine, F. *et al.* Helical Crystallization of Proteins on Carbon Nanotubes: A First Step towards the Development of New Biosensors. *Angew. Chemie Int. Ed.* **38,** 1912–1915 (1999).

31.   Kam, N. W. S. & Dai, H. Carbon nanotubes as intracellular protein transporters: Generality and biological functionality. *J. Am. Chem. Soc.* **127,** 6021–6026 (2005).

32.   Salvador-Morales, C. *et al.* Complement activation and protein adsorption by carbon nanotubes. *Mol. Immunol.* **43,** 193–201 (2006).

33.   Chen, R. J., Zhang, Y., Wang, D. & Dai, H. Noncovalent Sidewall Functionalization of Carbon Nanotubes for Protein Immobilization. *J. Am. Chem. Soc.* **123,** 3838–3839 (2001).

34.   Oski, F. A. & Barness, L. A. Vitamin E deficiency: A previously unrecognized cause of hemolytic anemia in the premature infant. *J. Pediatr.* **70,** 211–220 (1967).

35.   Wang, R. Physiological implications of hydrogen sulfide: a whiff exploration that blossomed. *Physiol. Rev.* **92,** 791–896 (2012).

36.   Whiteman, M. & Moore, P. K. Hydrogen sulfide and the vasculature: a novel vasculoprotective entity and regulator of nitric oxide bioavailability? *J. Cell. Mol. Med.* **13,** 488–507 (2009).

37.   Wallace, J. L., Dicay, M., McKnight, W. & Martin, G. R. Hydrogen sulfide enhances ulcer healing in rats. *FASEB J.* **21,** 4070–4076 (2007).

38.   Wang, R. Hydrogen sulfide: a new EDRF. *Kidney Int.* **76,** 700–4 (2009).

39.   Bates, M. N., Crane, J., Balmes, J. R. & Garrett, N. Investigation of Hydrogen Sulfide Exposure and Lung Function, Asthma and Chronic Obstructive Pulmonary Disease in a Geothermal Area of New Zealand. *PLoS One* **10,** e0122062 (2015).

40.   Yusuf, M. *et al.* Streptozotocin-induced diabetes in the rat is associated with enhanced tissue hydrogen sulfide biosynthesis. *Biochem. Biophys. Res. Commun.* **333,** 1146–1152 (2005).

41.   Wu, L. *et al.* Pancreatic islet overproduction of H2S and suppressed insulin release in Zucker diabetic rats. *Lab. Investig.* **89,** 59–67 (2009).

42.   Liu, W.-Q. Q. *et al.* The cardiovascular effects of central hydrogen sulfide are related to K(ATP)

channels activation. *Physiol. Res.* **60,** 729–38 (2011).

43. Polhemus, D. J. *et al.* Hydrogen sulfide attenuates cardiac dysfunction after heart failure via induction of angiogenesis. *Circ. Heart Fail.* **6,** 1077–86 (2013).

44. Lilyanna, S. *et al.* GYY4137 attenuates remodeling, preserves cardiac function and modulates the natriuretic peptide response to ischemia. *J. Mol. Cell. Cardiol.* **87,** 27–37 (2015).

45. Sanfilippo, F. M. *et al.* Can we monitor heart attack in the troponin era: evidence from a population-based cohort study. *BMC Cardiovasc. Disord.* **11,** 35 (2011).

46. van den Berg, E. *et al.* Urinary sulfur metabolites associate with a favorable cardiovascular risk profile and survival benefit in renal transplant recipients. *J. Am. Soc. Nephrol.* **25,** 1303–12 (2014).

47. Zavaczki, E. *et al.* Hydrogen sulfide inhibits the calcification and osteoblastic differentiation of vascular smooth muscle cells. *Kidney Int.* **80,** 731–9 (2011).

48. Stanford, W., Thompson, B. H. & Weiss, R. M. Coronary artery calcification: clinical significance and current methods of detection. *AJR Am J Roentgenol* **161,** 1139–1146 (1993).

49. Loecker, T. H., Schwartz, R. S., Cotta, C. W. & Hickman, J. R. Fluoroscopic coronary artery calcification and associated coronary disease in asymptomatic young men. *J. Am. Coll. Cardiol.* **19,** 1167–1172 (1992).

50. Al-Magableh, M. R. & Hart, J. L. Mechanism of vasorelaxation and role of endogenous hydrogen sulfide production in mouse aorta. *Naunyn. Schmiedebergs. Arch. Pharmacol.* **383,** 403–13 (2011).

51. Yang, G. *et al.* H2S as a physiologic vasorelaxant: hypertension in mice with deletion of cystathionine gamma-lyase. *Science* **322,** 587–90 (2008).

52. Kimura, H. *Hydrogen Sulfide and its Therapeutic Applications*. *Hydrogen Sulfide and its Therapeutic Applications* (Springer Vienna, 2013). doi:10.1007/978-3-7091-1550-3

53. Ogedegbe, G. *et al.* The misdiagnosis of hypertension: the role of patient anxiety. *Arch. Intern. Med.* **168,** 2459–65 (2008).

54. Xia, M., Chen, L., Muh, R. W., Li, P.-L. & Li, N. Production and actions of hydrogen sulfide, a novel gaseous bioactive substance, in the kidneys. *J. Pharmacol. Exp. Ther.* **329,** 1056–62 (2009).

55. Giuliani, D. *et al.* Hydrogen sulfide slows down progression of experimental Alzheimer's disease by targeting multiple pathophysiological mechanisms. *Neurobiol. Learn. Mem.* **104,** 82–91 (2013).

56. Morrison, L. D., Smith, D. D. & Kish, S. J. Brain S-adenosylmethionine levels are severely decreased in Alzheimer's disease. *J. Neurochem.* **67,** 1328–1331 (1996).

57. Gong, Q.-H. *et al.* Hydrogen sulfide attenuates lipopolysaccharide-induced cognitive impairment: a pro-inflammatory pathway in rats. *Pharmacol. Biochem. Behav.* **96,** 52–8 (2010).

58. Archibald, N. K., Clarke, M. P., Mosimann, U. P. & Burn, D. J. The retina in Parkinsons disease. *Brain* **132,** 1128–1145 (2009).

59. Birtwistle, J. & Baldwin, D. role of dopamine in schizophrenia and parkinsons disease. *Br. J. Nurs.* **7,** 832–841 (1998).

60. Boileau, I. *et al.* Decreased binding of the D3 dopamine receptor-preferring ligand [11C]-()-PHNO in drug-nave Parkinsons disease. *Brain* **132,** 1366–1375 (2009).

61. Zhang, J. *et al.* Hydrogen Sulfide Prevents Hydrogen Peroxide-Induced Activation of Epithelial Sodium Channel through a PTEN/PI(3,4,5)P3 Dependent Pathway. *PLoS One* **8,** e64304 (2013).

62. Wintner, E. a. *et al.* A monobromobimane-based assay to measure the pharmacokinetic profile of reactive sulphide species in blood. *Br. J. Pharmacol.* **160,** 941–957 (2010).

63. Filipovic, M. R. *et al.* Biochemical insight into physiological effects of H$_2$S: reaction with peroxynitrite and formation of a new nitric oxide donor, sulfinyl nitrite. *Biochem. J.* **441,** 609–21 (2012).

64. Zaidman. Variable localization of metal removal during the electrochemical milling of copper in nitrate solutions. (1986).

65. Hirai, T. & Yamane, H. MOCVD superconducting oxide films. *J. Cryst. Growth* **107,** 683–691 (1991).

66. Sung, HM, Chen, CJ, Ko, WS, Lin, H. Fine Powder Ferrite for Multilayer Chip Inductors. *IEEE Trans. Magn.* (1994).

67. Zhu, Yimei, Zhang, Hong, Suenaga, M, Welch, D. Planar defects induced by heavy-ion irradiation. *Philos. Mag.* **68,** 1079–1089 (1993).

68. Tanaka, M., Fukushima, S., Suzuki, M., Isobe, M. & Ami, T. Electrical and structural properties of CuO-SrPbO3-Ag ceramic composites. *Mater. Lett.* **20,** 275–278 (1994).

69. Guo, H. & Zhang, J. Synthesis of YBa2Cu4O8 ceramics at one atmosphere pressure in oxygen. *Appl. Supercond.* **1,** 1973–1980 (1993).

70. Ma, Xueming, Yue, L, Dong, Y. Mechanical reduction of CuO by Mg at room temperature. (1992).

71. Hirai, T. & Sasaki, M. In-situ processing of inorganic composites by chemical vapor deposition. *Ceram. Int.* **17,** 275–281 (1991).

72. Wu, D., Zhang, Q. & Tao, M. LSDA+U study of cupric oxide: Electronic structure and native point defects. *Phys. Rev. B - Condens. Matter Mater. Phys.* **73,** (2006).

73. Meyer, B. K. *et al.* Binary copper oxide semiconductors: From materials towards devices. *Phys. Status Solidi* **249,** 1487–1509 (2012).

74. Bourne, L. C., Yu, P. Y., Zettl, A. & Cohen, M. L. High-pressure electrical conductivity measurements in the copper oxides. *Phys. Rev. B* **40,** 10973–10976 (1989).

75. Azam, A., Ahmed, A. S., Oves, M., Khan, M. S. & Memic, A. Size-dependent antimicrobial properties of CuO nanoparticles against Gram-positive and -negative bacterial strains. *Int. J. Nanomedicine* **7,** 3527–3535 (2012).

76. Vidyasagar, C. C., Naik, Y. A., Venkatesha, T. G. & Viswanatha, R. Solid-State Synthesis and Effect of Temperature on Optical Properties of CuO Nanoparticles. *Nano-Micro Lett.* **4,** 73–77 (2012).

77. Azam, A., Ahmed,A.S., Oves,M.,Khan,MS.,Memic, A. Size-dependent antimicrobial properties of CuO nanoparticles against Gram-positive and -negative bacterial strains. *Int. J. Nanomedicine* **7,** 3527–3535 (2012).

78. H.F. Goldstein, Dai-sek Kim, P. Y. Y. Raman Study of CuO single crystals. **41,** 514 (1990).

79. Ferrari, a C. & Basko, D. M. Raman spectroscopy as a versatile tool for studying the properties of graphene. *Nat. Nanotechnol.* **8,** 235–246 (2013).

80. Anandan, S. & Yang, S. Emergent methods to synthesize and characterize semiconductor CuO nanoparticles with various morphologies – an overview. *J. Exp. Nanosci.* **2,** 23–56 (2007).

81. Wang , W. ; Wang , L. ; Shi , H. ; Liang, Y. A room temperature chemical route for large scale synthesis of sub-15 nm ultralong CuO nanowires with strong size effect and enhanced photocatalytic activity. *CrystEngComm* **14,** 5914–5922 (2012).

82. Xu, J.F., ; Ji, W., ; Shen, X.W., ; Li, W.S., ; Tang, S.H. ; Ye, W.R., ; Jia, D.Z., ; Xin, X.Q. Raman spectra of CuO nanocrystals. *J. Raman Spectrosc.* **30,** 413–415 (1999).

83. Zou, G. *et al.* Well-aligned arrays of CuO nanoplatelets. *J. Phys. Chem. B* **110,** 1632–1637 (2006).

84. Al-Kuhaili, M. F. Characterization of copper oxide thin films deposited by the thermal evaporation of cuprous oxide (Cu2O). *Vacuum* **82,** 623–629 (2008).

85. Johan, M. R., Suan, M. S. M., Hawari, N. L. & Ching, H. A. Annealing effects on the properties of copper oxide thin films prepared by chemical deposition. *Int. J. Electrochem. Sci.* **6,** 6094–6104 (2011).

86. Jeong, Y. K. & Choi, G. M. Nonstoichiometry and electrical conduction of CuO. *J. Phys. Chem. Solids* **57,** 81–84 (1996).

87. Grzesik, Z., Migdalska, M. Oxidation Mechanism of Cu2O and Defect Structure of CuO at High Temperatures. *High Temp. Matter Process.* **30,** 277–287 (2011).

88. Yang, M. & He, J. Fine tuning of the morphology of copper oxide nanostructures and their application in ambient degradation of methylene blue. *J. Colloid Interface Sci.* **355,** 15–22 (2011).

89. Borgohain, K., ; Mahamuni, S. Formation of Single-phase CuO Quantum Particles. *J. Mater. Res.* **17,** 1220–1223 (2002).

90. Hu, J., Li, D., Lu, J. G. & Wu, R. Effects on electronic properties of molecule adsorption on CuO surfaces and nanowires. *J. Phys. Chem. C* **114,** 17120–17126 (2010).

91. Hsu, C. Ethanol Gas and Humidity Sensors of CuO/Cu2O Composite Nanowires Based on a Cu Through-Silicon Via Approach. *Sensors Actuators B Chem.* 95–102 (2016).

92. Zheng, H. *et al.* Nanostructured tungsten oxide - Properties, synthesis, and applications. *Adv. Funct. Mater.* **21,** 2175–2196 (2011).

93. Ohya, Y., Ito, S., Ban, T. & Takahashi, Y. Preparation of CuO Thin Films and Their Electrical Conductivity. *Key Eng. Mater.* **181–182,** 113–116 (2000).

94. Serin, T., Yildiz, A., Horzum Şahin, Ş. & Serin, N. Extraction of important electrical parameters of CuO. *Phys. B Condens. Matter* **406,** 575–578 (2011).

95. Serin, T., Yildiz, A., Şahin, Ş. H. & Serin, N. Multiphonon hopping of carriers in CuO thin films. *Phys. B Condens. Matter* **406,** 3551–3555 (2011).

96. Nair, M. T. ., Guerrero, L., Arenas, O. L. & Nair, P. . Chemically deposited copper oxide thin films: structural, optical and electrical characteristics. *Appl. Surf. Sci.* **150,** 143–151 (1999).

97. Jundale, D.M., ; Joshi, P.B., ; Sen, S., ; Patil, V.B. Nanocrystalline CuO thin films: synthesis, microstructural and optoelectronic properties. *J. Mater. Sci. Mater. Electron.* **23,** 1492–1499 (2012).

98. Kryukova, N.G., Zaikovskii,I.V., Sadykov, V.A., Bulgakov, N. N. Nature of extended defects of CuO. *React. Kinet. Catal. Lett.* **32,** 111–115 (1986).

99. Terakura, K., ; Oguchi, T., ; Williams, A. R., ; Kubler, J. Band theory of insulating transition-metal

monoxides: Band-structure calculations. *Phys. Rev. B* **30,** 4734–4747 (1984).

100. Norman, M.R., ; Freeman, A.J. Model supercell local-density calculations of the 3 d excitation spectra in NiO. *Phys. Rev. B* **33,** 8896–8898 (1986).

101. Seehra, M. S. & Punnoose, A. Particle size dependence of exchange-bias and coercivity in CuO nanoparticles. *Solid State Commun.* **128,** 299–302 (2003).

102. Zheng, X. G., Mori, T., Nishiyama, K., Higemoto, W. & Xu, C. N. Dramatic suppression of antiferromagnetic coupling in nanoparticle CuO. *Solid State Commun.* **132,** 493–496 (2004).

103. Yang, K. G. *et al.* Room-temperature ferromagnetic CuO thin film grown by plasma-assisted molecular beam epitaxy. *Mater. Lett.* **166,** 23–25 (2016).

104. Goldman, A. I., Yang, B. X., Tranquada, J., Crow, J. E. & Jee, C.-S. Antiferromagnetic order in Dy Ba 2 Cu 3 O 7. *Phys. Rev. B* **36,** 7234–7236 (1987).

105. Azzoni, C. B., Paleari, A. & Parravicini, G. B. On the low-temperature magnetic-properties of CuO single-crystals. *J. Phys.-Condes. Matter* **4,** 1359–1366 (1992).

106. Narsinga Rao, G., Yao, Y. D. & Chen, J. W. Evolution of size, morphology, and magnetic properties of CuO nanoparticles by thermal annealing. *J. Appl. Phys.* **105,** (2009).

107. Forsyth, J. B., Brown, P. J. & Wanklyn, B. M. Magnetism in Cupric Oxide. *J. Phys. C Solid State Phys.* **21,** 2917–2929 (1988).

108. Yang, B. X., Thurston, T. R., Tranquada, J. M. & Shirane, G. Magnetic neutron scattering study of single-crystal cupric oxide. *Phys. Rev. B* **39,** 4343–4349 (1989).

109. Rehman, S., Mumtaz, A. & Hasanain, S. K. Size effects on the magnetic and optical properties of CuO nanoparticles. *J. Nanoparticle Res.* **13,** 2497–2507 (2011).

110. Sukhorukov, Y. P.,; Loshkareva, N. N.,; Samokhvalov, A. A.,; Naumov, S. V.,; Moskvin, A. S.,; Ovchinnikov, A. S. Magnetic phase transitions in optical spectrum of magnetic semiconductor CuO. *J. Magn. Magn. Mater.* **183,** 356–358 (1998).

111. Jiang, X., Herricks, T. & Xia, Y. CuO Nanowires Can Be Synthesized by Heating Copper Substrates in Air. *Nano Lett.* **2,** 1333–1338 (2002).

112. Kumar, A., Srivastava, a K., Tiwari, P. & Nandedkar, R. V. The effect of growth parameters on the aspect ratio and number density of CuO nanorods. *J. Phys. Condens. Matter* **16,** 8531–8543 (2004).

113. Cheng, S.-L. & Chen, M.-F. Fabrication, characterization, and kinetic study of vertical single-crystalline CuO nanowires on Si substrates. *Nanoscale Res. Lett.* **7,** 119 (2012).

114. Zhang, K., Rossi, C., Tenailleau, C., Alphonse, P. & Chane-Ching, J.-Y. Synthesis of large-area and aligned copper oxide nanowires from copper thin film on silicon substrate. *Nanotechnology* **18,** 275607 (2007).

115. Tsai, C.-M. *et al.* CuO nanowire synthesis catalyzed by a CoWP nanofilter. *Acta Mater.* **57,** 1570–1576 (2009).

116. Chen, J. T. *et al.* CuO nanowires synthesized by thermal oxidation route. *J. Alloys Compd.* **454,** 268–273 (2008).

117. Mema, R., Yuan, L., Du, Q., Wang, Y. & Zhou, G. Effect of surface stresses on CuO nanowire growth in the thermal oxidation of copper. *Chem. Phys. Lett.* **512,** 87–91 (2011).

118. yuan , Lu., ; Zhou , G. Enhanced CuO Nanowire Formation by Thermal Oxidation of Roughened Copper. *J. Electrochem. Soc.* **159,** (2012).

119. Tiwari, J. N., Tiwari, R. N. & Kim, K. S. Zero-dimensional, one-dimensional, two-dimensional and three-dimensional nanostructured materials for advanced electrochemical energy devices. *Prog. Mater. Sci.* **57,** 724–803 (2012).

120. Zhuang, Z., Peng, Q. & Li, Y. Controlled synthesis of semiconductor nanostructures in the liquid phase. *Chem. Soc. Rev.* **40,** 5492 (2011).

121. Xia, Y. *et al.* One-Dimensional Nanostructures: Synthesis, Characterization, and Applications. *Adv. Mater.* **15,** 353–389 (2003).

122. Cao, M. *et al.* A controllable synthetic route to Cu, Cu2O, and CuO nanotubes and nanorods. *Chem. Commun. (Camb).* **1,** 1884–1885 (2003).

123. Gao , X.P. , ; Bao , J., ; Pan , G.L. , ; Song, D. Y. J. Preparation and Electrochemical Performance of Polycrystalline and Single Crystalline CuO Nanorods as Anode Materials for Li Ion Battery. *J. Phys. Chem. B* **108,** 5547–5551 (2004).

124. Volanti, D. P., Orlandi, M. O., Andrés, J. & Longo, E. Efficient microwave-assisted hydrothermal synthesis of CuO sea urchin-like architectures via a mesoscale self-assembly. *CrystEngComm* **12,** 1696 (2010).

125. Ethiraj, A. S. & Kang, D. J. Synthesis and characterization of CuO nanowires by a simple wet chemical method. *Nanoscale Res. Lett.* **7,** 70 (2012).

126. Liu, B. & Zeng, H. C. Mesoscale organization of CuO nanoribbons: Formation of 'dandelions'. *J. Am. Chem. Soc.* **126,** 8124–8125 (2004).

127. Guan, X. *et al.* Hierarchical CuO hollow microspheres: Controlled synthesis for enhanced lithium

storage performance. *J. Alloys Compd.* **509,** 3367–3374 (2011).

128. Shaabani, B., Alizadeh-Gheshlaghi, E., Azizian-Kalandaragh, Y. & Khodayari, A. Preparation of CuO nanopowders and their catalytic activity in photodegradation of Rhodamine-B. *Adv. Powder Technol.* **25,** 1043–1052 (2014).

129. Liu, J. *et al.* Self-assembled CuO monocrystalline nanoarchitectures with controlled dimensionality and morphology. *Cryst. Growth Des.* **6,** 1690–1696 (2006).

130. Fan, H. *et al.* Controlled synthesis of monodispersed CuO nanocrystals. *Nanotechnology* **15,** 37–42 (2004).

131. Zhang, Z. *et al.* Three-dimensionally oriented aggregation of a few hundred nanoparticles into monocrystalline architectures. *Adv. Mater.* **17,** 42–47 (2005).

132. Zhang, Y. *et al.* CuO shuttle-like nanocrystals synthesized by oriented attachment. *J. Cryst. Growth* **291,** 196–201 (2006).

133. Xu, X., Yang, H. & Liu, Y. Self-assembled structures of CuO primary crystals synthesized from Cu(CH3COO)2–NaOH aqueous systems. *CrystEngComm* **14,** 5289 (2012).

134. Dar, M. A., Kim, Y. S., Kim, W. B., Sohn, J. M. & Shin, H. S. Structural and magnetic properties of CuO nanoneedles synthesized by hydrothermal method. *Appl. Surf. Sci.* **254,** 7477–7481 (2008).

135. Neupane, M. P. *et al.* Temperature driven morphological changes of hydrothermally prepared copper oxide nanoparticles. *Surf. Interface Anal.* **41,** 259–263 (2009).

136. Outokesh, M. *et al.* Hydrothermal synthesis of CuO nanoparticles: Study on effects of operational conditions on yield, purity, and size of the nanoparticles. *Ind. Eng. Chem. Res.* **50,** 3540–3554 (2011).

137. Shrestha , K., ; Sorensen , C. , ; Klabunde, J., ; Synthesis of CuO Nanorods, Reduction of CuO into Cu Nanorods, and Diffuse Reflectance Measurements of CuO and Cu Nanomaterials in the Near Infrared Region. *J. Phys. Chem. C* **114,** 14368–14376 (2010).

138. Chakraborty, S. *et al.* Vibrational Properties Of CuO Nanoparticles Synthesized By Hydrothermal Technique. **841,** 841–842 (2011).

139. Yang , M. , ; He , J. , ; Hu , X. , ;Yan , C. ,; Cheng, Z. ; CuO Nanostructures As Quartz Crystal Microbalance Sensing Layers for Detection of Trace Hydrogen Cyanide Gas. *Environ. Sci. Technol.* **45,** 6088–6094 (2011).

140. Sue, K. *et al.* Continuous hydrothermal synthesis of Fe2O3, NiO, and CuO nanoparticles by

superrapid heating using a T-type micro mixer at 673K and 30MPa. *Chem. Eng. J.* **166,** 947–953 (2011).

141. Srivastava, R., Anu Prathap, M. U. & Kore, R. Morphologically controlled synthesis of copper oxides and their catalytic applications in the synthesis of propargylamine and oxidative degradation of methylene blue. *Colloids Surfaces A Physicochem. Eng. Asp.* **392,** 271–282 (2011).

142. Borgohain, K. & Mahamuni, S. Formation of Single-phase CuO Quantum Particles. *J. Mater. Res.* **17,** 1220–1223 (2011).

143. Poizot, P. , ; Hung , C. , ; Nikiforov, M. , ; Bohannam, E., ; Switzer , J., ; An Electrochemical Method for CuO Thin Film Deposition from Aqueous Solution. *Electrochem. Solid-State Lett.* **6,** (2003).

144. Yuan, G.-Q., Jiang, H.-F., Lin, C. & Liao, S.-J. Shape- and size-controlled electrochemical synthesis of cupric oxide nanocrystals. *J. Cryst. Growth* **303,** 400–406 (2007).

145. Chen, L. B., Lu, N., Xu, C. M., Yu, H. C. & Wang, T. H. Electrochemical performance of polycrystalline CuO nanowires as anode material for Li ion batteries. *Electrochim. Acta* **54,** 4198–4201 (2009).

146. Goli, M., Haratizadeh, H. & Ebrahimizadeh Abrishami, M. Growth of flower-like copper oxide nanostructures by glow discharge in water. *Ceram. Int.* **40,** 16071–16075 (2014).

147. Huang, M. *et al.* Merging of Kirkendall growth and Ostwald ripening: CuO@MnO2 core-shell architectures for asymmetric supercapacitors. *Sci. Rep.* **4,** 4518 (2014).

148. Wagner, C. Theorie der Alterung von Niederschlägen durch Umlösen (Ostwald-Reifung). *Zeitschrift für Elektrochemie, Berichte der Bunsengesellschaft für Phys. Chemie* **65,** 581–591 (1961).

149. Kahlweit, M. Uber den derzeitigen Stand der Umlosungstheorie (Ostwald-Reifung). *Chemie Ing. Tech.* **48,** 676–679 (1976).

150. Noorduin, W. L., Vlieg, E., Kellogg, R. M. & Kaptein, B. Von der Ostwald-Reifung zur Homochiralität. *Angew. Chemie* **121,** 9778–9784 (2009).

151. Holleman, A. & Wiberg, E. *Lehrbuch der Anorganischen Chemie*. *Journal of Chemical Information and Modeling* **53,** (1995).

152. Moura, A. P. *et al.* Structure and growth mechanism of CuO plates obtained by microwave-hydrothermal without surfactants. *Adv. Powder Technol.* **21,** 197–202 (2010).

153. Wang, X., Yang, J., Shi, L., Gao,M. Surfactant-free Synthesis of CuO with Controllable Morphologies and Enhanced Photocatalytic Property. *Nanoscale Res. Lett.* **11,** (2016).

154. Qin, Y., ; Zhang, F.,; Chen,Y., ; Zhou, Y., ; Li, J., ; Zhu, A., ; Luo, Y., ; Tian, Y., ; Yang, J., ; Hierarchically Porous CuO Hollow Spheres Fabricated via a One-Pot Template-Free Method for High-Performance Gas Sensors. *J. Phys. Chem. C* **116,** 11994–12000 (2012).

155. Zhang, W., Wen, X. & Yang, S. Controlled reactions on a copper surface: synthesis and characterization of nanostructured copper compound films. *Inorg. Chem.* **42,** 5005–5014 (2003).

156. Hou, H., Xie, Y. & Li, Q. Large-scale synthesis of single-crystalline quasi-aligned submicrometer CuO ribbons. *Cryst. Growth Des.* **5,** 201–205 (2005).

157. Zhang, W., Wen, X., Yang, S., Berta, Y. & Wang, Z. L. Single-crystalline scroll-type nanotube arrays of copper hydroxide synthesized at room temperature. *Adv. Mater.* **15,** 822–825 (2003).

158. Wen, X., Zhang, W., Yang, S., Dai, Z. R. & Wang, Z. L. Solution Phase Synthesis of Cu(OH)2 Nanoribbons by Coordination Self-Assembly Using Cu2S Nanowires as Precursors. *Nano Lett.* **2,** 1397–1401 (2002).

159. Liu, Y. *et al.* Anion-controlled construction of CuO honeycombs and flowerlike assemblies on copper foils. *Cryst. Growth Des.* **7,** 467–470 (2007).

160. Kaur, M. *et al.* Growth and branching of CuO nanowires by thermal oxidation of copper. *J. Cryst. Growth* **289,** 670–675 (2006).

161. Shao, P., Deng, S., Chen, J. & Xu, N. Large-scale fabrication of ordered arrays of microcontainers and the restraint effect on growth of CuO nanowires. *Nanoscale Res. Lett.* **6,** 86 (2011).

162. Goncalves , A.B., ; Campos , L., ; Ferlauto , A.S., ; Lacerda , R. On the Growth and Electrical Characterization of CuO Nanowires by Thermal Oxidation. *J. Appl. Phys.* **106,** 034303–034303 (2009).

163. Bokstein, B. S., Fradkov, V. E. & Beke, D. L. Grain boundary segregation and grain-boundary heterodiffusion. *Philos. Mag. A* **65,** 277–286 (1992).

164. Herbig, M. *et al.* Atomic-scale quantification of grain boundary segregation in nanocrystalline material. *Phys. Rev. Lett.* **112,** (2013).

165. Liu, F. & Kirchheim, R. Grain boundary saturation and grain growth. *Scr. Mater.* **51,** 521–525 (2004).

166. Thongbai, P., Maensiri, S. & Yamwong, T. Effects of grain, grain boundary, and dc electric field on giant dielectric response in high purity CuO ceramics. *J. Appl. Phys.* **104,** (2008).

167. Zhu, Y., Mimura, K. & Isshiki, M. Influence of oxide grain morphology on formation of the CuO scale during oxidation of copper at 600-1000°C. *Corros. Sci.* **47,** 537–544 (2005).

168. Yuan, L., Wang, Y., Mema, R. & Zhou, G. Driving force and growth mechanism for spontaneous oxide nanowire formation during the thermal oxidation of metals. *Acta Mater.* **59,** 2491–2500 (2011).

169. Jia, W. *et al.* Vertically aligned CuO nanowires based electrode for amperometric detection of hydrogen peroxide. *Electroanalysis* **20,** 2153–2157 (2008).

170. Zhong, M. L. *et al.* Synthesis, growth mechanism and gas-sensing properties of large-scale CuO nanowires. *Acta Mater.* **58,** 5926–5932 (2010).

171. Hansen, B. J., Chan, H. (Iris), Lu, J., Lu, G. & Chen, J. Short-circuit diffusion growth of long bi-crystal CuO nanowires. *Chem. Phys. Lett.* **504,** 41–45 (2011).

172. Wang, J. Glucose biosensors: 40 Years of advances and challenges. *Electroanalysis* **13,** 983–988 (2001).

173. Wang, J. in *Electrochemical Sensors, Biosensors and their Biomedical Applications* 57–69 (Elsevier Inc., 2008).

174. Carnes, C.L. , Stipp, J., Klabunde , K.J. Synthesis, Characterization and Adsorption Studies of Nanocrystalline Copper Oxide and Nickel Oxide. *Langmuir* **18,** 1352–1359 (2002).

175. Borgohain, K., Singh, J. B., Rama Rao, M. V., Shripathi, T. & Mahamuni, S. Quantum size effects in CuO nanoparticles. *Phys. Rev. B* **61,** 11093–11096 (2000).

176. Xu, C. , Liu, Y. , Xu, G. , Wang, G. Preparation and characterization of CuO nanorods by thermal decomposition of CuC2O4 precursor. *Mater. Res. Bull.* **37,** 2365–2372 (2002).

177. Hong, Z.S., Cao, Y., Deng, J.F. A convenient alcohothermal approach for low temperature synthesis of CuO nanoparticles. *Mater. Lett.* **52,** 34–38 (2002).

178. Jiang, X.C., Herricks, T., Xia, Y. N. CuO Nanowires Can Be Synthesized by Heating Copper Substrates in Air. *Nano Lett.* **2,** 1333–1338 (2002).

179. Chaichi, M., Ehsani, M. Determination of Glucose and Cholesterol Using a Novel Optimized Luminol- CuO Nanoparticles-H2O2 Chemiluminescence Method by Box–Behnken Design. *J. Fluoresc.* **25,** 861–870 (2015).

180. Aslani, A. & Oroojpour, V. CO gas sensing of CuO nanostructures, synthesized by an assisted solvothermal wet chemical route. *Phys. B Condens. Matter* **406,** 144–149 (2011).

181. Liao, L. *et al.* Multifunctional CuO nanowire devices: p-type field effect transistors and CO gas

sensors. *Nanotechnology* **20,** 85203 (2009).

182. Kim, Y.-S., Hwang, I.-S., Kim, S.-J., Lee, C.-Y. & Lee, J.-H. CuO nanowire gas sensors for air quality control in automotive cabin. *Sensors Actuators B Chem.* **135,** 298–303 (2008).

183. Steinhauer, S. *et al.* Gas sensing properties of novel CuO nanowire devices. *Sensors Actuators B Chem.* **187,** 50–57 (2013).

184. Reitz, J. B. & Solomon, E. I. Propylene oxidation on copper oxide surfaces: Electronic and geometric contributions to reactivity and selectivity. *J. Am. Chem. Soc.* **120,** 11467–11478 (1998).

185. Podhajecky P., Zabransky Z., Novak P., Dobiasova L., Cerny R. ,Valvoda V. Relation between Crystallographic Microstructure and Electrochemical Properties of CuO for Lithium Cells. *Electrochim. Acta* **35,** 245 (1990).

186. Lanzaa, F., Feduzia R., Fugera, J. Effects of lithium oxide on the electrical properties of CuO at low temperatures. *J. Mater. Res.* **5,** 1739–1744 (1990).

187. Morais, J. M., Papadimitrakopoulos, F. & Burgess, D. J. Biomaterials/tissue interactions: possible solutions to overcome foreign body response. *AAPS J.* **12,** 188–196 (2010).

188. Wang, Y., Papadimitrakopoulos, F. & Burgess, D. J. Polymeric 'smart' coatings to prevent foreign body response to implantable biosensors. *J. Control. Release* **169,** 341–347 (2013).

189. Onuki, Y., Bhardwaj, U., Papadimitrakopoulos, F. & Burgess, D. J. A review of the biocompatibility of implantable devices: current challenges to overcome foreign body response. *J. Diabetes Sci. Technol.* **2,** 1003–15 (2008).

190. Kotanen, C. N., Moussy, F. G., Carrara, S. & Guiseppi-Elie, A. Implantable enzyme amperometric biosensors. *Biosensors and Bioelectronics* **35,** 14–26 (2012).

191. Vaddiraju, S., Tomazos, I., Burgess, D. J., Jain, F. C. & Papadimitrakopoulos, F. Emerging synergy between nanotechnology and implantable biosensors: A review. *Biosensors and Bioelectronics* **25,** 1553–1565 (2010).

192. Ziegler, K. J. Developing implantable optical biosensors. *Trends in Biotechnology* **23,** 440–444 (2005).

193. Olivo, J., Carrara, S., De Micheli, G. & Micheli, G. De. Energy Harvesting and Remote Powering for Implantable Biosensors. *IEEE Sens. J.* **11,** 1573–1586 (2011).

194. Luz, R. A. S., Iost, R. M. & Crespilho, F. N. in *Nanobioelectrochemistry: From Implantable Biosensors to Green Power Generation* 27–48 (Springer-Verlag Berlin Heidelberg, 2013).

195. Zhou, D. D. & Greenberg, R. J. in *Biosensors and their Applications in Healthcare* **November,**

24–36 (2013).

196. Heo, Y. J. & Takeuchi, S. Towards Smart Tattoos: Implantable Biosensors for Continuous Glucose Monitoring. *Advanced Healthcare Materials* **2,** 43–56 (2013).

197. Cash, K. J. & Clark, H. A. Nanosensors and nanomaterials for monitoring glucose in diabetes. *Trends Mol. Med.* **16,** 584–93 (2010).

198. Rahman, M. M., Ahammad, A. J. S., Jin, J.-H., Ahn, S. J. & Lee, J.-J. A comprehensive review of glucose biosensors based on nanostructured metal-oxides. *Sensors (Basel).* **10,** 4855–86 (2010).

199. Zhu, Z. *et al.* A critical review of glucose biosensors based on carbon nanomaterials: carbon nanotubes and graphene. *Sensors (Basel).* **12,** 5996–6022 (2012).

200. Zhang, Y. *et al.* CuO nanowires based sensitive and selective non-enzymatic glucose detection. *Sensors Actuators B Chem.* **191,** 86–93 (2014).

201. Wang, X. *et al.* Synthesis of CuO nanostructures and their application for nonenzymatic glucose sensing. *Sensors Actuators B Chem.* **144,** 220–225 (2010).

202. Zhao, Y. *et al.* Room temperature synthesis of 2D CuO nanoleaves in aqueous solution. *Nanotechnology* **22,** 115604 (2011).

203. Jiang, L.-C. & Zhang, W.-D. A highly sensitive nonenzymatic glucose sensor based on CuO nanoparticles-modified carbon nanotube electrode. *Biosens. Bioelectron.* **25,** 1402–7 (2010).

204. Zhang, W. De *et al.* Synthesis of vertically aligned carbon nanotubes on metal deposited quartz plates. *Carbon N. Y.* **40,** 1981–1989 (2002).

205. Batra, N., Tomar, M. & Gupta, V. ZnO-CuO composite matrix based reagentless biosensor for detection of total cholesterol. *Biosens. Bioelectron.* **67,** 263–71 (2015).

206. Espro, C., Donato, N., Galvagno, S., Aloisio, D., Leonardi, S.G., Neri, G. CuO Nanowires-based Electrodes for Glucose Sensors. *Chem. Eng. Trans.* **41,** 415–420 (2014).

207. Zhang, X. *et al.* High electrochemical performance based on ultrathin porous CuO nanobelts grown on Cu substrate as integrated electrode. *Phys. Chem. Chem. Phys.* **15,** 521–5 (2013).

208. Singh, J., Srivastava, M., Kalita, P. & Malhotra, B. D. A novel ternary NiFe2O4/CuO/FeO-chitosan nanocomposite as a cholesterol biosensor. *Process Biochem.* **47,** 2189–2198 (2012).

209. Ibupoto, Z. H., Khun, K., Liu, X. & Willander, M. Low temperature synthesis of seed mediated CuO bundle of nanowires, their structural characterisation and cholesterol detection. *Mater. Sci. Eng. C* **33,** 3889–3898 (2013).

210. Zhu, G. *et al.* Facile fabrication and enhanced sensing properties of hierarchically porous CuO
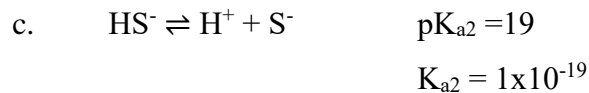
architectures. *ACS Appl. Mater. Interfaces* **4,** 744–751 (2012).

211. Hsueh, H. T. *et al.* Ethanol Gas Sensor of Crabwise CuO Nanowires Prepared on Glass Substrate. *J. Electrochem. Soc.* **158,** J106 (2011).

212. Kim, K. M. *et al.* Selective Detection of NO2 Using Cr-Doped CuO Nanorods. *Sensors (Switzerland)* **12,** 8013–8025 (2012).

213. Jin, C. *et al.* Influence of coating and thermal annealing on the structure and luminescence properties of CuO nanorods. *Solid State Commun.* **150,** 1812–1817 (2010).

214. Yang, M. *et al.* Copper oxide nanoparticle sensors for hydrogen cyanide detection: Unprecedented selectivity and sensitivity. *Sensors Actuators B Chem.* **155,** 692–698 (2011).

215. Bari, R.H., ; Patil, S.B., ; Bari, A.R. Spray-pyrolized nanostructured CuO thin films for H2S gas sensor. *Int. Nano Lett.* **3,** 12 (2013).

216. Xu, J. *et al.* Synthesis, field emission and humidity sensing characteristics of honeycomb-like CuO. *J. Phys. D. Appl. Phys.* **42,** 75417 (2009).

217. Chen, J., ; Wang , K. ; Hartman, L. ; Zhou, W. H2S Detection by Vertically Aligned CuO Nanowire Array Sensors. *J. Phys. Chem. C* **112,** 16017–16021 (2008).

218. Zhang, F., Zhu, A., Luo, Y., Tian, Y., Yang, J., Qin, Y. CuO Nanosheets for Sensitive and Selective Determination of H2S with High Recovery Ability. *J. Phys. Chem. C* **114,** 19214–19219 (2010).

219. Li, X., Wang, Y., Lei, Y. & Gu, Z. Highly sensitive H2S sensor based on template-synthesized CuO nanowires. *RSC Adv.* **2,** 2302 (2012).

220. Ramgir, N. S. *et al.* Sub-ppm H2S sensing at room temperature using CuO thin films. *Sensors Actuators B Chem.* **151,** 90–96 (2010).

221. Liu, J. *et al.* H2S Detection Sensing Characteristic of CuO/SnO2 Sensor. *Sensors* **3,** 110–118 (2003).

222. Kumar, R. *et al.* CuO–SnO 2 element as hydrogen sulfide gas sensor prepared by a sequential electron beam evaporation technique. *J. Phys. D. Appl. Phys.* **36,** 2377–2381 (2003).

223. Asad, M. & Sheikhi, M. H. Highly sensitive wireless H2S gas sensors at room temperature based on CuO-SWCNT hybrid nanomaterials. *Sensors Actuators B Chem.* **231,** 474–483 (2016).

224. Ferrari, a C. & Basko, D. M. Raman spectroscopy as a versatile tool for studying the properties of graphene. *Nat. Nanotechnol.* **8,** 235–246 (2013).

225. Filler, G. *et al.* Cystatin C as a marker of GFR—history, indications, and future research. *Clin. Biochem.* **38,** 1–8 (2005).

226. McMenamy, R., Lund, C., Oncley, J.L. Unbound Amino Acid Concentrations in Human Blood Plasmas. *J. Clin. Invest.* **36,** 1672–1679 (1957).

227. Loeb, R., Benedict, E. Inorganic Sulphates in Human Blood. *J. Clin. Invest.* **4,** 33–36 (1927).

228. Hoetink, A. E., Faes, T. J. C., Visser, K. R. & Heethaar, R. M. On the flow dependency of the electrical conductivity of blood. *IEEE Trans. Biomed. Eng.* **51,** 1251–1261 (2004).

229. Hirsch, F. G. *et al.* The Electrical Conductivity of Blood I. Relationship to Erythrocyte Concentration. *Blood* **5,** 1017–1035 (1950).

APPENDIX A: H₂S RATIO EQUATION DERIVATIONS

$H_2S - HS^- - S^{2-}$ Relation Derivation:

1. The interrelated Reactions:

    a. $H_2O \rightleftharpoons H^+ + OH^-$ $K_{aH_2O} = 1.8 \times 10^{-16}$

    b. $H_2S \rightleftharpoons H^+ + HS^-$ $pK_{a1} = 7.05$

                                      $K_{a1} = 8.91 \times 10^{-8}$

    c. $HS^- \rightleftharpoons H^+ + S^-$ $pK_{a2} = 19$

                                          $K_{a2} = 1 \times 10^{-19}$

2. Ratio Equations

At a given pH, the concentration of hydrogen ions ($[H^+]$) remains constant.

1) 1a) $pH = -\log[H^+]$

     1b) $[H^+] = 10^{-pH}$

2) 2a) $K_{a2} = \dfrac{[H^+][S^{2-}]}{[HS^-]}$

    2b) $\dfrac{[HS^-]}{[S^{2-}]} = \dfrac{[H^+]}{K_{a2}}$

Sub in 1b into 2b and also $K_{a2} = 1 \times 10^{-19}$:

    2c) $\dfrac{[HS^-]}{[S^{2-}]} = \dfrac{10^{-pH}}{1 \times 10^{-19}}$

    2a) $K_{a2} = \dfrac{[H^+][S^{2-}]}{[HS^-]}$

    2d) $\dfrac{[H^+][S^{2-}]}{K_{a2}} = [HS^-]$

Sub in 1b into 2d.

2e) $\dfrac{10^{-pH} \cdot [S^{2-}]}{K_{a2}} = [HS^-]$

3) 3a) $K_{a1} = \dfrac{[H^+][HS^-]}{[H_2S]}$

3b) $\dfrac{[H^+]}{K_{a1}} = \dfrac{[H_2S]}{[HS^-]}$

Sub in $K_{a1} = 8.91 \times 10^{-8}$

3c) $\dfrac{[H^+]}{8.91 \times 10^{-8}} = \dfrac{[H_2S]}{[HS^-]}$

Sub 1b into 3c.

3d) $\dfrac{10^{-pH}}{8.91 \times 10^{-8}} = \dfrac{[H_2S]}{[HS^-]}$

3e) $\dfrac{10^{-pH} \cdot [HS^-]}{K_{a1}} = [H_2S]$

Sub in 2d into 3e.

3f) $\dfrac{10^{-pH} \cdot \frac{10^{-pH} \cdot [S^{2-}]}{K_{a2}}}{K_{a1}} = [H_2S]$

3g) $\dfrac{(10^{-pH})^2 [S^{2-}]}{K_{a1} \cdot K_{a2}} = [H_2S]$

3h) $\dfrac{(10^{-pH})^2}{K_{a1} \cdot K_{a2}} = \dfrac{[H_2S]}{[S^{2-}]}$

Simplify using exponent laws and sub in $K_{a1} = 8.91 \times 10^{-8}$ and $K_{a2} = 1 \times 10^{-19}$

3g) $\dfrac{10^{-2pH}}{8.91 \times 10^{-8} \cdot 1 \times 10^{-19}} = \dfrac{[H_2S]}{[S^{2-}]}$

3h) $\dfrac{10^{-2pH}}{8.91 \times 10^{-27}} = \dfrac{[H_2S]}{[S^{2-}]}$

APPENDIX B: H₂S RATIO CHARTS COMPARING THE RESULTS OF THE DIFFERENT PKA₂ VALUES

Using the ratio equations derived in Appendix A, by substituting the pKa_2 value of interest and different pH levels, the following charts can be obtained.

Table B1. A chart showing the ratios of H_2S, HS^- and S^{2-} for the given pKa_2 values

pka₂ = 19

pH	Ratio	Ratio-Value	Comment
1	[H2S]/[HS-]	1.1220E+06	Mostly H₂S in Sol'n and almost no S²⁻
	[HS-]/[S2-]	1.0000E+12	
	[H2S]/[S2-]	1.1220E+18	
2	[H2S]/[HS-]	1.1220E+05	
	[HS-]/[S2-]	1.0000E+11	
	[H2S]/[S2-]	1.1220E+16	
3	[H2S]/[HS-]	1.1220E+04	
	[HS-]/[S2-]	1.0000E+10	
	[H2S]/[S2-]	1.1220E+14	
4	[H2S]/[HS-]	1.1220E+03	
	[HS-]/[S2-]	1.0000E+09	
	[H2S]/[S2-]	1.1220E+12	
5	[H2S]/[HS-]	1.1220E+02	
	[HS-]/[S2-]	1.0000E+08	
	[H2S]/[S2-]	1.1220E+10	
6	[H2S]/[HS-]	1.1220E+01	

pka₂ = 13

pH	Ratio	Ratio-Value	Comment
1	[H2S]/[HS-]	1.1220E+06	Mostly H₂S in sol'n and almost no S²⁻
	[HS-]/[S2-]	1.0000E+18	
	[H2S]/[S2-]	1.1220E+24	
2	[H2S]/[HS-]	1.1220E+05	
	[HS-]/[S2-]	1.0000E+17	
	[H2S]/[S2-]	1.1220E+22	
3	[H2S]/[HS-]	1.1220E+04	
	[HS-]/[S2-]	1.0000E+16	
	[H2S]/[S2-]	1.1220E+20	
4	[H2S]/[HS-]	1.1220E+03	
	[HS-]/[S2-]	1.0000E+15	
	[H2S]/[S2-]	1.1220E+18	
5	[H2S]/[HS-]	1.1220E+02	
	[HS-]/[S2-]	1.0000E+14	
	[H2S]/[S2-]	1.1220E+16	
6	[H2S]/[HS-]	1.1220E+01	

	Species ratio	Value	Note		Species ratio	Value	Note
	[HS-]/[S2-]	1.0000E+07			[HS-]/[S2-]	1.0000E+13	
	[H2S]/[S2-]	1.1220E+08			[H2S]/[S2-]	1.1220E+14	
7	[H2S]/[HS-]	1.1220E+00	$[H_2S] = [HS^-]$	7	[H2S]/[HS-]	1.1220E+00	$[H_2S] = [HS^-]$
	[HS-]/[S2-]	1.0000E+06			[HS-]/[S2-]	1.0000E+12	
	[H2S]/[S2-]	1.1220E+06			[H2S]/[S2-]	1.1220E+12	
8	[H2S]/[HS-]	1.1220E-01		8	[H2S]/[HS-]	1.1220E-01	
	[HS-]/[S2-]	1.0000E+05			[HS-]/[S2-]	1.0000E+11	
	[H2S]/[S2-]	1.1220E+04			[H2S]/[S2-]	1.1220E+10	
9	[H2S]/[HS-]	1.1220E-02		9	[H2S]/[HS-]	1.1220E-02	
	[HS-]/[S2-]	1.0000E+04			[HS-]/[S2-]	1.0000E+10	
	[H2S]/[S2-]	1.1220E+02			[H2S]/[S2-]	1.1220E+08	
10	[H2S]/[HS-]	1.1220E-03		10	[H2S]/[HS-]	1.1220E-03	
	[HS-]/[S2-]	1.0000E+03			[HS-]/[S2-]	1.0000E+09	
	[H2S]/[S2-]	1.1220E+00	$[H2S] = [S2-]$		[H2S]/[S2-]	1.1220E+06	
11	[H2S]/[HS-]	1.1220E-04		11	[H2S]/[HS-]	1.1220E-04	
	[HS-]/[S2-]	1.0000E+02			[HS-]/[S2-]	1.0000E+08	
	[H2S]/[S2-]	1.1220E-02			[H2S]/[S2-]	1.1220E+04	
12	[H2S]/[HS-]	1.1220E-05		12	[H2S]/[HS-]	1.1220E-05	
	[HS-]/[S2-]	1.0000E+01			[HS-]/[S2-]	1.0000E+07	
	[H2S]/[S2-]	1.1220E-04			[H2S]/[S2-]	1.1220E+02	
13	[H2S]/[HS-]	1.1220E-06		13	[H2S]/[HS-]	1.1220E-06	
	[HS-]/[S2-]	1.0000E+00	[HS-]=[S2-]		[HS-]/[S2-]	1.0000E+06	
	[H2S]/[S2-]	1.1220E-06			[H2S]/[S2-]	1.1220E+00	$[H_2S]=[S^{2-}]$
14	[H2S]/[HS-]	1.1220E-07		14	[H2S]/[HS-]	1.1220E-07	
	[HS-]/[S2-]	1.0000E-01			[HS-]/[S2-]	1.0000E+05	
	[H2S]/[S2-]	1.1220E-08			[H2S]/[S2-]	1.1220E-02	

APPENDIX C: THE ONLY VALUE EFFECTED BY PKA$_2$ IS [S^{2-}]:

The following example illustrates how the only value effected by the pKa$_2$ is [S^{2-}]:

At pH =7, given total [S^{2-}] concentration of = 1.0 x10^{-1} M, obtained from a ½ dilution of H$_2$S solution in SAOB, what are [H$_2$S], [HS$^-$], [S^{2-}]? (See Section 3.2.4 for full details on the calculation.)

pKa2= 19:

$$[S^{2-}] = \frac{[S^{2-}]_T \, V_T}{V_i \cdot (1+1.122x10^{12}+1x10^{12})}$$

Given V$_T$/V$_i$ = 2

$$[S^{2-}] = \frac{2[S^{2-}]_T}{(2.122x10^{12})}$$

$$[S^{2-}] = \frac{2 \cdot 1.0x10^{-1}M}{(2.122x10^{12})}$$

$$[S^{2-}] = \frac{2.0x10^{-1}M}{(2.122x10^{12})}$$

$$[S^{2-}] = 9.425x10^{-17}M$$

$$[H_2S] = 1.122 \; x \; 10^{12}[S^{2-}]$$

$$[H_2S] = 1.122 \; x \; 10^{12}(9.425x10^{-17}M)$$

$$[H_2S] = 1.0575 \; x \; 10^{-4}M$$

$$[HS^-] = 1.00 \; x \; 10^{12}(9.425x10^{-17}M)$$

$$[HS^-] = 9.42 \; x \; 10^{-5}M$$

Therefore:

[H$_2$S] = 1.0575 x10^{-4} M

pKa2=13

$$[S^{2-}] = \frac{[S^{2-}]_T \, V_T}{V_i \cdot (1+1.122x10^6+1x10^6)}$$

Given V$_T$/V$_i$ = 2

$$[S^{2-}] = \frac{2[S^{2-}]_T}{(2.122x10^6)}$$

$$[S^{2-}] = \frac{2 \cdot 1.0x10^{-1}M}{(2.122x10^6)}$$

$$[S^{2-}] = \frac{2.0x10^{-1}M}{(2.122x10^6)}$$

$$[S^{2-}] = 9.425x10^{-11}M$$

$$[H_2S] = 1.122 \; x \; 10^6[S^{2-}]$$

$$[H_2S] = 1.122 \; x \; 10^6(9.425x10^{-11}M)$$

$$[H_2S] = 1.0575 \; x \; 10^{-4}M$$

$$[HS^-] = 1.00 \; x \; 10^6(9.425x10^{-11}M)$$

$$[HS^-] = 9.42 \; x \; 10^{-5}M$$

Therefore:

[H$_2$S] = 1.0575 x10^{-4} M

$[HS^-] = 9.45 \times 10^{-5}$ M

$[S^{2-}] = 9.425 \times 10^{-17}$ M

$[HS^-] = 9.45 \times 10^{-5}$ M

$[S^{2-}] = 9.425 \times 10^{-11}$ M

APPENDIX D: INCOMPLETE PREPARATION OF COUPON USING CUO PLASMA

Plasma Coupon Production

Cu (foil) was cleaned with 100 mM HCl for 1 min and then scrubbed with scotch brite until it shined. The CuO was then screwed to a plate to the inside of a plasma chamber. A nominal voltage was applied (a negative bias) of ~600 V (400V is the breaking point of O_2, but 600V provided a bright blue-purple glow). The pressure of the chamber was dropped to 320 mTorr. The oxygen flow rate of 100 sccm (100%). The time used for the experiment was 1 hour. However, due to a malfunction with the high voltage power supply, we were unable to finish it. Note: Oxygen plasma was observed.
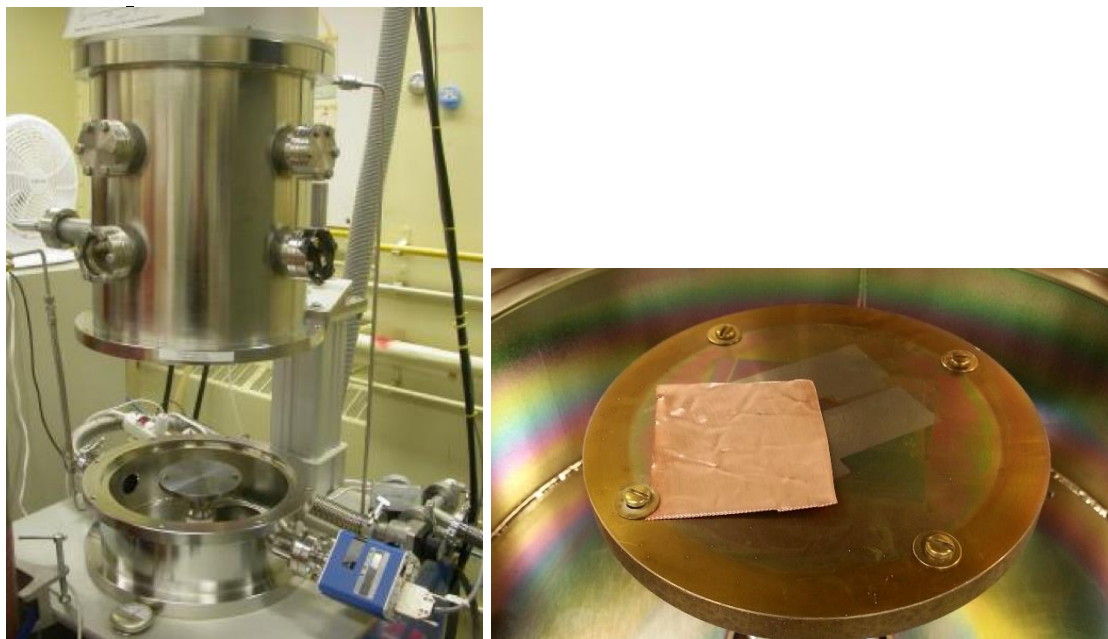
a)   b)
Fig D1. Showing the vacuum plasma chamber and a piece of copper foil ready for experimentation. Fig D1a) showing the ion plasma chamber. This picture is courtesy of Prof. M.P. Bradley, University of Saskatchewan. Fig D1b) shows a piece of copper foil ready for the plasma reaction.